IChF
Institute of Physical Chemistry PAS

Ph.D. thesis within the Warsaw-4-PhD at the
Institute of Physical Chemistry, Polish Academy of Sciences
Kasprzaka 44/52, 01-224 Warsaw

Widely-Tunable All-Fiber Laser Source for Coherent Raman Scattering Microscopy

Ph.D. Candidate: M.Sc. Cássia Corso Silva

Supervisor: prof. dr. hab. Yuriy Stepanenko
Auxiliary supervisor: dr. eng. Katarzyna Krupa

Warsaw, February 2025

Acknowledgments

Gostaria de agradecer a toda minha família, especialmente à minha mãe e à minha irmãzinha. Obrigada por todo o apoio e incentivo que me deram desde a infância. Todas essas conquistas não são apenas minhas, são nossas. Amo vocês.

I would like to acknowledge my supervisor, prof. dr. Yuriy Stepanenko and dr. eng. Katarzyna Krupa, for giving me this opportunity to be part of the lab. Working with Yura motivated me not only to learn about physics but also to explore other fields. His enthusiasm and broad knowledge are truly admirable. Kasia has been the role model who inspired me how to do research. Her positive outlook on life, her constant support, and her ability to always see the good in every situation made her much more than a mentor to me. I will always be grateful.

I would like to thank the entire Laser Centre team for all the scientific discussions and hard work. A special thanks to dr. Marcin Pastorczak for the fun in the lab with good music, and our conversations covering a wide range of topics, were always enjoyable. I would like to thank dr. Łukasz Zinkiewicz for the good time at the lab measuring the cells and the amazing scientific discussions. I am grateful to dr. hab. Angulo Nunez Gonzalo Manuel, dr. Hector Rodriguez Rodriguez and mgr. Sanat Kumar Mahankudo, for the lunches filled with lively discussions about fascinating and random topics.

My sincere thanks go to prof. dr. Vincent Couderc, dr. hab. Alessandro Tonello and dr. Tigran Mansuryan, who supervised my internship in Limoges. It was a wonderful time between the lab and the pâtisserie.

I am grateful for all the friends I made here, Jadwiga, Julia, and Rene. I couldn't have done it without you. To my old friends, thank you for your unwavering support and video calls. For the emotional support and love, I thank Alex. Meeting you has made my life so much better.

To all the people involved in this thesis, thank you for your patience in reading and helping me improve my writing.

One of the most beautiful memories I have from my time in Poland was seeing snow for the first time. Hearing the crunch of each step and seeing all the trees covered in snow is something I will never forget.

Funding acknowledgements

This thesis has been funded by the Foundation for Polish Science (FNP) within the TEAM-NET project (POIR.04.04.00-00-16ED/18-00) and partially by the National Agency for Academic Mobility (NAWA) within POLONIUM mobility project (BPN/BFR/2021/ 1/00013).

This thesis was developed within the Warsaw PhD School in Natural and BioMedical Sciences (Warsaw-4-PhD Doctoral School) at the Institute of Physical Chemistry of the Polish Academy of Sciences.

"Navegar é preciso. Viver não é preciso."

Álvaro de Campos (Fernando Pessoa).

List of Publications

Publications related to the thesis:

1. **Silva, C. C.**, Zinkiewicz, Ł., Pielach, M., Jamrozik, A., Królikowska, M., Purzycka, J., Wasylczyk, P., Krupa, K., and Stepanenko, Y., “Stimulated Raman scattering microscope for leukemic cell imaging.” In Label-free Biomedical Imaging and Sensing (LBIS) 2023 (Vol. 12391, pp. 136-141). **SPIE. Proc. of SPIE Vol. 12391 123910M-6.**
2. **Corso, C.**, Mansuryan, T., Tonello, A., Arosa, Y., Stepanenko, Y., Couderc, V., and Krupa, K., “Tunable four-wave mixing enabled by a self-phase modulation of chirped pulses.” Optics Letters, 48(21), 5531-5534, 2023. **10.1364/OL.502065**.

Others publications:

1. dos Santos, G. H., Salles, D. C. D., Damaceno, M. G., Menezes, B. T. D., **Corso, C.**, Martinelli, M., Souto Ribeiro, P.H., and de Araújo, R. M., “Decomposing spatial mode superpositions with a triangular optical cavity.” Physical Review Applied, 16(3), 034008, 2021. **10.1103/PhysRevApplied.16.034008**.

Conferences:

1. “Light Source for SRS based Microscopy”, MODy 2021, Mazury, Poland, 26-29/09/2021, **Oral presentation**
2. “Fiber laser for Stimulated Raman Scattering imaging”, MODy 2022, Jachranka, Poland, 26-28/09/2022, **Oral presentation**
3. “Stimulated Raman scattering microscope for leukemic cell imaging”, SPIE Photonics West, San Francisco, California, United States, 29/01-02/02/2023, **Oral presentation**

4. Silva, C. C., Mansuryan, T., Tonello, A., Arosa-Lobato, Y., Stepanenko, Y., Couderc, V., and **Krupa, K.**, “Four-Wave-Mixing controlled by Self-Phase-Modulation of chirped pulses.” In CLEO: Science and Innovations (pp. SM4F-3), Optica Publishing Group, San Jose, United States, 07-12/05/2023, **Oral presentation by dr. eng. K. Krupa**

5. Silva, C. C., Mansuryan, T., Tonello, A., Arosa-Lobato, Y., Stepanenko, Y., Couderc, V., and **Krupa, K.**, “CARS imaging allowed by Four-Wave-Mixing widely tunable by chirped pulses.” In 2023 Conference on Lasers and Electro-Optics Europe and European Quantum Electronics Conference (CLEO/Europe-EQEC) (pp. 1-1), IEEE, Munich, Germany, 26-30/06/2023, **Oral presentation by dr. eng. K. Krupa**

6. “Tunable dual-wavelength light source for Stimulated Raman Scattering imaging”, Conference of the NLPQT, Warsaw, Poland, 19-20/10/2023, **Poster presentation**

7. “Tunable four-wave mixing based light source for nonlinear imaging applications”, Women in Photonics 2023, Jena, Germany, 26-30/11/2023, **Oral and Poster presentation**

8. “Tunable four-wave mixing based light source”, IPC Microsymposium, Warsaw, Poland, 09-10/01/2024, **Poster presentation**

9. “Tunable four-wave mixing based light source for nonlinear imaging”, Doctoral Seminar, IChF-IPhT, Dornburg, Germany, 18-21/03/2024, **Poster presentation**

10. Silva, C., Mansuryan, T., Tonello, Zinkiewicz L., Fabjanowicz B., Pielach M., Jamrozik A., Kardas T., Arosa-Lobato Y., Wasylczyk P., Couderc V., Stepanenko Y., and **Krupa, K.**, “Fiber light sources for nonlinear imaging applications”, Advanced Photonics Congress 2024, Specialty Optical Fibers, Quebec City, Canada, 28/07-01/08/2024, Optica Publishing Group, paper SoM4F.2, **Invited oral presentation by dr. eng. K. Krupa**

11. “Tunable four-wave mixing based light source for nonlinear imaging”, IPC Microsymposium, Warsaw, Poland, 13-15/01/2025, **Poster presentation** **This poster has been recognized as outstanding by the International Advisory Board - IAB*

International Schools:

1. "Fiber laser for Stimulated Raman Scattering imaging", 2021 Siegman International School On Lasers: 25/06-02/07/2022, Chęciny, Poland, **Poster presentation**
2. "Tunable four-wave mixing based light source for nonlinear imaging applications", 1st Photonics Talent Internation Summer School: 08-12/07/2024, Bordeaux, France, **Poster presentation**
3. "Tunable four-wave mixing based light source for nonlinear imaging applications", Warsaw Summer School on Advanced Optical Imaging 2024, 03-05/09/2024, Warsaw, Poland, **Poster presentation**

Patents:

1. Polish patent application: **Corso, C.**, Mansuryan, T., Tonello, A., Arosa, Y., Stepanenko, Y., Couderc, V., and Krupa, K., title *Źródło laserowe o szerokim zakresie strojenia z wykorzystaniem parametrycznego nieliniowego efektu mieszania fal z impulsami ze świergotem i sposób szerokopasmowego przestrajania źródła laserowego z wykorzystaniem parametrycznego nieliniowego efektu mieszania fal z impulsami ze świergotem.* **P.444762, submitted 03/05/2023.**
2. EPO (EU) patent application: **Corso, C.**, Mansuryan, T., Tonello, A., Arosa, Y., Stepanenko, Y., Couderc, V., and Krupa, K., title *Widely tunable laser source using parametric nonlinear effect of wave mixing with chirped pulses and method of broadband tunable laser source using parametric nonlinear effect of wave mixing with chirped pulses.* **EP24174041, submitted 03/05/2024.**

Abstract

The development of fiber laser sources has been a focus of research for several decades, driven by the increasing demand for numerous applications, including Coherent Raman Scattering (CRS) microscopy. The CRS stands out among microscopy techniques due to its advantages of label-free imaging and high resolution. This thesis will introduce three wavelength tunable laser sources that exploit nonlinear effects in optical fibers to enable Raman measurement in both fingerprint and C-H stretch spectral regions. Access to the fingerprint region is particularly valuable, as it facilitates improved chemosensitivity assessment, an area that remains poorly addressed by current state-of-the-art fiber light sources.

The first dual-wavelength Stimulated Raman Scattering (SRS) light source to be developed will allow measurements in the fingerprint Raman region, covering the range from 950 cm^{-1} to 1600 cm^{-1}. This fiber laser source will deliver tunable output for the pump and Stokes beams ranging from 913 nm to 930 nm, and from 1020 nm to 1070 nm, respectively, with an average power of 40 mW for each beam. The tunability of the Stokes beam will be achieved by using a novel method of spectral broadening through Self-Phase Modulation (SPM) of chirped pulses in all-fiber configuration. The light source will be validated through its implementation into SRS microscopy for imaging polystyrene beads and leukemic cells.

The second light source will be designed to perform imaging in both the fingerprint and C-H stretch Raman regions. The fiber optical parametric oscillator using the Degenerate-Four-Wave Mixing (D-FWM) will be presented. The system will be built around the fiber oscillator with a fixed central wavelength, serving as a seed beam. The pump tunability will be achieved exploiting a novel method involving spectral broadening of chirped pulses, followed by spectral filtering and amplification similar to the approach used in the first light source. The obtained D-FWM signals will be tunable between 730 nm to 940 nm. While considering the second beam at 1030 nm, this can enable Raman measurements in the range from 929 cm^{-1} to 3990 cm^{-1}.

The third part of the thesis will focus on development of a novel method for tuning D-FWM sidebands based on the SPM of chirped pulses. This method will involve varying the chirp of the pump pulses at fixed central wavelength that are next injected into the concatenation of standard fiber and a photonic crystal fiber. The outermost redshifted SPM peak exhibits significant spectral power density to act as a tunable pump for the D-FWM process. When combined with a 1030 nm beam, this may allow measurements in the fingerprint and C-H stretch Raman regions spanning from 873 cm^{-1} and 3738 cm^{-1}. Coherent Anti-Stokes Raman Scattering imaging of polystyrene beads and droplet paraffin will also be conducted to validate this light source.

Streszczenie

Ze względu na ogromny potencjał zastosowania w wielu dziedzinach, w tym mikroskopii koherentnego rozpraszania Ramana (ang. Coherent Raman Scattering - CRS), rozwój źródeł laserowych opartych o technologię światłowodową jest przedmiotem intensywnych badań już od kilku dekad. Zaletami wyróżniającymi koherentne rozpraszania Ramana spośród innych technik mikroskopowych jest wysoka rozdzielczość oraz możliwość obrazowania bez stosowania dodatkowych znaczników chemicznych. Niniejsza praca prezentuje trzy przestrajalne źródła laserowe, działające w oparciu o efekty nieliniowe zachodzące w światłowodach. Źródła te umożliwiają pomiar widma Ramana zarówno w zakresie widma charakterystycznego danej substancji tzw. chemicznego odcisku palca (ang. fingerprint), jak i drgań rozciągających wiązań C-H. Dostęp do obszaru ramanowskiego odcisku palca jest szczególnie istotny, gdyż pozwala na lepszą ocenę czułości chemicznej, jednakże na ten moment obszar ten pozostaje niewystarczająco zaadresowany przez istniejące lasery światłowodowe.

Pierwsze zbudowane dwukolorowe źródło światła do zastosowania w mikroskopii wymuszonego rozpraszania Raman (ang. Stimulated Raman Scattering - SRS) umożliwia pomiary w obszarze ramanowskiego odcisku palca obejmującym zakres od 950 cm^{-1} do 1600 cm^{-1}. Przedstawiony laser światłowodowy zapewnia przestrajanie w zakresach od 913 nm do 930 nm oraz od 1020 nm do 1070 nm, odpowiednio, dla wiązki pompującej oraz wiązki Stokesa. Moc średnia każdej z wiązek to 40 mW. Możliwość przestrajania wiązki Stokesa osiągnięto dzięki zastosowaniu nowej metody poszerzania widma poprzez samomodulację fazy (ang. Self-Phase Modulation - SPM) impulsów ćwierkających (ang. chirped pulses) w konfiguracji całkowicie światłowodowej. W celu weryfikacji, opisane źródło światła zintegrowano z mikroskopem wymuszonego rozpraszania Ramana i wykorzystano do obrazowania kulek polistyrenowych i komórek białaczki.

Drugie źródło światła zostało zaprojektowane w celu obrazowania zarówno w obszarze ramanowskiego odcisku palca, jak i drgań rozciągających C-H. Przedstawiono parametryczny oscylator światłowodowy wykorzystujący zdegenerowane mieszanie czterofalowe (ang. Degenerate-Four-Wave Mixing - D-FWM). System zbudowano na bazie oscylatora światłowodowego o ustalonej centralnej długości fali, służącego jako wiązka zasiewająca. Strojenie pompy zrealizowano stosując nowatorską metodę

obejmującą poszerzenie widmowe impulsów ćwierkających, a następnie filtrowanie widmowe i wzmocnianie, analogicznie jak w przypadku pierwszego źródła. Uzyskane sygnały mieszania czterofalowego są przestrajalne w zakresie od 730 nm do 940 nm. Biorąc pod uwagę drugą wiązkę o długości fali 1030 nm, umożliwi to pomiary Ramana w zakresie od 929 cm^{-1} do 3990 cm^{-1}.

Trzecia część pracy jest poświęcona opracowaniu nowej metody strojenia pasm bocznych mieszania czterofalowego w oparciu o samomodulację fazy impulsów ćwierkających. Metoda ta obejmuje zmianę wartości świergotu impulsów pompujących przy ustalonej centralnej długości fali, które są następnie wprowadzane do odcinka standardowego światłowodu połączonego ze światłowodem fotonicznym. Wykazano, iż najbardziej zewnętrzny, przesunięty w kierunku czerwieni pik samomodulacji fazy, charakteryzujący się dużą gęstością mocy widmowej, może być wykorzystany jako przestrajalna pompa w procesie zdegenerowanego mieszania czterofalowego. W połączeniu z wiązką 1030 nm umożliwia to pomiary w obszarze ramanowskiego odcisku palca oraz drgań rozciagających C-H, obejmującym zakres od 873 cm^{-1} do 3738 cm^{-1}. W celu walidacji tego źródła światła, przeprowadzono również obrazowanie za pomocą koherentego antystokesowskiego rozpraszania Ramana kulek polistyrenowych i kropelek parafiny.

Table of Contents

List of Figures

List of Tables

List of Acronyms

AOM Acoustic-Optic Modulator.

aS anti-Stokes.

ASE Amplified Spontaneous Emission.

CARS Coherent Anti-Stokes Raman Scattering.

CRS Coherent Raman Scattering.

D-FWM Degenerate-Four-Wave Mixing.

EOM Electro-Optic Modulator.

Er Erbium.

FOPAs Fiber-Optical Parametric Amplifiers.

FOPO Fiber Optical Parametric Oscillator.

FT Fourier Transform.

FWHM Full Width at Half Maximum.

FWM Four-Wave Mixing.

GRIN Graded-Index.

GVD Group Velocity Dispersion.

LMA Large-Mode-Area.

MMF Multimode Fiber.

Nd Neodymium.

NIR Near-Infrared.

NLS Nonlinear Schrödinger.

NOLM Nonlinear Optical Loop Mirror.

OWB Optical Wave Breaking.

PCF Photonic Crystal Fiber.

PM Polarization-Maintaining.

PMT Photomultiplier Tube.

RF Radio-Frequency.

SCG Supercontinuum Generation.

SF Spectral Focusing.

SHG Second-Harmonic Generation.

SMF Single-Mode Fiber.

SPM Self-Phase Modulation.

SpRS Spontaneous Raman Scattering.

SRG Stimulated Raman Gain.

SRL Stimulated Raman Loss.

SRS Stimulated Raman Scattering.

SSFS Soliton Self-Frequency Shift.

Ti:S Titanium:Sapphire.

TIR Total Internal Reflection.

Yb Ytterbium.

ZDW Zero Dispersion Wavelength.

List of Symbols

λ: Wavelength (nm or μm).
ν: Optical frequency (Hz).
ω: Angular frequency ($\omega = 2\pi\nu$, rad/s).
k: Wave vector magnitude ($k = 2\pi/\lambda$, rad/m).
n: Refractive index (dimensionless).
c: Velocity of light in vacuum ($\approx 3 \times 10^8\,\mathrm{m/s}$).
ϵ_0: Vacuum permittivity ($\approx 8.854 \times 10^{-12}\,\mathrm{F/m}$).
μ_0: Vacuum permeability ($\approx 4\pi \times 10^{-7}\,\mathrm{H/m}$).
P: Optical power (W).
I: Optical intensity ($\mathrm{W/m^2}$).
E: Electric field amplitude (V/m).
γ: Nonlinear coefficient ($\mathrm{W^{-1}m^{-1}}$).
$\chi^{(n)}$: n-th order nonlinear susceptibility.
T: Transmission coefficient (dimensionless).
R: Reflection coefficient (dimensionless).
$\Delta\nu$: Spectral bandwidth (Hz).
D: Dispersion parameter ($ps/km \cdot nm$).
β_1 Group Delay Parameter (GVP, s/m).
β_2 Group Velocity Dispersion (GVD, s^2/m).
G: Gain coefficient ($\mathrm{m^{-1}}$).
z: Propagation distance (m or cm).
A_{eff}: Effective mode area (m^2).

Chapter 1

Introduction

Coherent Raman Scattering (CRS) microscopy is a multi-photon technique widely used for in vivo studies and diagnostic imaging. Renowned for its label-free and non-invasive nature, this approach eliminates the need for sample preparation. It offers high chemical selectivity and allows the acquisition of high-resolution images of cells, and tissues, providing detailed insights into their molecular composition and structure. These features make CRS an ideal technique for biomedical applications. The two most commonly used CRS methods are Stimulated Raman Scattering (SRS) and Coherent Anti-Stokes Raman Scattering (CARS).

Several multicolor CRS imaging techniques have been developed to obtain Raman images at various vibrational frequencies, as will be described in Section 4.4. These techniques require multicolor light sources, which, until recently, were often based on solid-state lasers, typically Titanium:Sapphire (Ti:S) lasers, combined with free-space optics and Optical Parametric Oscillators (OPOs) using nonlinear crystals. However, such systems are bulky, expensive, and environmentally sensitive, making them unsuitable for use outside controlled laboratory settings, including clinical environments [1–5].

Recent advancements in nonlinear fiber optics and fiber laser technology have enabled the development of broadband or wavelength-tunable laser systems based on optical fibers. These systems offer a cost-effective, compact, and alignment-free solution. Furthermore, they exhibit excellent environmental stability when constructed entirely from polarization-maintaining fibers and components.

Current fiber gain media restrict the operation of fiber oscillators to spectral regions near 1.0 μm, 1.55 μm, and 1.9 μm. Various frequency conversion nonlinear effects can be employed to achieve wavelength tunability outside these regions. Examples of such effects include Soliton Self-Frequency Shift (SSFS), Four-Wave Mixing (FWM), and Supercontinuum Generation (SCG), all of which have been used in the development of multicolor light sources.

SSFS efficiently transfers energy from the pump pulse to a redshifted Stokes pulse [6–8], enabling the development of tunable laser systems. SCG, on the other hand, produces broadband light sources commonly by injecting ultrashort pump pulses into Photonic Crystal Fibers (PCFs) or highly nonlinear fibers (HNFs) near the Zero Dispersion Wavelength (ZDW) [9]. Light sources based on FWM combine the advantages of these effects, offering both wide and selective wavelength tunability with high power, particularly when implemented in cavity configurations. Standard approaches typically rely on tuning the pump wavelength [10].

Several fiber-based parametric schemes, such as Fiber Optical Parametric Oscillators (FOPOs), Fiber Optical Parametric Amplifiers (FOPAs), and Fiber Optical Parametric Chirped-Pulse Amplifiers (FOPCPAs), have been proposed [11–15]. Thanks to the use of FWM as a parametric effect, they are capable of covering the entire fingerprint and C-H stretch Raman regions [14].

Over recent years, there has been a growing demand for developing CRS light sources that are compact, cost-effective, and maintenance-free, thus suitable for clinical applications. The need for advancements in cancer diagnostics, pharmaceutical research, and other medical fields drives this demand.

1.1 The goal of this work

This thesis aims to explore and develop new methods for building widely tunable light sources that can be used for applications in CRS microscopy. With this in mind, I will investigate:

1. Is it possible to build a tunable fiber light source that enables measurements in the fingerprint Raman region based on supercontinuum generation in the normal dispersion regime?
2. Is it possible to build an optical parametric oscillator in an all-fiber configuration that enables a broad tunability range through the four-wave mixing nonlinear effect when pumped with a tunable laser system based on a fixed wavelength oscillator?
3. Is it possible to achieve broad tuning of four-wave mixing sidebands when pumped with laser systems at a fixed wavelength?

1.2 Structure of the thesis

This thesis is presented in 8 chapters. It starts with a theory of optical fibers in Chapter 2 by describing the principles of waveguiding, selected linear properties, as well as various types of optical fibers.

Chapter 3 introduces the theoretical background of the nonlinear effects in optical fibers, such as Self-Phase Modulation, Four-Wave Mixing, and Supercontinuum Generation, which are discussed in detail.

Chapter 4 presents the fundamental principles of Coherent Raman Scattering microscopy. The theoretical details and different approaches for CRS microscopy are presented.

Chapter 5 reports the development of a dual-tunable light source for Raman imaging in the fingerprint spectral region. Details of the light source development and the novel approach for spectral broadening in all-fiber configuration are presented. SRS imaging of leukemic cells in the fingerprint Raman region is also demonstrated.

Chapter 6 focuses on the development of a widely tunable FOPO light source that enables measurements across the fingerprint and C-H stretch Raman regions through the novel approach of spectral broadening.

Chapter 7 introduces a new method for spectral tuning of FWM sidebands. This work was realized in collaboration with the group of prof. dr. Vincent Couderc from the Institute of XLIM (UMR CNRS 7252) of the University of Limoges in France. Experimental results and numerically supported explanations behind the observed effect are presented. Additionally, CARS imaging of polystyrene beads and paraffin is demonstrated.

Finally, Chapter 8 concludes the thesis by summarizing the results obtained and discussing potential further improvements and further developments of the constructed light sources.

Chapter 2

Optical fibers

The development of optical fibers in the 1960s initially focused on transmitting images through bundles of glass fibers [16]. Later, in 1970, advancements in fiber fabrication and materials paved the way for efficient data transmission and communication over long distances. Today, optical fibers are employed in a wide range of applications [17–23], including the construction of laser systems and multicolor light sources.

Optical fibers are primarily categorized into two standard types: Single-Mode Fibers (SMFs) and Multimode Fibers (MMFs), based on the number of modes they can guide. Within this classification, microstructured optical fibers, also known as Photonic Crystal Fibers (PCFs), are the preferred choice for generating nonlinear effects due to their ability to tailor the fiber dispersive properties.

This chapter will briefly overview the fundamentals of optical fibers, including their main properties and waveguiding principles. Various types of optical fibers, including PCFs, will also be discussed.

2.1 Principle of waveguiding

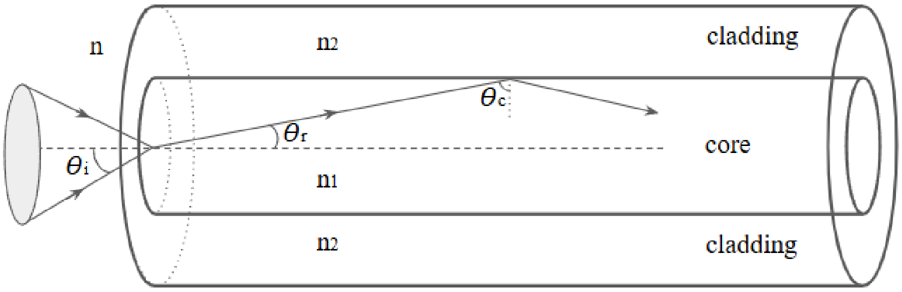

Figure 2.1: Segment of an optical fiber. n is the refraction index of the medium, n_1 is the refraction index of the core, n_2 is the refraction index of the cladding ($n_2 < n_1$), θ_i is the incident angle, θ_r is the refracted angle and θ_c is the critical angle.

Figure 2.1 illustrates a segment of an optical fiber, which consists of a cylindrical waveguide with a central core surrounded by a cladding layer. Light propagates in an optical fiber via Total Internal Reflection (TIR), a phenomenon first studied and demonstrated by J. Tyndall in 1870 [24, 25]. TIR occurs at the boundary between two media when light travels from a medium with a higher refractive index (the core of the fiber) to one with a lower refractive index (the cladding) when the angle of incidence exceeds a critical angle. This difference in refractive index ensures light is confined within the core, enabling efficient transmission over long distances.

Let us now look into more detail on the light propagation in an optical fiber through Snell's law:

$$n_1 \cdot sin(\theta_i) = n_2 \cdot sin(\theta_r), \tag{2.1}$$

where:

- n_1: refraction index of the core;
- n_2: refraction index of the cladding ($n_2 < n_1$);
- θ_i: incident angle;
- θ_r: refracted angle;
- θ_c: critical angle.

TIR occurs when $\theta_i > \theta_c$. At the critical angle $\theta_i = \theta_c$, the refracted ray travel at $\theta_r = 90°$, and the Equation 2.1 simplifies to:

$$\theta_c = arcsin\frac{n_2}{n_1}. \tag{2.2}$$

As illustrated in Figure 2.1, an optical ray incident on the fiber is guided if the angle of incidence falls within the acceptance cone. Let us now go into more detail by applying Snell's law:

$$cos(\theta_c) = \frac{n_2}{n_1}sin(\theta_{max}), \tag{2.3}$$

θ_{max} is the half-angle of the acceptance cone, and by squaring both sides:

$$cos^2(\theta_c) = \frac{n_2^2}{n_1^2}sin^2(\theta_{max}) = 1 - sin^2(\theta_c) = 1 - \frac{n_2^2}{n_1^2} \tag{2.4}$$

the Equation 2.4 becomes:

$$nsin(\theta_{max}) = \sqrt{n_1^2 - n_2^2} = NA, \tag{2.5}$$

where NA is the Numerical Aperture and determines the fiber's ability to collect light from a broader or narrower range of angles.

2.2 Linear properties of optical fibers

2.2.1 Attenuation

Losses occur during light propagation in optical fibers due to material absorption, scattering, and dispersion. These losses are quantified by a parameter known as attenuation. Considering an input beam with initial power P_0 propagating in an optical fiber with a fiber length of L, the output power can be derived from the Beer-Lambert law as [26]:

$$P_T = P_0 exp(-\alpha L), \tag{2.6}$$

where α is the attenuation constant that is commonly used to measure the power loss per unit length in dB/km:

$$\alpha_{dB} = -\frac{10}{L} log\left(\frac{P_T}{P_0}\right). \tag{2.7}$$

The most common material for fabricating optical fiber is silica, which can be easily drawn into thin fibers at low cost. However, silica has microscopic density fluctuations that cause light to be deflected by Rayleigh scattering. These losses increase dramatically at shorter wavelengths because Rayleigh scattering has a strong wavelength dependence proportional to λ^{-4}, as illustrated in Figure 2.2 [26, 27].

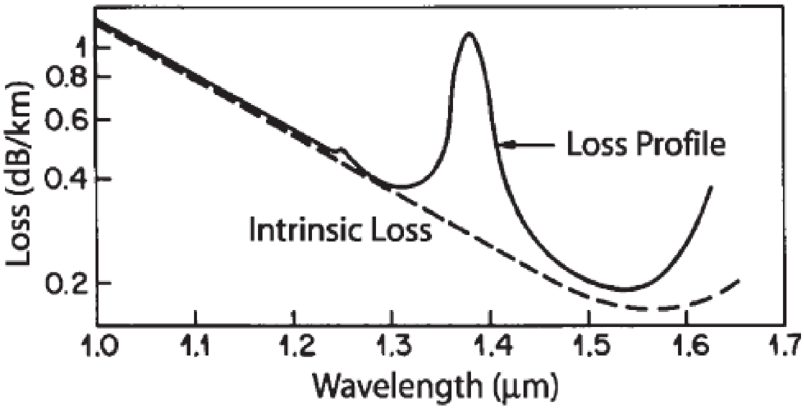

Figure 2.2: Loss spectrum of a silica SMF. The dashed curve is the contribution resulting from Rayleigh scattering [27]. Reprinted from [26].

2.2.2 Chromatic dispersion

Chromatic dispersion arises from the interaction between an electromagnetic wave and the bound electrons of a dielectric medium. The response of the medium generally depends on the optical frequency (ω), leading to a frequency-dependent of the refractive index ($n(\omega)$). The refractive index is approximated using the Sellmeier equation [26]:

$$n^2(\omega) = 1 + \sum_{j=1}^{m} \frac{B_j \omega_j^2}{\omega_j^2 - \omega^2}, \tag{2.8}$$

where ω_j is the resonance frequency of the jth oscillator, and B_j is the strength of the jth corresponding resonance. Dispersion is particularly significant for short pulses because the frequency-dependent refractive index causes different spectral components of the pulse to propagate at varying speeds ($c/n(\omega)$) [26]. Figure 2.3 illustrates the refractive index of bulk-fused silica as a function of wavelength.

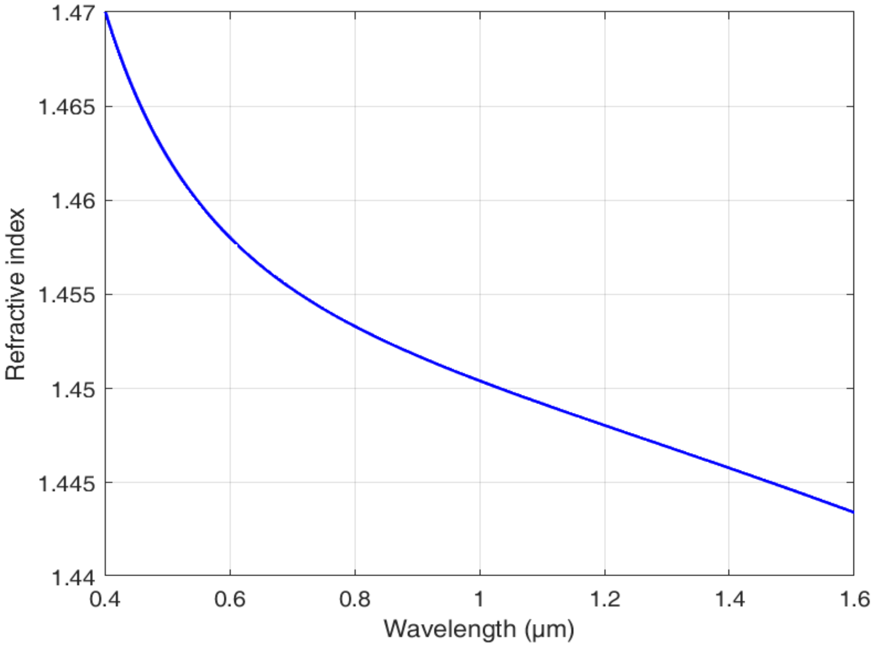

Figure 2.3: Refractive index of bulk-fused silica as a function of wavelength, calculated from the Sellmeier equation.

Optical fibers guide light in discrete modes, each mode characterized by an effective refractive index (n_{eff}). The n_{eff} depends on the spatial field distribution of the mode, the fiber geometry structure, and the wavelength of the propagating light. The effects of fiber dispersion are described by the parameter $\beta = n(\omega)\omega/c$, whose Taylor expansion is:

$$\beta(\omega) = n(\omega)\frac{\omega}{c} = \beta_0 + \beta_1(\omega - \omega_0) + \frac{1}{2}\beta_2(\omega - \omega_0)^2 + ..., \tag{2.9}$$

where:

$$\beta_m = \left(\frac{d^m\beta}{d\omega^m}\right)_{\omega=\omega_0} \quad (m = 0, 1, 2, 3, ...) \tag{2.10}$$

the β_m are coefficients related to the dispersion characteristics of the medium. β_1 the group delay parameter, which describes the time delay of the pulse with an unchanged shape, is given by [26]:

$$\beta_1 = \frac{1}{c}\left(n + \omega\frac{dn}{d\omega}\right), \tag{2.11}$$

its units are s/m. The second derivative of Equation 2.10 is given by:

$$\beta_2 = \frac{1}{c}\left(2\frac{dn}{d\omega} + \omega\frac{d^2n}{d\omega^2}\right), \tag{2.12}$$

β_2 is the Group Velocity Dispersion (GVD) parameter, expressed in units of s^2/m. It characterizes the frequency dependence of the group velocity, which causes a time delay between the different spectral components of short pulses, leading to temporal broadening. A practical representation of dispersion in short pulses is through the relationship between β_1, β_2, and the dispersion parameter D expressed in units of $ps/km \cdot nm$, given by:

$$D = \frac{d\beta_1}{d\lambda} = -\frac{2\pi c}{\lambda^2}\beta_2 = -\frac{\lambda}{c}\frac{d^2n}{d\lambda^2}. \tag{2.13}$$

Figure 2.4 illustrates D (blue curve) and β_2 (red curve) for bulk-fused silica as a function of wavelength, derived from Equations 2.12 and 2.13. A solid horizontal line at 0 and a dashed line at 1.27 μm indicate the Zero Dispersion Wavelength (ZDW), where the material exhibits no chromatic dispersion, meaning different wavelengths travel at the same speed.

Dispersion can be described in two different regimes. In the normal dispersion regime. $\beta_2 > 0$ and wavelengths $\lambda<\lambda_{ZDW}$, high-frequency (short wavelength) components of an optical pulse travel slower than low-frequency (long wavelength) components. Conversely, in the anomalous dispersion $\beta_2 < 0$ and wavelengths $\lambda>\lambda_{ZDW}$, the opposite effect occurs: low-frequency (long wavelength) components travel slower than the high-frequency (short wavelength) components [26].

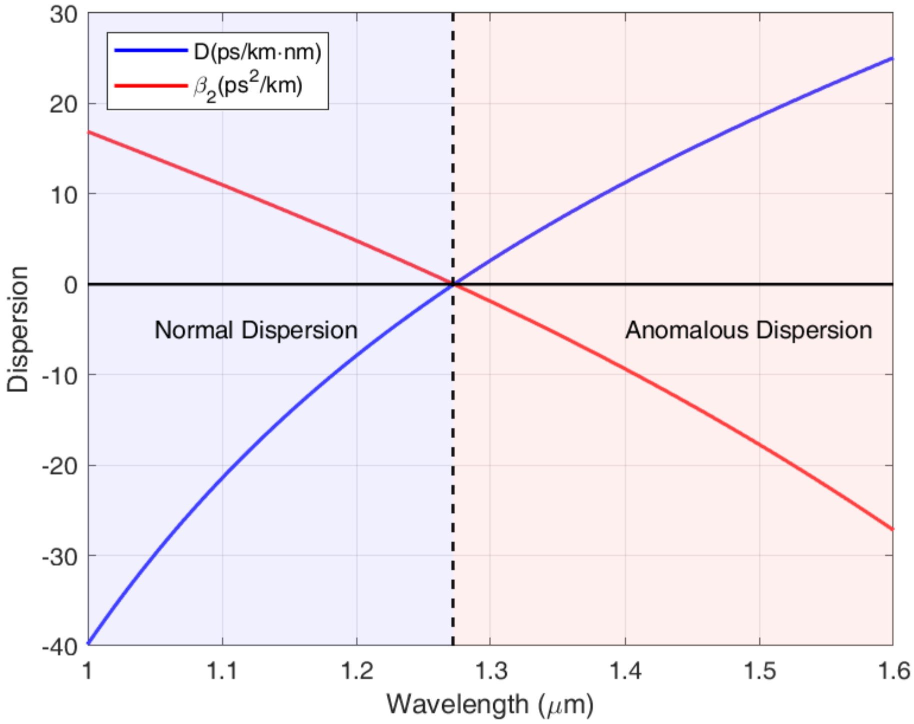

Figure 2.4: Variation of D and β_2 for bulk-fused silica as a function of wavelength. ZDW at 1.27 μm, with normal dispersion region in the blue-shaded region (1.00-1.27 μm) and anomalous dispersion in the red-shaded region (1.27-1.60 μm) [26].

2.3 Different types of optical fibers

2.3.1 Single-Mode Fibers and Multimode Fibers

Optical fibers are classified as *Step-index fibers*, where the refractive index between the core and cladding is constant, and *Graded-Index (GRIN) fibers*, which have a continuous parabolic variation of the refractive index from the cladding to the core center.

Step-index fibers, can be further divided into *Single-Mode Fiber (SMF)* and *Multimode Fiber (MMF)*. SMFs are designed to carry a single mode along long distances, as illustrated in Figure 2.5a. To achieve this, the core diameter is typically small, around 8-10 μm, and the cladding diameter is around 125 μm.

The single-mode operation occurs when the normalized frequency V is less than or equal to 2.405, and it is determined by the equation [26]:

$$V = \frac{2\pi\rho}{\lambda} NA, \tag{2.14}$$

where ρ is the core radius, λ is the wavelength of light.

In contrast to SMF, MMFs are designed to carry the propagation of multiple transverse optical modes [26]. The core diameter is larger than SMFs, typically around 50-200 μm. In step-index MMFs, light rays propagate in a zigzag pattern due to TIR, with multiple reflections at different angles, as shown in Figure 2.5b.

The V-number for step-index MMFs can be approximated by:

$$M \approx \frac{V^2}{2}. \tag{2.15}$$

In contrast, GRIN fibers the light propagates in a sinusoidal path due to the gradual change in the core refractive index [26], as illustrated in Figure 2.5c. And the V-number is $M \approx \frac{V^2}{4}$. This thesis focuses on single-mode propagation, while MMFs are utilized for beam collection and subsequent analysis within the optical apparatus.

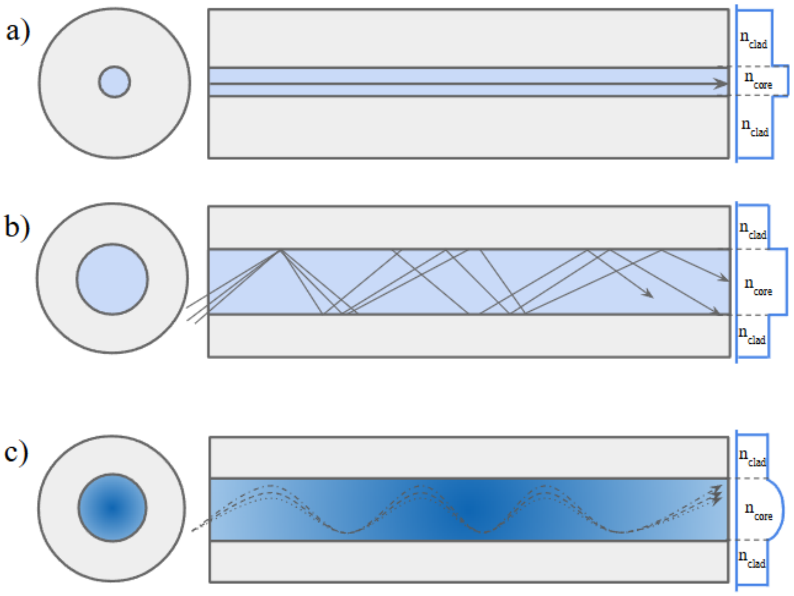

Figure 2.5: Optical fiber designs with optical rays propagation. a) SMF, b) Step-index MMF, and c) GRIN MMF.

2.3.2 Polarization-Maintaining fiber

Polarization-Maintaining (PM) fibers are a specialized type of SMF designed to preserve the polarization state of light as it propagates through the optical fiber. The most common type of PM is PANDA fiber, which has the simplest design to manufacture and has low losses compared to other PM fibers, such as bow-tie or elliptical-core fibers [28]. Figure 2.6 illustrates the most common PANDA fibers design, which consists of two stress rods on each side of the core employed to create an asymmetrical waveguide that induces birefringence. The birefringence maintains the polarization of the propagating light by differentiating the refractive indices along orthogonal axes.

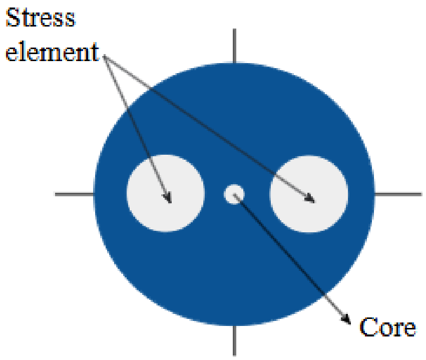

Figure 2.6: Profile of the PANDA PM fiber. The two larger circles represent the stress roads, and the small circle represents the core.

PM fibers are commonly used for the development of fiber lasers due to the lack of additional polarization state controllers and environmental stability, making them required for various applications [29–33].

2.3.3 Photonic Crystal Fiber

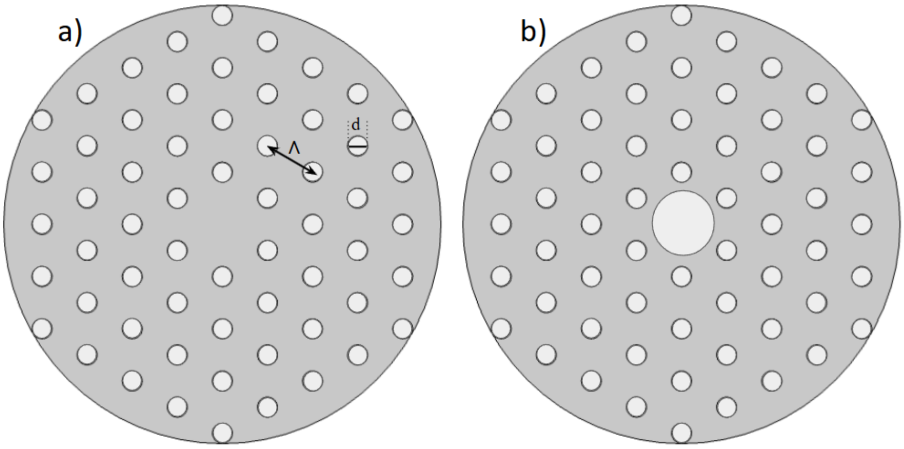

Figure 2.7: PCF cross-sections. a) Solid-core and b) hollow-core. The parameters pitch Λ and hole size diameter *d*.

Photonic Crystal Fibers (PCFs) were first manufactured in 1997 by P. Russell et al.. Russell's work demonstrated an optical fiber with a central core surrounded by a 2D photonic crystal structure consisting of a hexagonal array of air holes on the micrometer scale [34]. PCFs can be fabricated to exhibit normal or anomalous dispersion, which is determined by design parameters such as the size of the air holes, the distance between the holes, the materials used, the NA, and other structural features. Thus, they can present high nonlinear properties used for Supercontinuum

Generation (SCG), thus building multicolor light sources. PCFs are classified into primary categories: *solid-core* and *hollow-core*.

In solid-core PCF, light propagates through the high refractive index contrast between the core and cladding [35,36]. The core is typically made of silica, while the cladding, with an air-hole lattice, ensures a lower average refractive index. Figure 2.7a illustrates an example of a solid-core PCF. The parameter d is the diameter of the air hole lattice, and Λ represents the pitch, defined as the center-to-center distance between the air holes.

Figure 2.7b illustrates an example of a hollow-core PCFs. The refractive index of the core is lower than in the cladding [37]. The core is typically filled with air or a low-index gas, while the cladding is made of a two-dimensional photonic crystal structure with an array of air holes. This periodic dielectric arrangement generates a photonic bandgap (PBG), enabling efficient light guidance through the hollow core.

2.3.4 PCFs employed in this work

All the optical fibers used in the developed light sources are PM fibers to ensure environmental stability and eliminate the need for polarization controllers. In this work, two different PCFs were used: Nonlinear (NL)-NEG-PM-1050 and Large-Mode-Area (LMA)-PM-5 (both from NKT Photonics).

Figure 2.8a presents the cross-section of the first fiber (NL-NEG-PM-1050-1), achieved from a scanning electron microscope (SEM), provided by dr. eng. Wojciech Nogala, group Nanoelectrochemistry, Institute of Physical Chemistry. As we can see, it presents a solid hexagonal structure with a core diameter of approximately 2.3 ± 0.3 μm. Figure 2.8b illustrates the dispersion curve provided by the manufacturer. The curve does not cross the zero, having all-normal dispersion properties. The interest is to generate SC in all normal dispersion because it enables the generation of a broad and coherent spectrum without the formation of solitons effects.

Figure 2.9a presents instead an SEM image of cross-section of the second fiber (LMA-PM-5) also provided by dr. eng. Wojciech Nogala. This fiber has a larger core diameter of approximately 5.0 $\pm 0.5\mu$m. The dispersion curve is displayed in Figure 2.9b, which the data was provided by the manufacturer. The LMA-PM-5 fiber has a ZDW of around 1050 nm.

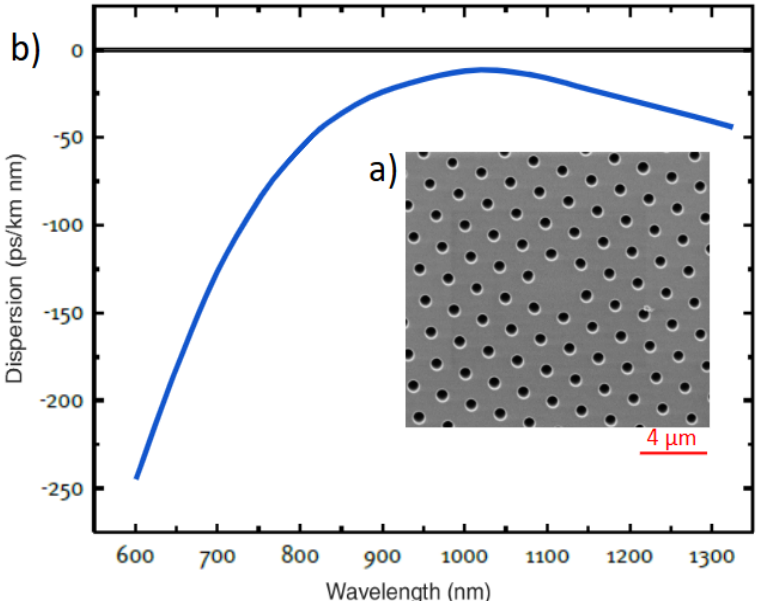

Figure 2.8: NL-NEG-1050-1 a) cross-section from SEM and b) dispersion curve provided by NKT Photonics.

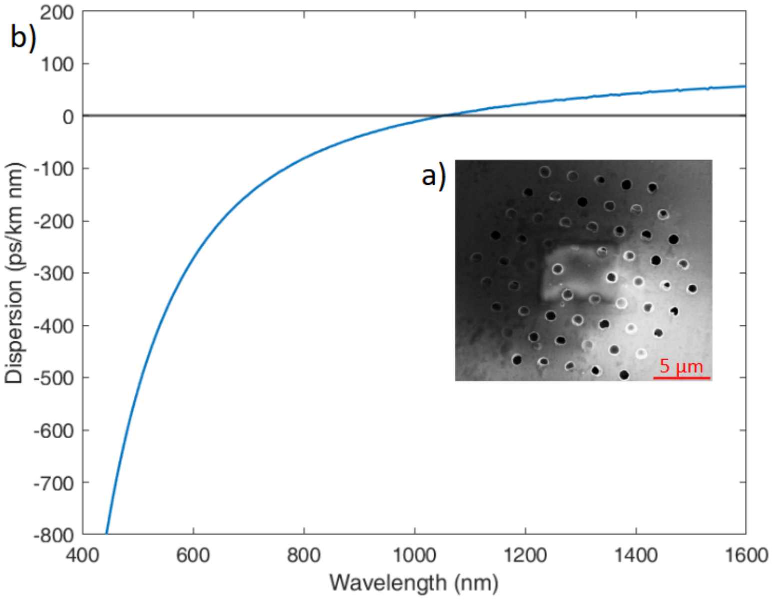

Figure 2.9: LMA-PM-5 a) cross-section from SEM and b) dispersion curve provided by NKT Photonics with a ZDW at around 1050 nm.

Chapter 3

Nonlinear effects in optical fibers

Optical fibers are widely used for generating various spectral and temporal nonlinear effects, which are then employed in numerous applications, including nonlinear imaging. This chapter introduces the fundamental principles of selected nonlinear effects, chosen to facilitate understanding of the work conducted within the scope of this thesis, as discussed in the subsequent chapters.

3.1 Kerr nonlinearity

The nonlinear effects are generated when intense light propagates through a medium, e.g. an optical fiber. The interaction between the electrons in the medium and the intense electric field of the light alters the optical properties of the medium. Kerr effect is one of the most common third-order nonlinear effect [38–40], which causes a change in the refractive index in response to applied electric field, as follows:

$$n(I) = n_0 + n_2 I = n_0 + \bar{n}_2 |E|^2, \tag{3.1}$$

where n_0 is the linear refractive index, n_2 is the nonlinear refractive index, $\bar{n}_2$ is the nonlinear refractive index coefficient, and E is the electric field related to the optical intensity (I). These refractive indices can be derived from the fundamental relation between the medium polarization and the electric field of the light. The polarization $\vec{P}$ induced in the medium can be described in terms of a Taylor expansion as:

$$\vec{P}(z,t) = \epsilon_0 \chi^{(1)} \vec{E}(z,t) + \epsilon_0 \chi^{(2)} \vec{E}(z,t)^2 + \epsilon_0 \chi^{(3)} \vec{E}(z,t)^3 + ..., \tag{3.2}$$

where ϵ_0 is the vacuum permittivity, and $\chi^{(n)}$ is the electrical susceptibility tensor of index h of the medium, where $\chi^{(1)}$ is the linear susceptibility tensor describing the linear response of the material to the $\vec{E}$. The $\chi^{(2)}$ and $\chi^{(3)}$ and so on, are higher-order susceptibilities tensors that account for the nonlinear response of the material.

We will simplify an approach by considering such tensors as simple coefficients by assuming that induced $\vec{P}$ and $\vec{E}$ are both linearly polarized. When considering light propagating in an optical fiber, z represents the propagation coordinate and t is the time domain.

In the slowly varying envelope approximation, if we assume a linear polarization along $\hat{x}$, we can write the electric field ($\vec{E}$), as follows:

$$\vec{E}(z,t) = \frac{1}{2}\hat{x}\Big[E(z,t)e^{-i\omega_0 t} + c.c\Big], \tag{3.3}$$

where *c.c* is the abbreviation of complex conjugate and $E(z,t)$ is the slowly varying envelope. Same procedure can be applied for the induced polarization:

$$\vec{P}(z,t) = \frac{1}{2}\hat{x}\Big[P(z,t)e^{-i\omega_0 t} + c.c\Big]. \tag{3.4}$$

The total polarization can be described as:

$$\vec{P} = \vec{P}_L + \vec{P}_{NL}, \tag{3.5}$$

where $\vec{P}_L$ and $\vec{P}_{NL}$ are the linear and nonlinear induced polarization.

Considering a centrosymmetric medium with an absence of second-order nonlinearity, the slowly varying part of the induced polarization is:

$$P(z,t) = \epsilon_0 \chi_{eff} E(z,t), \tag{3.6}$$

where the effective susceptibility is:

$$\chi_{eff} = \chi^{(1)} + \frac{3}{4}\chi^{(3)}|E(z,t)|^2 = \chi_{eff-L} + \chi_{eff-NL}. \tag{3.7}$$

Thus

$$P(z,t) = \epsilon_0 \chi^{(1)} E(z,t) + \epsilon_0 \frac{3}{4}\chi^{(3)}|E(z,t)|^2 E(z,t) = P_L + P_{NL}. \tag{3.8}$$

Since

$$\begin{aligned} n &= (1+\chi_{eff})^{1/2} = (1+\chi_{eff-L}+\chi_{eff-NL})^{1/2} \\ &= (1+\chi^{(1)} + \frac{3}{4}\chi^{(3)}|E(z,t)|^2)^{1/2}, \end{aligned} \tag{3.9}$$

where

$$n_0 = (1+\chi^{(1)})^{1/2} \tag{3.10}$$

the nonlinear-index coefficient ($\bar{n}_2$) is related to the third-order susceptibility $\chi^{(3)}$ by:

$$\bar{n}_2 = \frac{3\chi^{(3)}}{8n_0}. \tag{3.11}$$

The optical intensity, related to the electric field (E), is given by:

$$I = \frac{1}{2}\epsilon_0 c n_0 |E|^2, \tag{3.12}$$

with c being the velocity of light in vacuum. Thus, the nonlinear index n_2 is given by:

$$n_2 = \frac{2\bar{n}_2}{\epsilon_0 c n_0}. \tag{3.13}$$

The Kerr effect is responsible for the generation of several nonlinear effects, including Self-Phase Modulation (SPM), Cross-Phase Modulation (XPM), Supercontinuum Generation (SCG), Four-Wave Mixing (FMW), which will be discussed in more detail below.

3.2 Self-Phase Modulation

Self-phase modulation (SPM) is a consequence of the Kerr effect. This effect was first observed in a cell filled with CS_2 [41] and later in silica fibers [42, 43]. Let us consider an ultrashort Gaussian pulse with its intensity described as [26]:

$$I(t) = I_0 exp\left(-\frac{t^2}{T_0^2}\right), \tag{3.14}$$

where I_0 is the peak intensity, t is time and T_0 is the half pulse duration measured at $exp(-1)$ in intensity. The time-varying refractive index is given by:

$$\frac{dn(I)}{dt} = n_2\frac{dI}{dt} = n_2 I_0\left(\frac{-2t}{T_0^2}\right) exp\left(\frac{-t^2}{T_0^2}\right). \tag{3.15}$$

The variation in the refractive index generates a shift in the instantaneous phase of the pulse cumulated along a propagation distance (z):

$$\phi(t) = \frac{2\pi}{\lambda_0} n(I) z - \omega_0 t, \tag{3.16}$$

where ω_0 is the carrier frequency and λ_0 is the vacuum wavelength of the pulse. The phase shift results in a frequency shift of the pulse with the instantaneous frequency ($\omega(t)$) as:

$$\omega(t) = \frac{\partial\phi}{\partial t} = -\omega_0 + \frac{2\pi}{\lambda_0} z \frac{dn(I)}{dt} = -\omega_0 + \frac{2\pi}{\lambda_0} z n_2 \frac{dI}{dt} \tag{3.17}$$

$$\omega(t) = -\omega_0 - \frac{4\pi n_2 I_0 t}{\lambda_0 T_0^2} exp\left(\frac{-t^2}{T_0^2}\right). \tag{3.18}$$

As described by Equation 3.17, the instantaneous frequency is proportional to the time derivative of the instantaneous input pulse power and is, therefore, influenced by the pulse shape. In silica, this leads to a frequency downshift at the front edge of the pulse and an upshift at the back edge, as schematically illustrated in Figure 3.1.

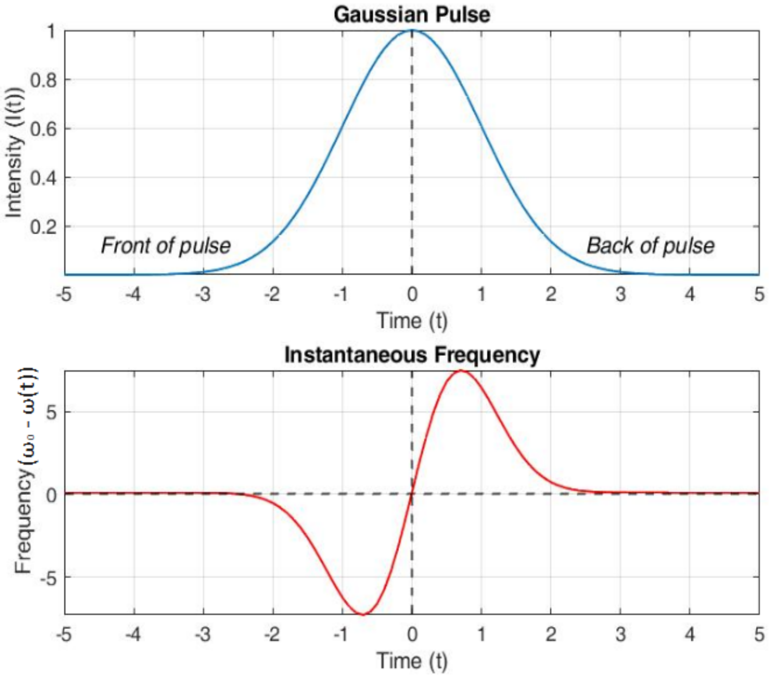

Figure 3.1: Gaussian pulse (top) and its instantaneous frequency after propagation through a nonlinear medium (bottom).

3.3 Optical Wave Breaking

A nonlinear phenomenon that arises due to the interaction between the SPM and GVD ($\beta_2 > 0$, Chapter 2, Section 2.2.2) is called Optical Wave Breaking (OWB) [44]. The SPM generates low frequencies in the front of the pulse and high frequencies in the back of the pulse. Simultaneously, the positive GVD causes the low-frequency components to travel faster than the high-frequency components, which leads to a breakdown of the pulse shape at a distance known as L_{WB} (WB, wave breaks), resulting in a pulse temporally stretched, forming an ”S” [26,45]. Figure 3.2 illustrates the calculated plot of the OWB as the pulse propagates in a fiber length z. At the L_{WB}, the sidelobes appear, which stop the spectral broadening.

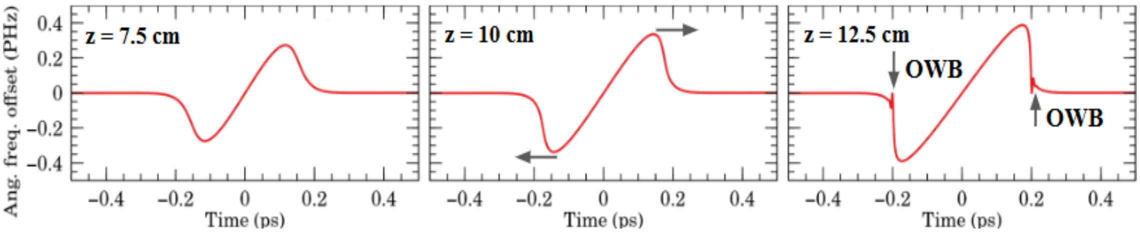

Figure 3.2: OWB evolution, sidelobes appear at the fiber length z=12.5 cm.

3.4 Four-Wave Mixing

Four-Wave Mixing (FWM) is a third-order parametric process that involves the nonlinear interaction among four optical waves, in which the energy and momentum of the income photons are conserved. FWM is a phase-sensitive process, where the efficiency depends on the phase-matching conditions. To occur the FWM, a specific choice of input wavelengths and fiber parameters is required. Considering the electric field polarized along the x-axis:

$$\vec{E} = \frac{1}{2}\hat{x}\sum_{j=1}^{4} E_j exp[i(\beta_j z - \omega_j t)] + c.c., \tag{3.19}$$

where $\beta_j = \frac{\tilde{n}_j \omega_j}{c}$ is the propagation constant and $\tilde{n}_j$ is mode index referred to wave j. z is the distance propagation. The induced nonlinear polarization is given by:

$$\overrightarrow{P_{NL}} = \frac{1}{2}\hat{x}\sum_{j=1}^{4} P_j exp[i(\beta_j z - \omega_j t)] + c.c. \tag{3.20}$$

P_4 can be expressed as:

$$\begin{aligned} P_4 = \frac{3\epsilon_0}{4}\chi^{(3)}_{xxxx}[&|E_4|^2 E_4 + 2(|E_1|^2 + |E_2|^2 + |E_3|^2)E_4 + 2E_1E_2E_3exp(i\theta_+) \\ &+ 2E_1E_2E_3^* exp(i\theta_-) + ...], \end{aligned} \tag{3.21}$$

θ_+ is given by:

$$\theta_+ = (\beta_1 + \beta_2 + \beta_3 - \beta_4)z - (\omega_1 + \omega_2 + \omega_3 - \omega_4)t, \tag{3.22}$$

And θ_- :

$$\theta_- = (\beta_1 + \beta_2 - \beta_3 - \beta_4)z - (\omega_1 + \omega_2 - \omega_3 - \omega_4)t. \tag{3.23}$$

The first four terms of Equation 3.21, which contain E_4, are responsible for the SPM and XPM nonlinear effects. The following terms result from the frequency combinations of all four waves, whose effectiveness depends on the phase mismatch between E_4 and P_4, which are led by θ_+ and θ_-. Thus, in Equation 3.21, there are two types of FWM. The term θ_+ implies the transfer of energy from three photons to a single photon at the frequency $\omega_4 = \omega_1 + \omega_2 + \omega_3$, known as the third-harmonic generation ($\omega_1 = \omega_2 = \omega_3$).

Similarly, the term θ_- indicates that two photons at frequencies ω_1 and ω_2 are annihilated, and two photons at frequencies ω_3 and ω_4 are created simultaneously:

$$\omega_3 + \omega_4 = \omega_1 + \omega_2. \tag{3.24}$$

This process occurs when the phase-matching is achieved by $\triangle k = 0$ where:

$$\triangle k = \beta_3 + \beta_4 - \beta_1 - \beta_2 = (\tilde{n}_3\omega_3 + \tilde{n}_4\omega_4 - \tilde{n}_1\omega_1 - \tilde{n}_2\omega_2)/c, \tag{3.25}$$

$\tilde{n}_j$ is the effective mode index at the frequency ω_j. When $\omega_1 \neq \omega_2$, it requires two pump beams to generate FWM. In the case of $\omega_1 = \omega_2$, a single pump beam can produce FWM. Note that in this particular case, symbols β_1 and β_2 refer to wavenumbers of waves 1 and 2. Note also that the spatial dependence of the field is included using $E_j(x, y, z) = F(x, y)A_j(z, t)$, where $F_j(x, y)$ is the spatial distribution of the jth fiber mode, which influences the effective area of guided mode (A_{eff}) and $A_j(z, t)$ is the complex envelope of electric field. The effective phase mismatch is given by:

$$\kappa = \triangle k + \gamma(P_1 + P_2), \tag{3.26}$$

where $\gamma \approx n_2\omega_j/(cA_{eff})$ and γ representing an average value. P_1 and P_2 are the incident pump powers. The gain responsible for amplification is referred to as parametric gain, determined by the nonlinear interaction and phase mismatch defined as:

$$g = \sqrt{(\gamma P_0 r)^2 - (\kappa/2)^2}, \tag{3.27}$$

where $r = \frac{\sqrt{2P_1P_2}}{P_0}$ and $P_0 = P_1 + P_2$. The parametric gain remains valid if we use $P_1 = P_2 = P_0/2 (r = 1)$:

$$\kappa = \triangle k + 2\gamma P_0. \tag{3.28}$$

Figure 3.3 illustrates the variations of g as a function of $\triangle k$ for values of γP_0. The maximum gain occurs at $\kappa = 0$ or $\triangle k = -2\gamma P_0$. The gain is in the range of $0 > \triangle k > -4\gamma P_0$. The shift of the gain peak $\triangle k = 0$ is attributed to contributions from nonlinear effects such as SPM and XPM to the phase mismatch.

Nevertheless, the FWM effect can be classified into two cases: the non - degenerate (ND) and degenerate (D).

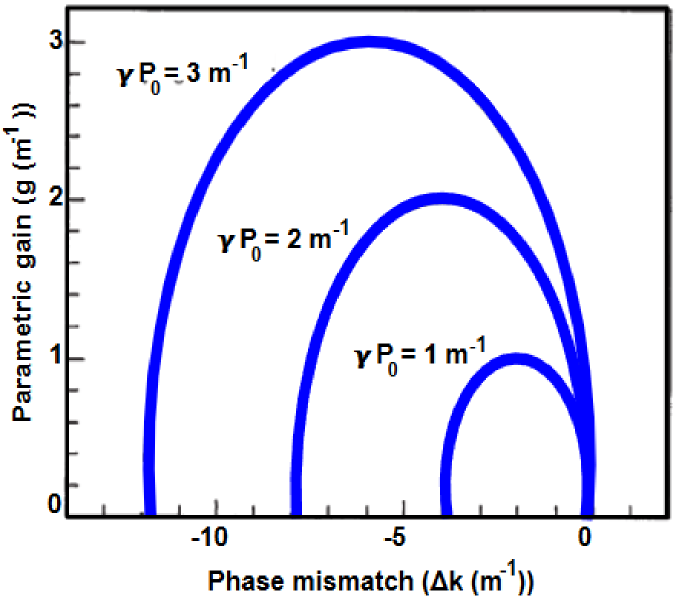

Figure 3.3: Parametric gain as a function of the phase mismatch for different pump powers P_0. The shift is due to the nonlinear effects of SPM and XPM. Reprinted from [26].

ND-FWM occurs when three input waves with distinct frequencies, namely ω_1, ω_2, and ω_3 interact within a nonlinear medium, e.g., a crystal, optical fiber, or semiconductor device. The interaction occurs due to the nonlinear response from the medium, which results in a mixing of the input waves. In this process, the energy from the three photons is transferred to a single photon at the frequency:

$$\omega_4 = \omega_1 + \omega_2 - \omega_3. \tag{3.29}$$

In the D-FWM case, waves with the same frequency interact within a nonlinear medium, denoted by $\omega_1 = \omega_2$. This interaction results in the generation of two waves with the same frequency as the input waves. It can be generated by an intense single pump beam at the frequency ω_1, which generates two sidebands at frequencies ω_3 and ω_4:

$$\omega_1 - \omega_3 = \omega_4 - \omega_1, \tag{3.30}$$

where $\omega_3 < \omega_4$. The low-frequency sideband at ω_3 is known as the Stokes wave, while the high-frequency sideband ω_4 is the anti-Stokes wave.

3.5 Optical soliton

Optical soliton is a phenomenon that arises in optical fibers, occurring in the anomalous dispersion regime due to the interplay between chromatic dispersion and the Kerr effect. The concept was first introduced by S. Russell in 1834, when he observed a water wave propagation undistorted over several kilometers, which he called the *Wave of Translation* [46]. The term soliton was later coined in 1965 by N. Zabusky and M. Kruskal to describe stable wave packets propagating without distortion over long distances [47]. In the context of optical fibers, solitons were first proposed in 1973 by A. Hasegawa and F. Tappert as a solution to the Nonlinear Schrödinger (NLS) equation governing pulse propagation in dispersive media [48].

Soliton is a complex phenomenon that involves advanced mathematical methods. Considering a CW beam propagating in a lossless optical fiber, where the NLS equation governs the behavior of the pulse, given by [26]:

$$i\frac{\partial A}{\partial z} = \frac{\beta_2}{2}\frac{\partial^2 A}{\partial t^2} - \gamma |A|^2 A, \tag{3.31}$$

where $A(z, t)$ is the complex envelope of the optical field, β_2 is the GVD parameter, and γ is the nonlinear coefficient

$$\gamma = \frac{n_2 \omega_0}{c A_{eff}}, \tag{3.32}$$

where A_{eff} is the effective area of the first guided mode.

The inverse scattering method, which treats the problem by analyzing waves scattering off a potential, is utilized to solve the NLS equation [49–51]. This method is somehow analogous to the Fourier transform approach for solving linear partial differential equations. For a fundamental soliton ($N = 1$), the NLS can be solved with a hyperbolic-secant-shaped pulse:

$$A(z, t) = \sqrt{P}_0 sech\left(\frac{t}{T}\right) exp(i\phi(z, t)), \tag{3.33}$$

where P_0 is the peak power. The Full Width at Half Maximum (FWHM) pulse duration is approximately 1.7627 times the parameter T. The soliton order parameter is described as:

$$N^2 = \frac{\gamma P_0 T^2}{|\beta_2|}. \tag{3.34}$$

For fundamental solitons, SPM induces phase shifts that are balanced with GVD in a way that the pulse shape and the pulse spectrum do not change on propagation [26]. With $N = 1$, the Equation 3.34 becomes:

$$P_0 = \frac{|\beta_2|}{\gamma T^2}. \tag{3.35}$$

For higher-order solitons ($N > 1$), the SPM dominates, but after the GVD leads the pulse contraction, which causes periodic oscillations during the pulse propagation [26].

3.6 Stimulated Raman Scattering

Stimulated Raman Scattering (SRS) in optical fibers occurs when an intense pump wave interacts with the fiber medium, resulting in a shifted frequency wave known as the Stokes wave. This phenomenon is due to the inelastic scattering of photons that transfer energy to the vibrational modes of the optical fiber. In the CW and quasi-CW conditions, the initial growth of the Stokes wave is given by [52]:

$$\frac{dI_s}{dz} = g_R I_p I_s, \tag{3.36}$$

where I_s represents the Stokes intensity, I_p is the pump intensity, and g_R is the Raman-gain coefficient, being related to the cross-section of spontaneous Raman scattering [53]. The Raman-gain coefficient at the frequency difference between the pump and Stokes waves is denoted by $g_R(\Omega)$, where $\Omega \equiv \omega_p - \omega_s$. The $g_R(\Omega)$ is an important parameter to describe SRS, which was first used to measure in silica fibers [54, 55].

The gain coefficient g_R depends on the fiber properties and the pump and Stokes waves, e.g., if they are co-polarized or orthogonally polarized [26]. Figure 3.4 illustrates the g_R for fused silica as a function of the frequency shift at the pump wavelength 1 μm. The Raman gain in silica fibers has a broader frequency range of 40 THz with a maximum peak near 13 THz [26]. Different from crystalline materials, silica fibers are amorphous materials with a disordered molecular structure that spread out into bands, creating a continuum that leads to the observed extended Raman gain spectrum [56].

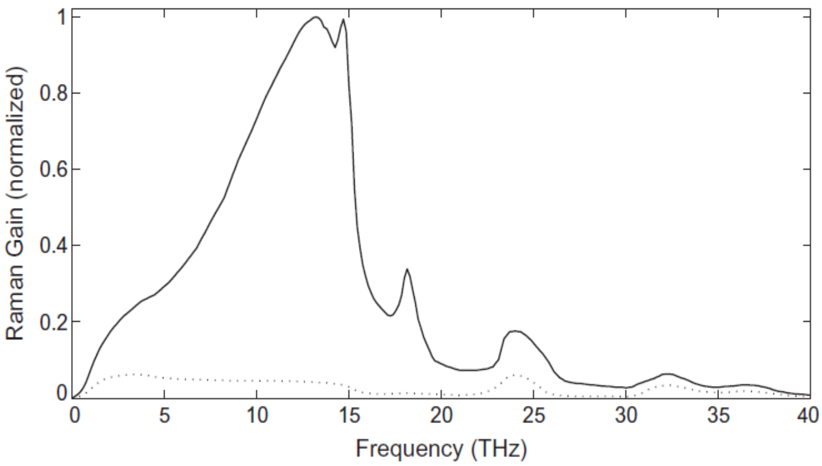

Figure 3.4: Raman gain for fused silica. The solid curve represents when the pump and Stokes waves are co-polarized. The dotted curve illustrates the pump and Stokes waves are orthogonally polarized. Reprinted from [26].

The fiber length needs to be sufficiently long, and the input power needs to be high enough to initiate the SRS process. It is often observed in systems such as Neodymium (Nd):Yttrium Aluminum Garnet (YAG) lasers, Ytterbium (Yb)-doped fiber lasers, high-power CW lasers, and high-power pulsed lasers.

3.7 Supercontinuum Generation

Supercontinuum Generation (SCG) is a combination of various nonlinear effects, such as SPM, FWM, OWM, solitons, and Raman scattering, that occurs when ultrashort optical pulses propagate through highly nonlinear materials. The nonlinear effects affect the temporal and spectral evolution, contributing to the broadening of the optical spectrum. Concurrently, the dispersive properties of the material influence the propagation of different spectral components, further shaping the evolving pulse.

The first observations of SCG were made in 1967 by F. Shimizu in gaseous nonlinear media [41] and by R. Alfano and S. Shapiro in bulk glass [57]. However, the first experiment utilizing optical fibers occurred later, in 1976, where pulses from a dye laser were directed into a 20 m fiber, resulting in a spectral broadening over 180 nm [58]. In 1987, an experiment using a 25 ps laser injected into a 15 m fiber achieved spectral broadening of up to 50 nm [59]. Also, in 1987, another experiment employed a 1 km segment of SMF and an 830 fs laser, achieving a broadening of approximately 200 nm [60]. Further experiments using longer pulses have since been demonstrated [61,62].

The development of PCFs in 2000 marked a significant advancement in various optical fields, especially when used for propagating nonlinear effects [35,37,63]. In contrast to traditional MMF or SMF, where SCG typically requires longer lengths when using picosecond lasers, microstructure fibers achieve SCG with shorter lengths [64–66]. Furthermore, with the development of femtosecond lasers, SCG can be generated within tens of centimeters of microstructure fibers [9,67].

SCG is strongly dependent on the fiber parameters and characteristics of the input beam. Studies have demonstrated that a broad SC is most effectively generated when pumping wavelengths are close to the Zero Dispersion Wavelength (ZDW) [68,69]. The dispersive regimes play an important role in spectral broadening. As mentioned in Chapter 2, Section 2.2.2, there are two dispersive regimes:

- Normal dispersive regime, when $\beta_2 > 0$ and the wavelengths satisfy $\lambda < \lambda_{ZDW}$. The high-frequency components of an optical pulse travel slower than the low-frequency components [26].

  In this case, SCG is initiated by SPM and OWB effects for fs pulses. As the pulse duration increases, FWM and Raman scattering dominate spectral broadening:

- FWM becomes more efficient with ps and ns pulses because higher temporal coherence and narrower bandwidth facilitate phase-matching conditions.

- Raman scattering, the larger total energy over longer interaction times generates strong Raman Stokes components, significantly contributing to spectral broadening [70].

- Anomalous dispersive regime, when $\beta_2 < 0$ and wavelengths satisfy $\lambda > \lambda_{ZDW}$. The high-frequency components of an optical pulse travel faster than the low-frequency components [26].

  In this case, SCG is dominated by soliton dynamics for fs pulses. Key mechanisms include:

  - Soliton fission, where higher-order solitons break into fundamental solitons, which drives the spectral broadening followed by the Raman-induced redshifts.

  - For ps and ns pulses, modulation instability (MI) initiates the generation of sidebands, which evolve into soliton dynamics, leading to spectral broadening. However, MI is noise-sensitive, which results in an incoherent SC spectrum.

  - The Raman scattering further broadens the spectrum as pulse duration increases [70].

Pulse duration	**Dispersion regime**	**Nonlinear effects**
Femtosecond (<1 ps)	Anomalous ($\beta_2 < 0$)	Soliton fission, dispersive waves
	Normal ($\beta_2 > 0$)	SPM
Picosecond (1 ps–1 ns)	Anomalous ($\beta_2 < 0$)	MI, soliton dynamics
	Normal ($\beta_2 > 0$)	SPM, OWB, FWM, Raman scattering
Nanosecond (>1 ns)	Anomalous ($\beta_2 < 0$)	MI, Raman scattering
	Normal ($\beta_2 > 0$)	Raman scattering, FWM

Table 3.1: Characteristics of the SCG dynamics [70].

Table 3.1 summarizes the characteristics of the SCG dynamics. The pulse duration here was classified into three categories: femtosecond pulses (<1 ps), picosecond pulses (1 ps-1 ns), and nanosecond pulses (>1 ns). The SC spectrum is coherent in both dispersion regimes due to the soliton fission and SPM for femtosecond pulses. However, as the pulse duration increases, the coherence becomes limited due to MI. The SC becomes incoherent and noisy for longer pulses as noise-sensitive effects like MI and Raman scattering dominate.

Chapter 4

Coherent Raman Scattering Microscopy

The Raman Scattering was discovered in 1928 by Sir C. Raman and K. Krishnan [71]. Raman's experiment used sunlight as the source, a telescope as the collector, and his own eyes as the detector. The experiment involves the interaction between light and matter, resulting in the inelastic scattering of photons, which means a change in the energy of the scattered photons. In 1960, Raman's experiment was improved with advancements in instrumentation, particularly with the introduction of laser sources [72–74]. The use of lasers provides high-intensity, monochromatic, and coherent light, improving the sensitivity and precision of Raman measurements. This innovation enabled the development of advanced Coherent Raman Scattering Microscopy (CRS) microscopy techniques.

Raman microscopy offers noninvasive, label-free chemical imaging of biological samples with high spatial resolution and molecular specificity by providing chemical information based on specific vibrational peaks.

Spontaneous Raman Scattering (SpRS) is an inelastic scattering process in which pump photons at ω_p interact with the molecular vibrations of the sample. This interaction leads to energy shifts in the scattered light, producing Stokes photons at ω_S that are emitted in all directions without phase coherence.

In contrast, CRS is a nonlinear optical process that arises from the third-order polarization ($P^{(3)}$) induced in the sample. It is governed by the interaction of incident light fields with the third-order susceptibility ($\chi^{(3)}$) of the material. CRS requires at least two synchronized light beams: the pump beam at ω_p and the Stokes beam at ω_S. The frequency difference between these beams $\Omega = \omega_p - \omega_S$ matches the molecular vibrational frequencies, driving coherent molecular vibrations in the sample.

Compared to SpRS, CRS generates much stronger vibrationally sensitive signals, enabling faster scanning, a critical advantage for imaging applications. CRS also offers finer control over the Raman response of materials. The most commonly used CRS techniques are Stimulated Raman Scattering (SRS) and Coherent anti-Stokes Raman scattering (CARS).

This Chapter will discuss the fundamental principles of the SpRS, SRS, and CARS techniques, highlighting their differences and particularities.

4.1 Spontaneous Raman Scattering

The Spontaneous Raman Scattering (SpRS) process occurs when a quasi-monochromatic laser light at a frequency ω_p excites a molecule to a virtual state, which is then relaxed to the ground state, emitting a spontaneous photon, corresponding ω_S. As illustrated in Figure 4.1, the $\omega_S = \omega_p - \Omega$ is down-shifted in frequency by the molecular vibration at frequency Ω, which is specific to the vibrational frequency of the chemical bonds of the probed molecule. The SpR signal corresponds to discrete bands, constituting a broad spectrum with the pump light frequency [75].

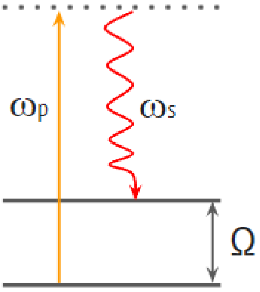

Figure 4.1: Schematic of the energy levels of the SpRS process.

Measurement method based on SpRS uses visible or Near-Infrared (NIR) radiation to probe the vibrational modes of molecules, enabling the identification of selective chemical bonds for the investigation of molecular conformations. In the field of biomedical sciences, it is often used to distinguish normal cells from carcinogenic ones, as variations in protein structures, nucleic acids, and lipids in cancer cells result in distinct biochemical compositions that can be detected through SpR spectroscopy [76].

Nevertheless, SpR microscopy suffers from a low scattering cross-section, around 10-12 orders of magnitude lower than the absorption cross-section of molecules [77]. This limitation arises because most photons are elastically scattered, which makes it difficult to detect the less numerous inelastically scattered photons responsible for the Raman signal. Consequently, SpRS requires long integration times to obtain a single Raman spectrum, as only one photon in a million is inelastically scattered [78].

SpRS is commonly used for applications where time is not a critical parameter, such as chemical and material analyses, in which the identification of molecular compounds is based on the vibrational spectra [79]. It can also distinguish between different polymorphs used in material science to analyze polymers, semiconductors, and pharmaceuticals [80].

4.2 Stimulated Raman Scattering

Stimulated Raman Scattering (SRS) phenomenon was first discovered by E. Woodbury [81] and next confirmed by G. Eckjardt [82] in 1962. It was later popularized as a time-resolved technique through the work of R. Mathies et al. [83] and as an SRS-based microscopy technique through contributions of S. Xie et al. [84, 85].

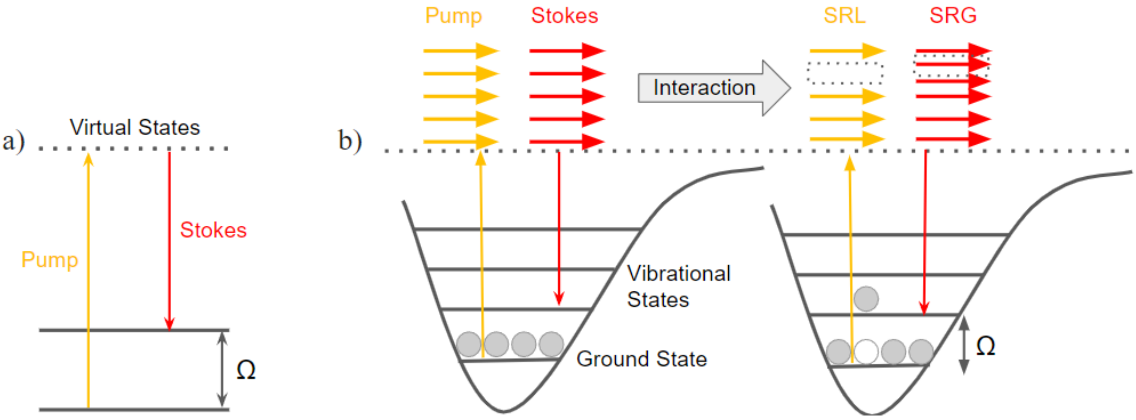

Figure 4.2: a) Schematic of energy levels of the SRS process and b) SRS as an energy transfer process of molecules.

The SRS phenomenon occurs when two excitation fields at a pump frequency ω_p and Stokes frequency ω_S interact within the sample, and if the difference frequency of the excitation beams $\Delta\omega = \omega_p - \omega_S$ matches with the vibration frequency of the molecular transition, as illustrated in Figure 4.2a. A pump photon is absorbed by the sample, and a Stokes photon is generated, which results in Stimulated Raman Loss (SRL) characterized by simultaneous pump-field attenuation and in Stimulated Raman Gain (SRG) characterized by Stokes-field amplification as presented in Figure 4.2b. The transmitted intensities are described by the equation [78]:

$$\Delta I_p \propto -N \cdot \sigma_{Raman} \cdot I_p \cdot I_S \tag{4.1}$$

$$\Delta I_S \propto N \cdot \sigma_{Raman} \cdot I_p \cdot I_S \tag{4.2}$$

where N is the number of molecules in the probe volume and σ_{Raman} is the molecular Raman scattering cross-section. The $\Delta I_S \propto N$ means that the signal is proportional to the concentration of an analyte. Optical signals with quadratic or higher-order dependency on the intensity are classified as nonlinear techniques. In

SRS, the signal intensity depends in a nonlinear way on the power of the excitation pump and Stokes beams [78].

In SRS microscopy, measurements are performed based on detecting the gain (ΔI_S) and loss (ΔI_p) in the intensity of the excitation beams, resulting from an energy transfer between the optical fields and the sample. Thus, SRS does not suffer from non-resonant background signals, as a non-resonant process has no real vibrational modes that match the energy difference between the pump and Stokes beams. Table 4.1 compares the SpRS and SRS processes, highlighting the advantages of each process.

Spontaneous Raman Scattering	**Stimulated Raman Scattering**
Incoherent process, scattered photons are emitted isotropically	Coherent process, scattered photons are directional and phase-matched
Single-photon process	Multi-photon process
One laser source	Two synchronized laser beams (pump and Stokes)
Weaker signal	Stronger signal
Signal vulnerable to auto-fluorescence	Immune to auto-fluorescence, no non-resonant background
Slow imaging, usually tens of seconds/pxl	Fast imaging with a video-rate speed
Full spectra	Selected spectral information

Table 4.1: Comparison between SpRS and SRS techniques [78].

4.2.1 SRS Detection System

In the detection system, SRL is usually detected instead of SRG. This is because Silicon (Si) photodiodes, which are commonly used, have a sensitivity curve that exhibits a stronger response to shorter wavelengths, such as the pump beam. While Indium Gallium Arsenic (InGaAs)-based photodiodes can also be used, they are less robust than Si-based photodiodes.

The SRL/SRG signal is commonly detected by lock-in amplifiers, which is a device that employs phase-sensitive detection. This technique isolates the signal component at a reference frequency and phase while rejecting the noise signals at frequencies other than the reference. Thus, the noise signals do not affect the measurements, enabling measurements of weak signals.

The lock-in amplifiers require modulation of the signal to perform phase-sensitive detection. Modulations higher than 1 MHz are preferable due to the availability of Radio-Frequency (RF) filters and photodiodes [78]. For video-rate imaging, modulation at around 20 MHz is required to provide enough modulation cycles per pixel for a good-quality SRS image [78]. Devices such as Electro-Optic Modulator (EOM) or an Acoustic-Optic Modulator (AOM) are commonly used to obtain modulation.

Figure 4.3a illustrates the detection system based on SRL, where the Stokes beam is typically modulated at >1 MHz. This results in the amplitude modulation of the pump beam and the detection of the SRL. In contrast, the SRG is measured when the pump beam is modulated at a frequency of >1 MHz, and the modulation transfer to the Stokes beam is detected, as illustrated in Figure 4.3b.

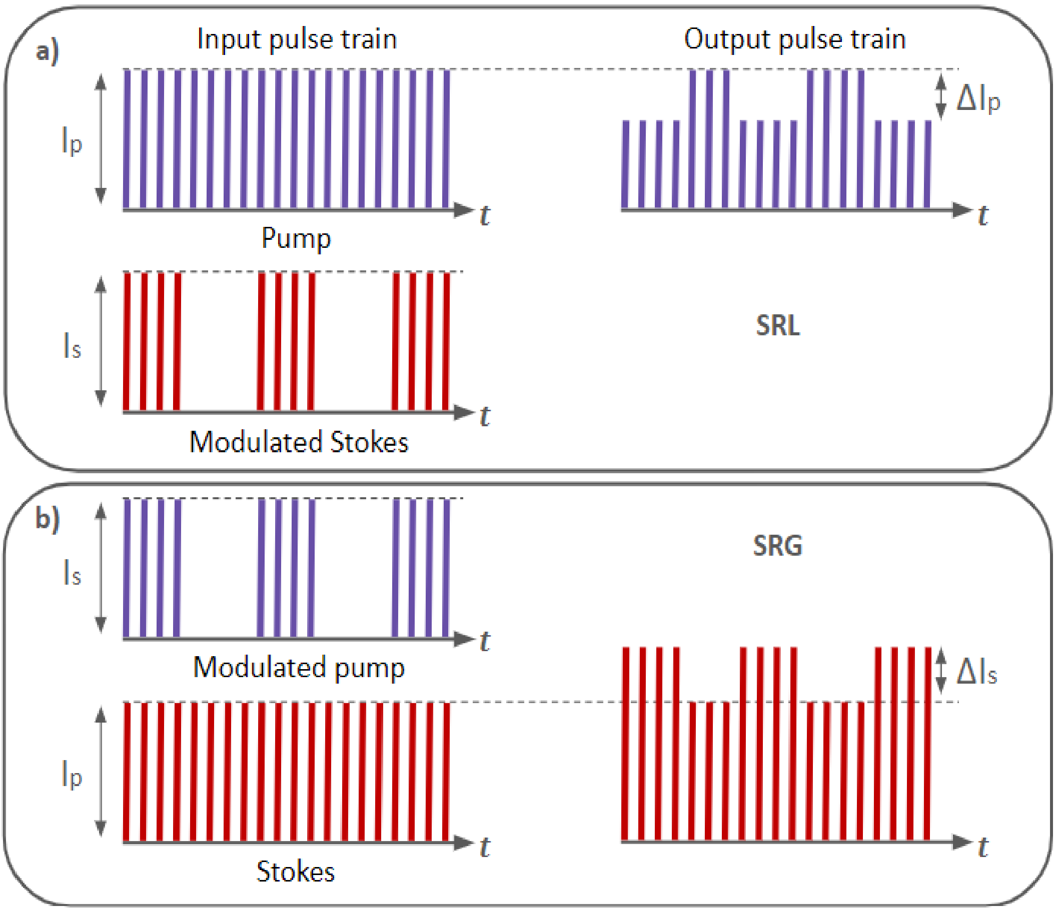

Figure 4.3: Detection system for SRS based on a) SRL and b) SRG.

4.3 Coherent anti-Stokes Raman scattering

Coherent anti-Stokes Raman scattering (CARS) was first observed in 1965 by R. Maker and P. Terhune [86], and later was named by R. Begley in 1974 [87]. Whereas CARS microscopy was first reported in 1982 by M. Duncan et al. [88]. Duncan's system presented a high non-resonant background signal due to the use of pulsed dye lasers. Since then, scientific advancements improved CARS microscopy, which now plays a crucial role in chemical analyses.

Figure 4.4 illustrates the scheme energy level of the CARS process. The vibrational coherence occurs by the interaction between the probe beam at a frequency ω_{pr} (*pr: probe*), which generates coherent radiation at the anti-Stokes frequency:

$$\omega_{aS} = \omega_{pr} + \omega_p - \omega_S, \tag{4.3}$$

where *aS: anti-Stokes*. If the $\omega_{pr} = \omega_p$, then the Equation 4.3 becomes:

$$\omega_{aS} = 2\omega_p - \omega_S. \tag{4.4}$$

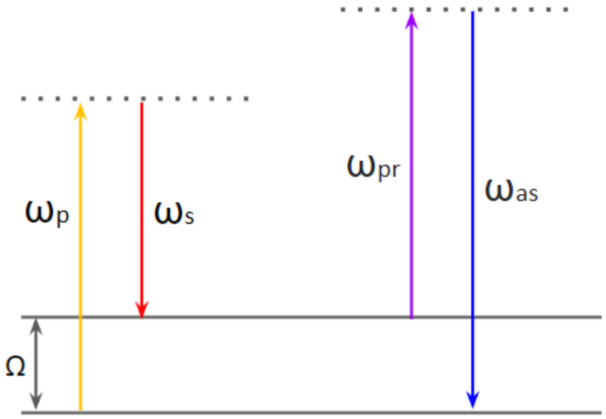

Figure 4.4: Schematic of energy levels of CARS process.

CARS is a technique that involves an FWM process, and to occur, the phase-matching condition needs to be satisfied:

$$|\Delta\beta| \cdot L = |\beta_{aS} - (2\beta_p - \beta_S)| \cdot L < \pi, \tag{4.5}$$

the wave vectors are denoted by: pump β_p, Stokes β_S, and anti-Stokes (aS) β_{aS}, where L is the length of the sample. Figure 4.5 illustrates the phase-matching diagram. The CARS signal is usually generated in a specific direction, where constructive interference of the anti-Stokes field occurs.

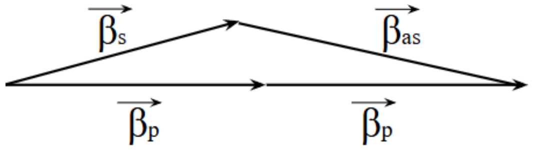

Figure 4.5: Phase-matching condition.

The transmitted intensity of CARS is described by the following equation:

$$\Delta I_{\text{CARS}} \propto N^2 \cdot \sigma^2_{\text{Raman}} \cdot I^2_p \cdot I_S. \tag{4.6}$$

Different from Equations 4.1 and 4.2, where the signal is proportional to the concentration, in CARS, the signal depends quadratically on the concentration. This dependence results in low sensitivity to the components with low concentrations and may become challenging at higher concentrations due to the fast signal growth.

CARS, like SRS, often use pulsed lasers with a temporal duration of a few picoseconds that provide peak power high enough to efficiently generate the signals, with narrow spectral bandwidth, less than 1 nm, to match the intrinsic linewidth of molecular vibrations [89].

4.3.1 CARS detection system

CARS technique is classified as homodyne and heterodyne detection. The homodyne detection is the conventional CARS, where the signal is detected at the anti-Stokes frequency, where the field mode differs from the input fields. Meanwhile, heterodyne detection is based on the interference between the CARS signal and a reference field at the same frequency. The signal is measured by mutual interference [78].

After the pump and Stokes beams are spatially and temporally overlapped, they are scanned through the sample. The intensity of the anti-Stokes wavelength is collected from the sample, and the pump wavelength is then separated from the anti-Stokes wavelength using a dichroic mirror. The intensity is measured using a Photomultiplier Tube (PMT), which are usually based on multi-alkali or GaAs because the detected anti-Stokes wavelengths range from 600 nm to 800 nm or higher. The NIR wavelength range has been presented to minimize the generation of non-resonant background [90].

However, the PMT efficiency is $< 25\%$ and lower than $<10\%$ for wavelengths longer than 800 nm [78]. Additionally, PMTs enable single wavelength measurements, so alternative approaches are necessary to detect the entire spectrum. Broadband spectral acquisition is commonly used. The anti-Stokes signal is collected by a spectrometer coupled with a high-sensitivity detector, such as a CCD camera. The spectrometer then resolves the different vibrational frequencies within the broadband signal, enabling the entire vibrational spectrum to be recorded in a single measurement [75].

4.4 Different types of CRS techniques

This section provides an overview of different approaches for CRS microscopy. They can be used for both SRS and CARS techniques; however, they require different detection systems, as described in Sections 4.2.1 and 4.3.1.

- **Wavelength tuning** is a typical approach used in SRS/CARS microscopy. By varying the wavelength of the pump and/or Stokes beam, it is possible to tune the system to match the vibrational frequencies at specific molecular bonds [10–14]. This solution requires tunable light sources that provide a narrow spectral bandwidth. This approach will be used in the thesis focused on development of light sources for CRS imaging.

- **Wavelength multiplexing** requires a broadband Stokes beam, typically achieved through spectral broadening by employing a PCF [91–94] and narrowband pump beam of a bandwidth typically less than 10 cm^{-1}.

  Figure 4.6 illustrates the principles of multiplex CARS and SRS [75]. Panel (a) shows the CARS process, where a narrowband pump beam (ω_{pu}) and a broadband Stokes beam (ω_S) interact with the sample, exciting multiple vibrational levels ($\Omega_1, \Omega_2, \Omega_3$). The vibrational coherence is read out by the pump beam ($\omega_{pr} = \omega_{pu}$), which generates a blue-shifted anti-Stokes signal (ω_{aS}). In SRS, instead the SRG mechanism, depicted in panel (b), illustrates the amplification of the Stokes signal at frequencies corresponding to the vibrational levels of the sample. Panel (c) presents the SRL mechanism, where a broadband pump and a narrowband Stokes beam interact with the sample, leading to an energy loss in the pump at frequencies matching the vibrational levels of the sample. The corresponding spectral diagrams are presented in panels (d) and (e).

  The CARS/SRS spectrum can be recorded in the frequency domain using multichannel detectors or in the time domain through the Fourier Transform (FT) method [95,96]. Although multiplex CRS does not provide faster imaging compared to single-frequency SRS/CARS, they provide more information as an entire spectrum can be registered, thus enabling imaging of multiple components [91,97,98].

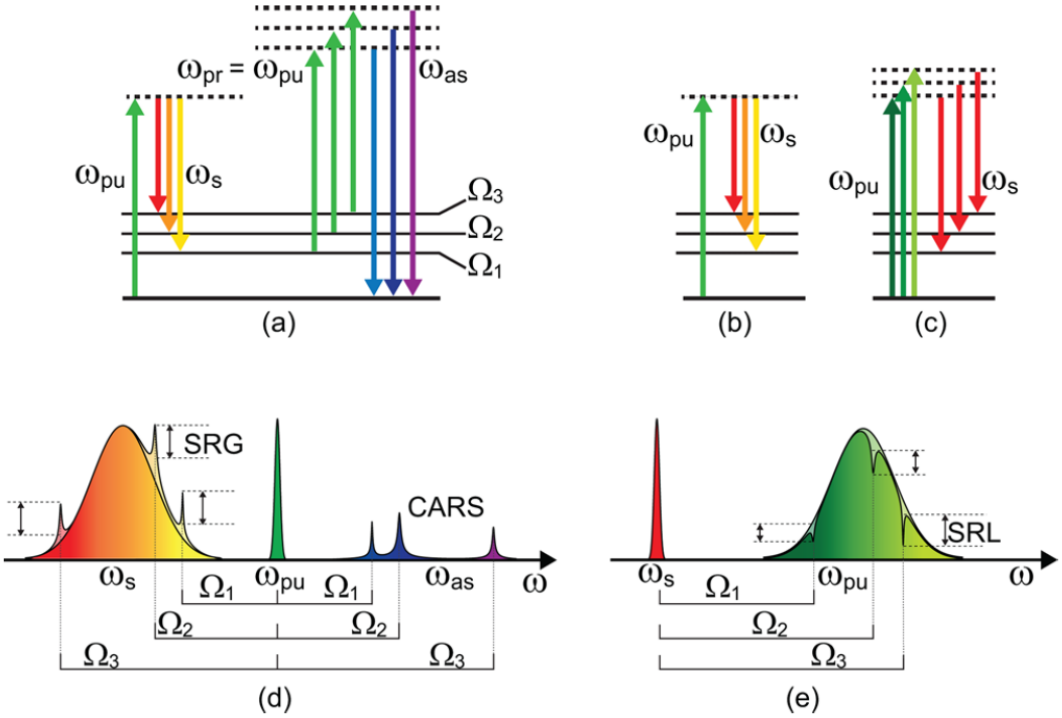

Figure 4.6: Schematic of energy levels and fields. a) Broadband CARS, b) SRS with broadband Stokes, c) SRS with broadband pump. Pump/Stokes spectra and nonlinear signals for the cases of d) broadband Stokes and e) broadband pump. Reprinted from [75].

- **Spectral Focusing (SF)** is commonly employed for fast tuning in CRS microscopy. This approach requires a broadband chirped femtosecond pump and Stokes beams. SF relies on focusing the entire spectral bandwidth of the chirped pulse into a single vibrational transition, resulting in an effective spectral bandwidth that is narrower than the original pulse bandwidth. To achieve chirp, pulse stretchers consisting of a double-pass grating lens combination allow fine-tuning of the chirp parameters [99]. Alternatively, blocks of highly dispersive glass (like SF57 or SF6) can be employed for pulse stretching [100–102].

  For a better understating, Figure 4.7 illustrates the concept of SF [75]. Panel (a) presents the chirped pump pulse (green) and a chirped Stokes pulse (red) overlapped in time. The frequency difference between the two pulses (Ω_1, Ω_2) changes linearly with the time delay (Δt). Panel (b) illustrates the frequency domain, where the frequency difference $\Omega(\Delta t) = \omega_{pu} - \omega_S + 2\alpha\Delta t$ determines which vibrational modes (Ω_1 or Ω_2), are excited, based on the Δt.

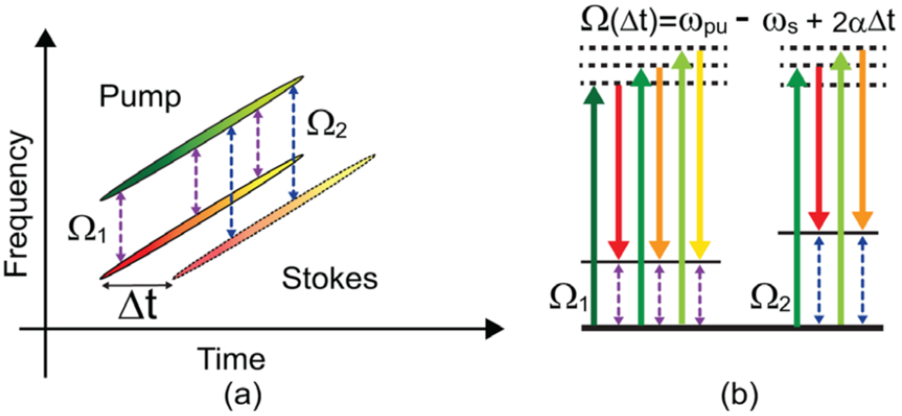

Figure 4.7: Concept of SF. a) The time-dependent frequencies of pump and Stokes pulses and b) the level excitation scheme. Reprinted from [75].

- **Deep learning** based CRS utilizes advanced algorithms to enable faster image reconstruction compared to traditional methods. It relies on the initial training of a neural network, which can subsequently perform real-time phase recovery, making it highly efficient for practical applications. Analyzing patterns in large data with deep learning algorithms can improve quality imaging by removing artifacts and noises [103]. It can also be used to reconstruct low-quality images in higher-resolution formats [104].

SRS/CARS microscopy is a vast field, and just a few techniques were presented here. Each method provides advantages for specific experimental requirements, such as imaging speed, depth of tissue penetration, simple systems, chemical specificity, and complex samples. Choosing the most suitable approach can optimize the experimental setup and achieve reliable results.

4.5 SRS vs CARS

This section summarizes and highlights the principal differences between the SRS and CARS microscopy. Both CRS methods require the spatial and temporal overlap of the pump, and Stokes beams to generate the Raman signals. SRS and CARS microscopy are often used for label-free imaging providing insights into the chemical composition of biological specimens without damaging the sample.

In SRS microscopy, the signal is detected by a lock-in amplifier, which requires modulation, generating a weaker signal but providing a background-free signal. In contrast, CARS uses a PMT to detect the anti-Stokes signal, generating a stronger signal but suffers from non-resonant background noise and distorted vibrational lineshapes. This makes it less effective for imaging of weak transitions, such as fingerprint region (600-1800 cm^{-1}). Due to its strong signal generation and high sensitivity, CARS microscopy is often used for imaging in the C-H stretch region (2800-3100 cm^{-1}).

Table 4.2 provides a comparison between CARS and SRS, highlighting the advantages and disadvantages of each technique.

SRS	**CARS**
Energy transfer process	Parametric process
Signal increases linearly with both pump and Stokes power	Signal increases quadratically with pump beam and linearly with Stokes beam powers
Spectra similar to SpRS	Dispersive shape
Linear concentration dependence of the chemical being imaged	Quadratic concentration dependence of the chemical being imaged
Signal is the convolution of the object with a point-spread function	Coherent image artifacts
No non-resonant-background	Non-resonant background

Table 4.2: Differences between the SRS and CARS microscopy [75, 78].

Chapter 5

Tunable light source for Raman imaging in the fingerprint region

5.1 Introduction

Light sources for SRS imaging applications should provide a tunable dual-wavelength output with a spectral bandwidth of a few nanometers and power levels of up to 100 mW, as discussed in Ref. [105]. Most reported so far SRS light sources emit few picosecond pulses tunable around 1000 nm and 750 nm, thus enabling measurements in the C-H stretch region spanning from 2700 cm^{-1} to 3200 cm^{-1}. These spectral ranges are typically achieved using Erbium (Er)-doped fiber oscillators combined with Supercontinuum Generation (SCG) in highly nonlinear fibers and Second-Harmonic Generation (SHG) in nonlinear crystals [105, 106]. A recent study by C. Kong et al., [107] adopts a similar approach, but instead of relying on SCG to achieve 1 μm from a 1.5 μm pump, it exploits Cross-Phase Modulation (XPM) to self-synchronize two fiber oscillators: one based on Er-doped fiber and the other on Yb-doped fiber.

The aim of this chapter is to develop a fiber-based tunable SRS light source that allows for measurement in the fingerprint spectral region. The fingerprint region is interesting due to the presence of proteins and lipids that contain important information from a chemical viewpoint. To accomplish this, I will construct a fiber laser composed of the Stokes and pump arm delivering picosecond pulses tunable around 1030 nm and 920 nm, respectively. In short, I will use tunable narrow-band spectral filtering of SPM-induced broadband spectra further amplified in Yb-doped and Nd-doped fibers.

Section 5.2 will describe in detail the development of the SRS light source, including the Yb-doped fiber oscillator, the pump, and the Stokes arm, as well as their spectral and temporal characterization. Next, in Section 5.3, the novel all-fiber method of efficient SPM broadening will be presented, allowing the extension of the tunability range of the pump arm. The application of the tunable light source for SRS imaging of the polystyrene beads and leukemic cells will be discussed in Section 5.4. Finally, Chapter 5 will be concluded in Section 5.5.

5.2 Experimental setup

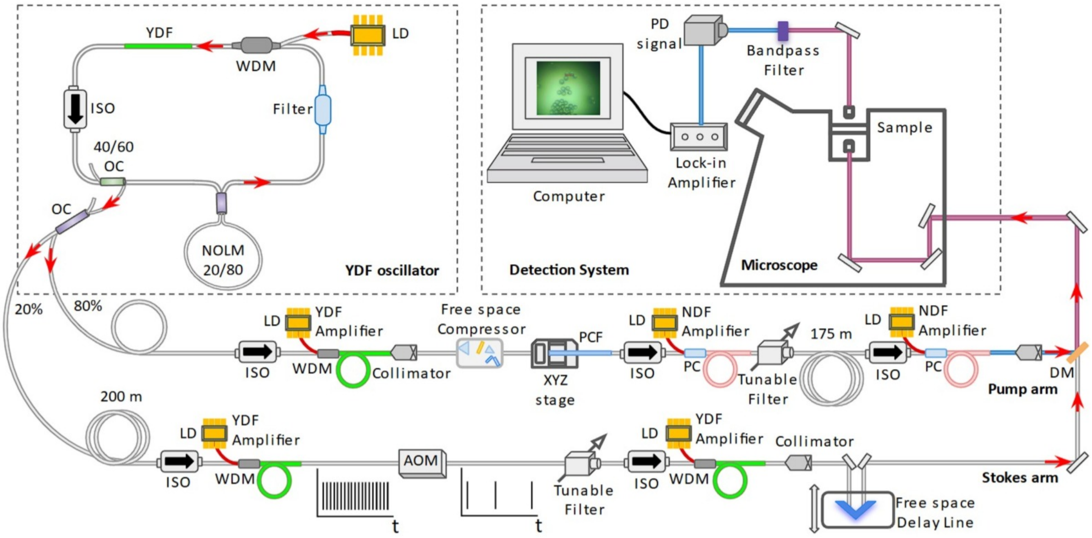

Figure 5.1: Experiment setup of the SRS-based imaging system composed of light source and microscope integrated with a detection system; YDF, Ytterbium-doped fiber; WDM, wavelength division multiplexer; LD, laser diode; ISO, optical isolator; NOLM, nonlinear optical loop mirror; OC, output coupler; PC, pump combiner; AOM, acousto-optic modulator; PCF, photonic crystal fiber; NDF, Neodymium-doped fiber; DM, dichroic mirror; PD, photodiode.

Figure 5.1 presents the schematic of the SRS imaging system, which includes a tunable fiber light source and a microscope integrated with a detection system. These components are described in detail in the following sections. The SRS light source consists of three main elements: the Yb-doped fiber oscillator, the Stokes arm, and the pump arm. The source was constructed entirely using polarization-maintaining (PM) fibers to ensure stable operation.

5.2.1 Mode-locked Yb-doped fiber oscillator

Figure 5.2 illustrates the schematic of the ultrafast fiber oscillator developed by following Ref. [31]. The gain medium consisted of a 0.5 m long Yb-doped fiber (Coherent, PM-YSF-HI), which was pumped through a wavelength division multiplexer (WDM) using a continuous-wave (CW) laser diode emitting at 976 nm. A fiber isolator (ISO) was implemented to ensure the unidirectional beam propagation in the cavity.

The oscillator was mode-locked by exploiting a 4.4 m long Nonlinear Optical Loop Mirror (NOLM) built from a 2x2 fiber coupler with a power splitting ratio of 20/80. To optimize the pulse duration while maintaining stable laser operation, a spectral filter with a Gaussian transmission profile and a Full Width at Half Maximum (FWHM) of 4.45 nm, centered at a wavelength of 1030 nm was employed. Moreover, a fiber coupler with a 40/60 splitting ratio was implemented to output 40% of the light from the cavity. It was placed before the NOLM to monitor the mode-locking operation via a beam reflected from the loop mirror. The total cavity length was around 10.5 m, which implies a repetition rate of 17.18 MHz.

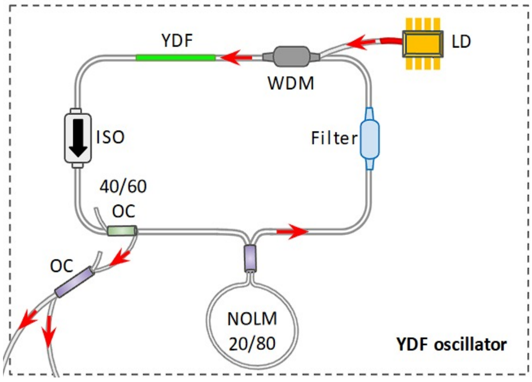

Figure 5.2: Schematic of the Yb-doped fiber oscillator.

The spectral and temporal characteristics of the light emitted by the Yb-doped fiber oscillator are reported in Figure 5.3. They were measured by using the following instruments: the Optical Spectrum Analyzer (OSA, Yokogawa AQ6374), a Radio-Frequency Spectrum Analyzer (RF, Agilent E4443A), an ultra-fast photodetector (Alphalas, InGaAs, UPD-35-UVIR-P) connected to a 6 GHz oscilloscope (WavePro 760Zi-A, Teledyne Lecroy), a homemade built autocorrelator, and a power meter.

The oscillator generates chirped pulses with a duration of 9.5 ps (see Figure 5.3b) at a repetition rate of 17.18 MHz (see Figure 5.3c), which can be compressed using a free-space grating compressor to 193 fs, as it will be discussed further in the chapter. The pulses are centered at 1030 nm and exhibit a typical cat-ear spectrum characteristic of the dissipative soliton regime, with a bandwidth of 14 nm, as shown in panel (a) of Figure 5.3. Additionally, the laser is self-starting and demonstrates highly stable mode-locking operation, as evidenced by the pulse train in panel (d) of Figure 5.3 and the 90 dB signal-to-noise ratio in the RF spectrum shown in panel (c) of Figure 5.3. These results are achieved when the laser diode current is set to 364 mA, delivering an average output power of 10 mW from the oscillator.

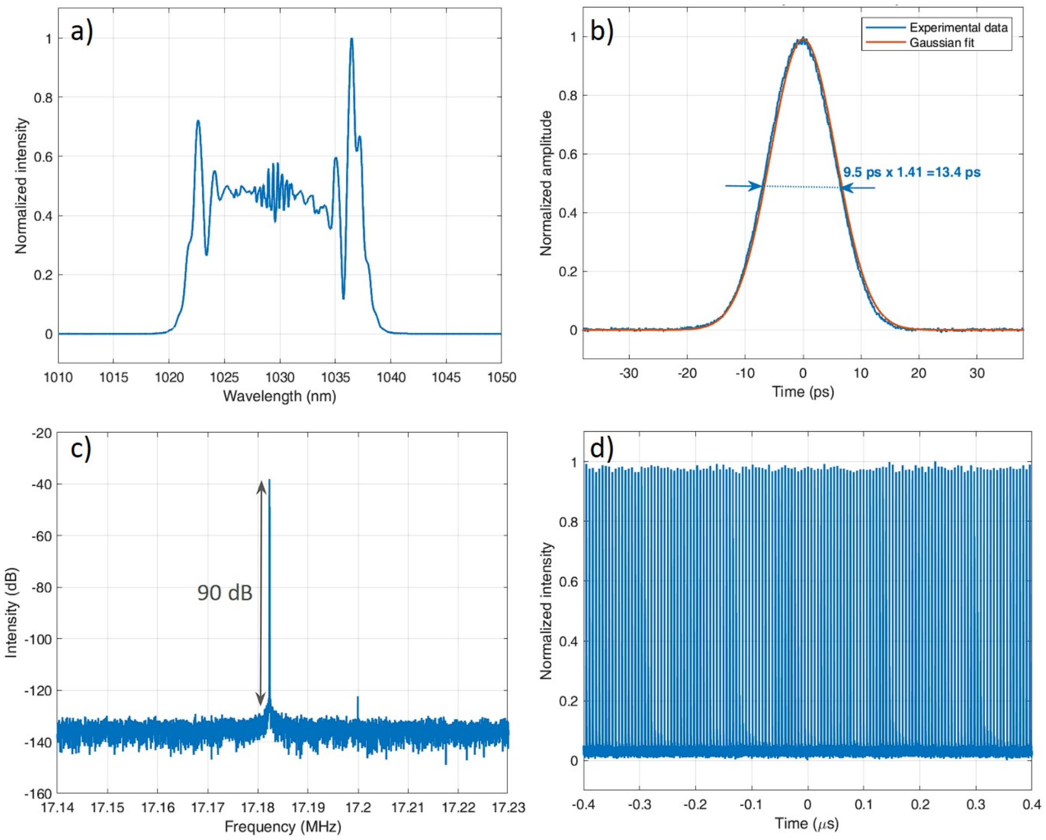

Figure 5.3: a) Output spectrum centered at 1030 nm with an FWHM of 14 nm and b) pulse profile with a temporal duration of 9.5 ps. c) Radio-frequency (RF) spectrum of the generated output pulse train centered at 17.18 MHz and d) output pulse train, fluctuations are caused by the undersampling of the oscilloscope.

5.2.2 Stokes arm of tunable light source

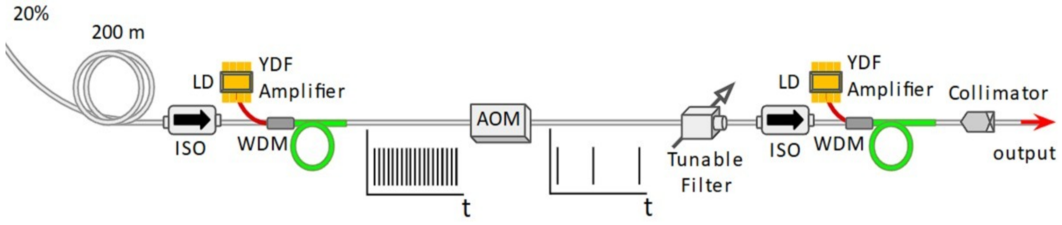

Figure 5.4: Schematic of the Stokes arm of the SRS light source.

The output beam of the previously described Yb-doped fiber oscillator was next split into two beams using a 2x2 fiber output coupler with a power splitting ratio of 20/80. A 20% output beam was used to construct the Stokes arm of the SRS light source, as schematically depicted in Figure 5.4.

Specifically, the beam was first pre-amplified in the initial stage of a Yb-doped fiber amplifier. Its repetition rate was then reduced from 17.18 MHz to 1 MHz using a fiber-based Acousto-Optic Modulator (AOM, AA Optoelectronic) to enable lock-in detection required for further SRS imaging applications (see Chapter 4, Section 4.2.1). Subsequently, the beam was spectrally filtered through a tunable filter with a 1 nm bandwidth (Agiltron, FOTF-010223131) and finally amplified in the second stage of the Yb-doped fiber amplifier.

All the Yb-doped fiber amplifiers were custom-built, utilizing Yb-doped fibers (Coherent, PM-YSF-HI) as the gain medium, with a length of approximately 0.6 m. Then, the Yb-doped fiber is pumped by a WDM using a CW laser diode emitting at 976 nm. An ISO is also included to prevent back reflections.

As a result, a Stokes beam tunable from 1023 nm to 1036 nm was achieved, covering the entire spectral range of the initial fiber oscillator. The beam had a spectral bandwidth of 2.0 nm and an average power of up to 100 mW at each wavelength, as shown in panel (a) of Figure 5.5. The pulse duration was measured to be approximately 12.2 ps (see Figure 5.5b), which resulted from adding a 200 m long segment of fiber (Coherent, PM980-XP) before the first amplifier. This modification was made to minimize undesired spectral broadening.

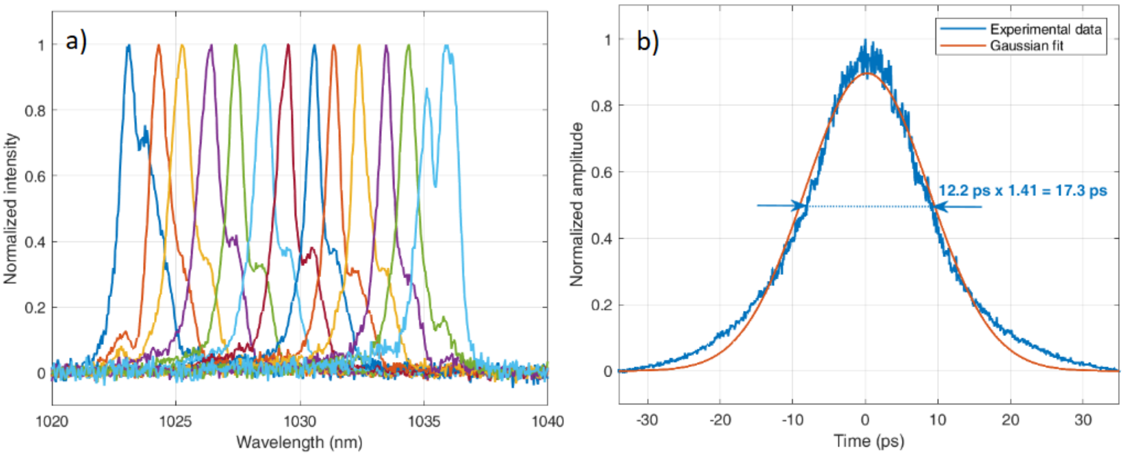

Figure 5.5: a) Tunable Stokes spectra with an average power of 100 mW for each spectrum. b) Pulse profile with temporal duration of 12.2 ps measured for a selected Stokes beam at 1030 nm.

5.2.3 Pump arm of tunable light source

The 80% of the output beam emitted by the Yb-doped oscillator was directed to construct the pump arm of the SRS light source, as schematically shown in Figure 5.6. While the Stokes arm is tunable around a central wavelength of 1030 nm, tunability around 920 nm is required to access the fingerprint spectral region for further use in SRS imaging. To achieve this spectral range, it was utilized

Supercontinuum Generation (SCG), a process known to require femtosecond pulses for efficient operation.

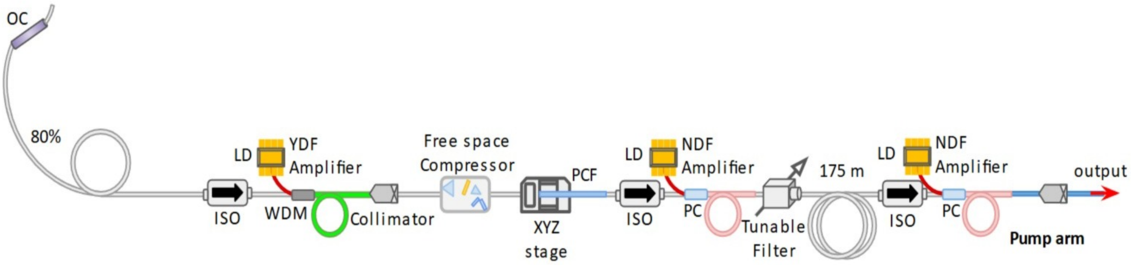

Figure 5.6: Schematic of the pump arm of the SRS light source.

As mentioned earlier, the ultrafast fiber oscillator delivers chirped pulses that can be compressed to 193 fs. The oscillator's average power was increased to 400 mW using a Yb-doped fiber amplifier to construct the pump arm, similar to those used in the Stokes arm. The pulses were then compressed using a free-space grating compressor. The characteristics of the compressed pulses were measured using a custom-built SPIDER device, employing the Spectral Phase Interferometry for Direct Electric-field Reconstruction technique, as illustrated in Figure 5.7.

Optical spectrum (black) and phase (red dashed), as well as reconstructed temporal electric field intensity (red) compared to Fourier Transform-Limited (FTL) pulse (blue), are shown in panels (a) and (b) of Figures 5.7, respectively.

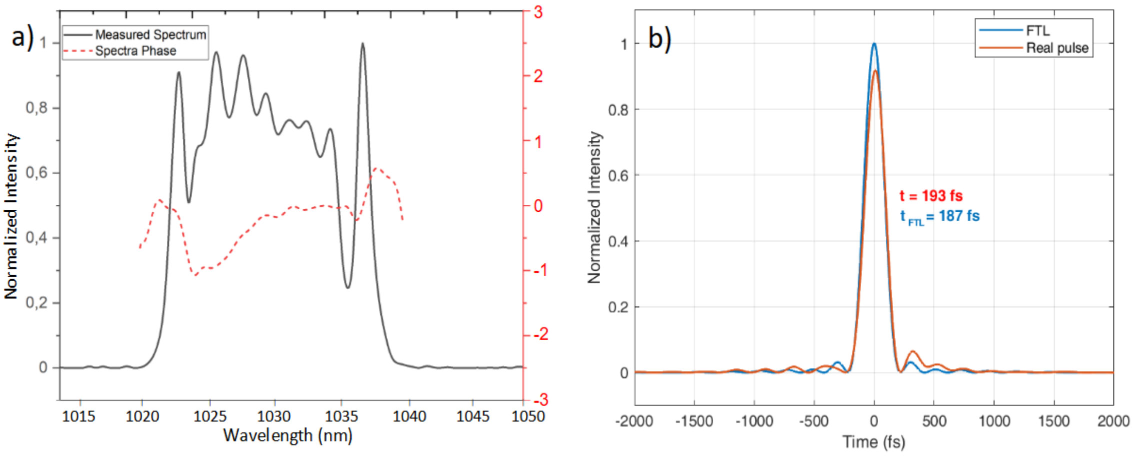

Figure 5.7: a) Optical spectrum and spectral phase with a temporal Strehl ratio of 0.92. b) Reconstructed temporal electrical field intensity of the output pulse (red curve) in comparison with the FTL pulse (blue curve).

Next, the 193 fs pulses were introduced to 5 cm long all-normal dispersion PCF with 88% coupling efficiency. Specifically, a NL-1050-NEG-1-PM fiber (from NKT Photonics) was used, with a core diameter of 2.3 μm and structure and dispersion profile described in Section 2.3.4 of Chapter 2. It was placed the fiber on a precise 3-axes translation stage followed by a set of mirrors and a properly chosen aspheric lens (in this case, with a 6.24 mm focal length) to maximize the coupling efficiency. Moreover, a half-wave plate was employed to align the linear polarization of the input beam according to one of the neutral axes of the PM PCF.

Figure 5.8 presents a progressive spectral broadening as a function of input average power. At the maximum input average power of 310 mW, the supercontinuum spans from 700 nm to 1200 nm. The SC is primarily induced by the SPM process, a typical feature of a normal dispersion regime. However, we can also observe the appearance of a separated peak at 700 nm as a result of a Cross-Phase Modulational instability (XPMI) according to Ref. [9, 108].

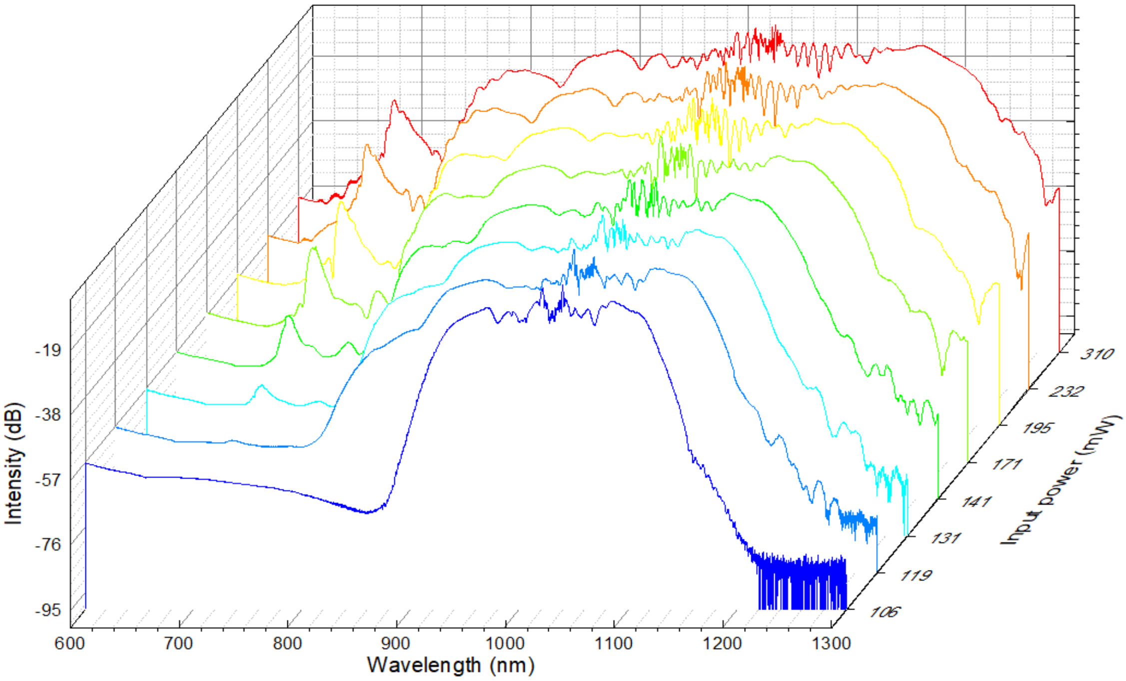

Figure 5.8: Spectral evolution as a function of the input average power.

The SC was subsequently used as a seed for the Nd-doped fiber amplifier, which simultaneously amplified and filtered the injected broadband spectrum to the region around 920 nm. The SC was introduced into the amplifier by splicing the end of the PCF to the PM780 fiber pigtail (from Coherent) connected to the amplifier input. This process resulted in a 38% loss, primarily due to the different properties of the two spliced fibers. The Nd-doped fiber amplifier was composed of 7 meters of a double-cladding (DC) Nd-doped fiber (Exail, IXF-2CF-NDPM-5-80-W*), which was pumped through a beam combiner (Exail, IXS-COMB-PM-1-1-1-4-80-P) by a 40 W laser diode at a central wavelength of 808 nm (BWT, BLDDG00665). A water cooling system was used to cool the system.

Figure 5.9 presents the SC spectra measured at the output of the Nd-doped fiber amplifier as a function of output amplified power. The amplification process yielded a maximum output power of 61.2 mW within the spectral region around 920 nm. Next, a fiber-tunable spectral filter with 1 nm of bandwidth (Brimrose, TEAF-900-1100- UH-EH-2FP-PM) was employed. Because of approximately 64% of losses provided by the filter, a second Nd-doped fiber amplifier was implemented, using 4.5 m of the DC Nd-doped fiber, which permitted to increase the power up to 50 mW.

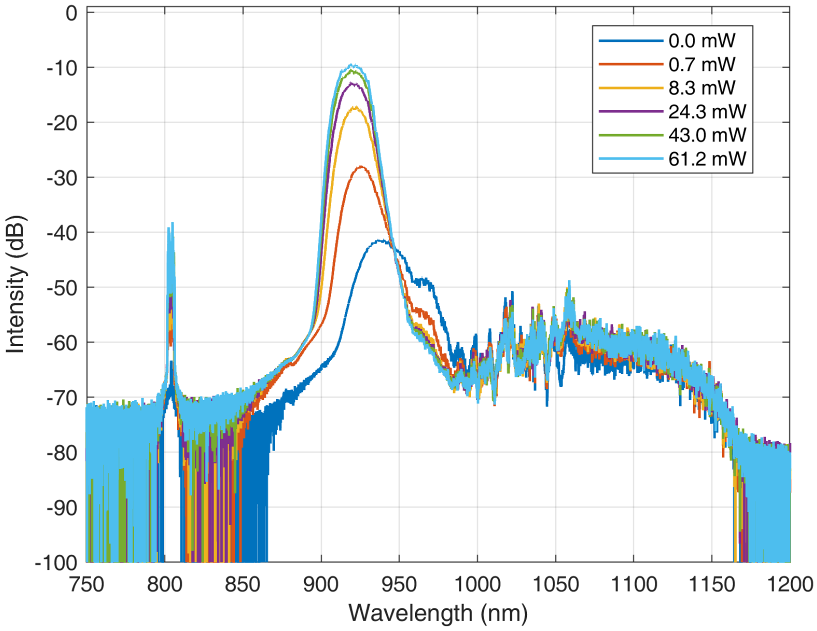

Figure 5.9: Spectra at the output of Nd amplifier as a function of amplified output power. The peak at 808 nm corresponds to the residual pump.

To keep the spectral bandwidth close to a few nm, 175 m of PM780 fiber (from Coherent) was added between the two Nd amplifiers at the lowest power point, minimizing unwanted nonlinear effects. This additional fiber increased the pulse duration to 14.4 ps, as shown in panel (b) of Figure 5.10. The reduced peak power helped prevent spectral broadening of the output beam. Consequently, the pump arm delivered spectra with a power of 50 mW and a 2 nm bandwidth, tunable from 913 nm to 930 nm, as illustrated in panel (a) of Figure 5.10.

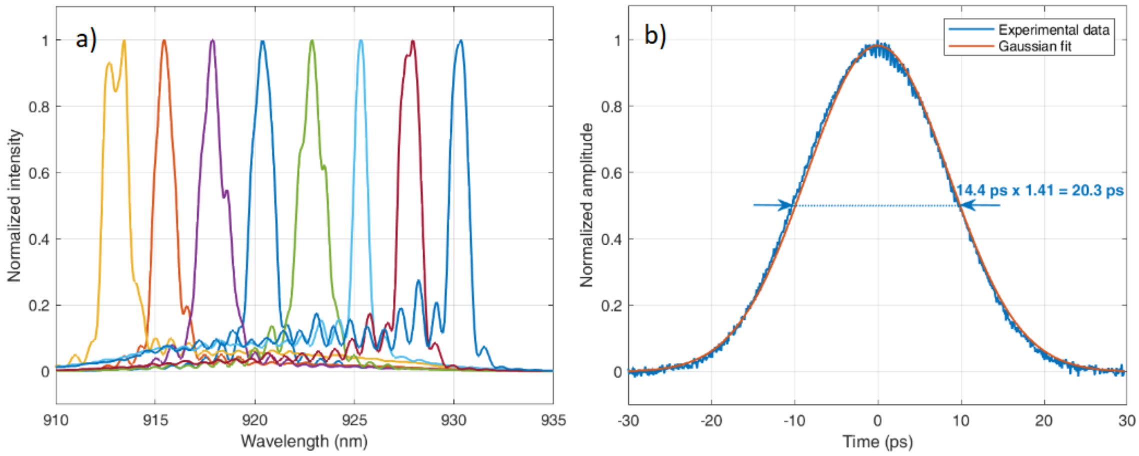

Figure 5.10: a) Tunable pump spectra with an average power of 50 mW for each spectrum. b) Pulse profile with a temporal duration of 14.4 ps measured for a selected pump beam at 920 nm.

5.3 Optimization of the light source

The previously described version of the tunable SRS light source allowed measurements in the fingerprint Raman region from 977 cm^{-1} up to 1300 cm^{-1}. To further extend the range of wavenumbers accessible with the light source, I developed a second version of the SRS laser system. This upgraded system expanded the tunability range of the Stokes arm through the implementation of an innovative method for efficient spectral broadening of chirped pulses via Self-Phase Modulation (SPM) in an all-fiber configuration.

Nonlinear spectral broadening can be utilized to extend the tunability of the Stokes beam beyond the spectrum of the light directly emitted by the Yb-doped fiber oscillator. Typically, generating a broad spectrum requires femtosecond pulses. Therefore, a free-space grating compressor must be employed for the Yb-doped fiber oscillator, which produces chirped pulses with durations of several picoseconds. This approach was previously used in constructing the SRS light source pump arm, as described in Section 5.2.3.

However, free-space configurations are not environmentally stable and often require frequent adjustments. In contrast, all-fiber systems, particularly those constructed entirely from polarization-maintaining (PM) fibers, are known for their robustness against mechanical and environmental fluctuations.

In this work, a novel method for efficient SPM-induced spectral broadening of chirped pulses was developed. The experimental setup is schematically illustrated in Figure 5.11. Specifically, 20% of the output power from the Yb-doped fiber oscillator was pre-amplified before passing through a super-Gaussian fiber-based filter with a

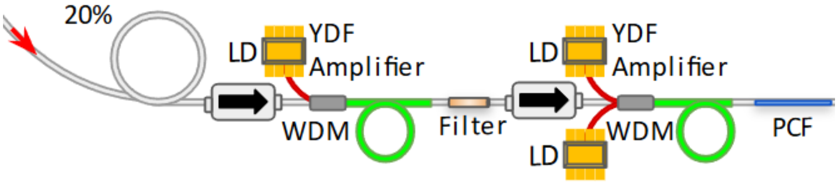

Figure 5.11: Schematic of the spectrum broadening.

2 nm bandwidth centered at 1030 nm (Lightcomm, PMFWDM-T1030). This filter reduces the spectral bandwidth of the input beam, enabling the compression of 9.5 ps chirped pulses to below 1 ps, which is sufficiently short for efficient SPM in PCF. As presented in Figure 5.11, the compressed pulses were first amplified in a Yb-doped fiber amplifier and then injected into a 1 m segment of LMA-PM-5 fiber (NKT Photonics).

Figure 5.12 illustrates the resulting SPM as a function of power. As shown, the LMA-PM-5 fiber achieved maximum spectral broadening, spanning from 995 nm to 1080 nm, at a power of 300 mW. To the best of our knowledge, this represents the broadest SPM achieved in an all-fiber configuration.

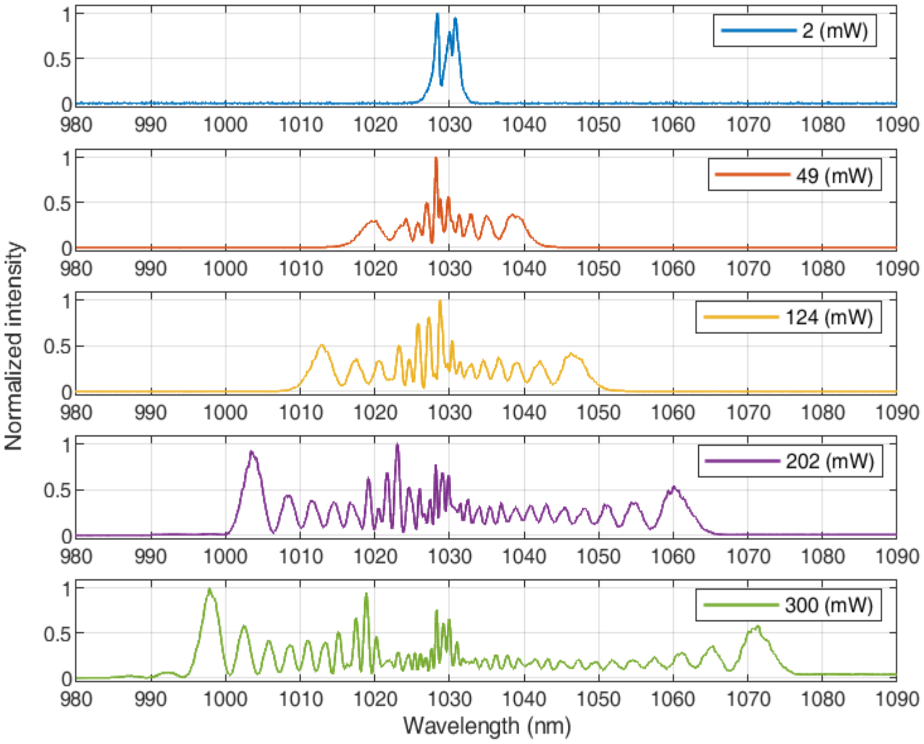

Figure 5.12: SPM evolution as a function of the pump power.

A tunable fiberized filter was again employed, followed by a multistage amplification system, schematically illustrated in Figure 5.13 to further develop the Stokes arm of the SRS light source with broader wavelength tunability.

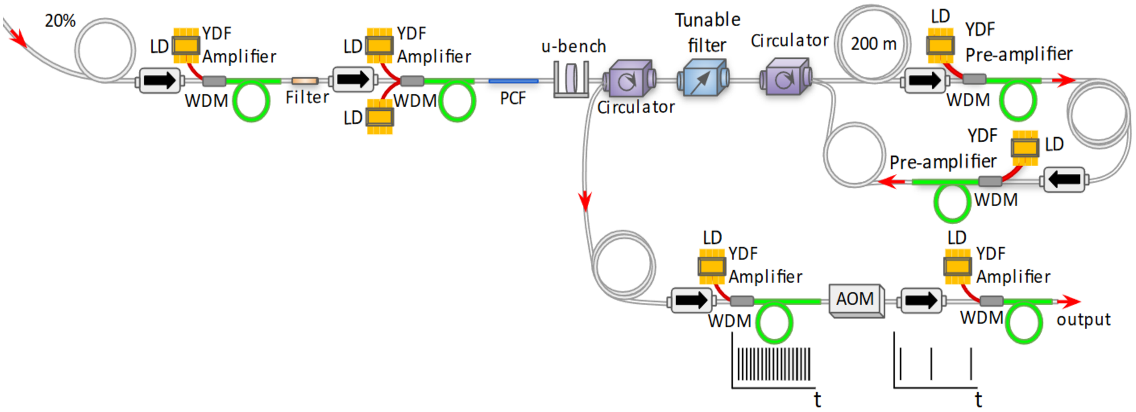

Figure 5.13: Schematic of the improved Stokes arm.

In detail, a 1 nm tunable filter (Brimrose, TEAF-900-1100-UH-EH-2FP-PM) was employed, capable of handling a maximum input power of 80 mW. To ensure the filter's safety and to prevent unwanted wave-breaking nonlinear effects, a density filter placed in a fiberized U-bench was used to reduce the input power from 300 mW to 60 mW. Figure 5.14 shows the spectra with 1 nm bandwidth and tunable from 1000 nm to 1070 nm, which were measured at the output of the Brimrose filter.

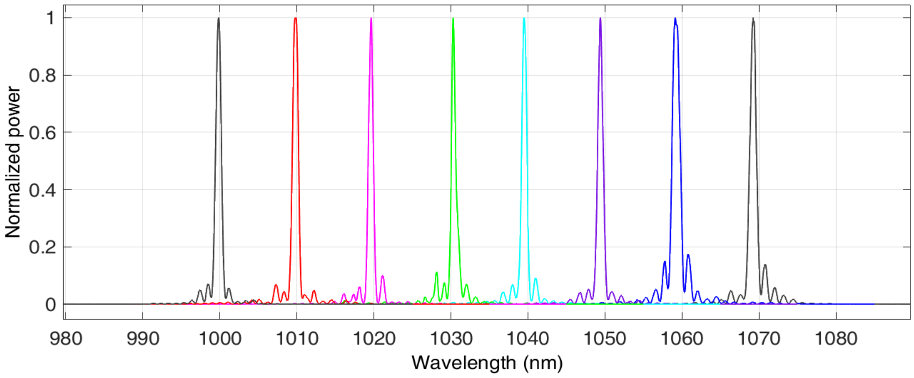

Figure 5.14: Spectra measured at the output of the 1 nm bandpass filter at different tuned central wavelengths.

This tunable beam had relatively low power, well below 1 mW. Ytterbium-doped fibers exhibit a maximum gain of around 1030 nm. When attempting to amplify this beam with varying central wavelengths using Yb-doped fibers, significant Amplified Spontaneous Emission (ASE) noise was generated, especially for seed wavelengths near the edges of the gain spectrum. This issue made amplification less efficient.

To address this challenge, a multistage Yb amplifier with double-pass spectral filtration was developed, as shown in Figure 5.13. This approach significantly reduced ASE noise. As a result, a beam with a 1.4 nm spectral width, tunable from 1020 nm to 1070 nm was achieved, as presented in Figure 5.15a, with an improvement of over 2 times compared to the initial prototype. This improvement extended the range of Raman shifts covered by the light source, which now ranges from 950 cm^{-1} to 1600 cm^{-1} with 40 mW of average output power.

To minimize SPM effects, a 200 m-long PM980 fiber was retained, which, as before, elongated the pulse duration to 10.4 ps, as displayed in panel (b) of Figure 5.15. Additionally, the AOM was placed between the final two amplification stages.

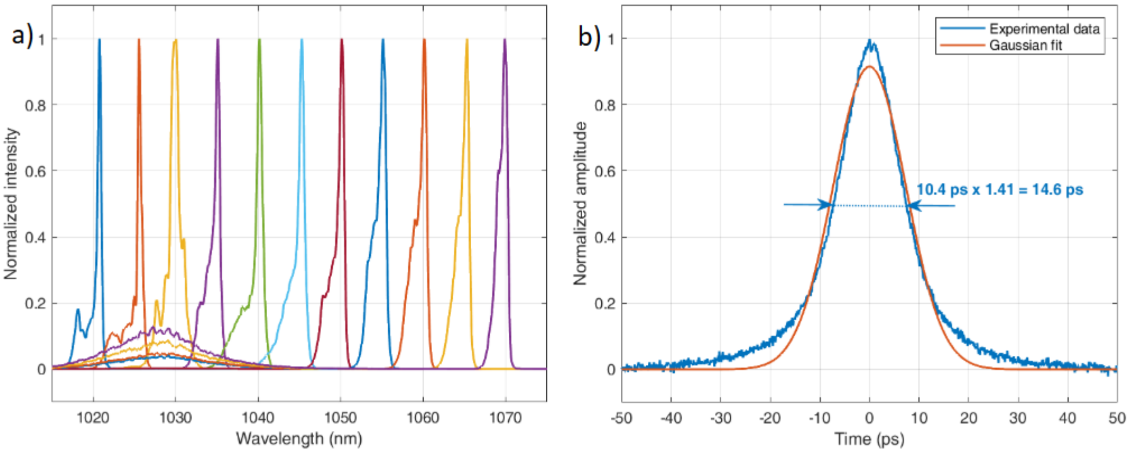

Figure 5.15: a) Output Stokes spectra tunable within extended spectral range. b) Pulse profile with the temporal duration of 10.4 ps measured for a selected improved Stokes beam at 1030 nm.

5.4 Application to SRS imaging

The tunable light source was implemented in an SRS microscope, schematically illustrated in Figure 5.16, to demonstrate its potential for imaging applications. The pump and Stokes beams were directed to the microscope through a series of optical mirrors and a dichroic filter to ensure spatial overlap. Temporal overlap was achieved with a delay line exploring Second-Harmonic Generation (SHG) in BBO crystal (see Appendix A).

The microscope was custom-built by the group photonic nanostructure facility, Institute of Experimental Physics, Faculty of Physics, University of Warsaw. It consisted of two objectives (Nikon, 20x, 0.75 NA): one to focus the beams on the sample and another to collect the signal. A galvo scanner (Cambridge Technology, 6215H) was included to enable x-y scanning and obtain images. Detection was

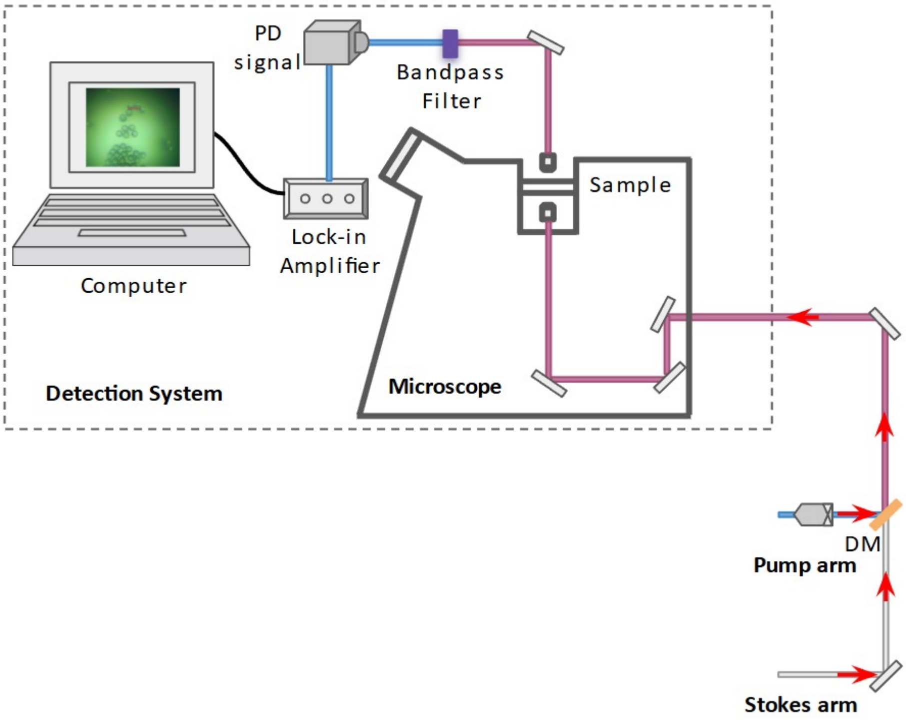

Figure 5.16: Detection system based on lock-in amplifier.

performed with a lock-in amplifier (Zurich Instruments, HF2LI) configured for Stimulated Raman Loss (SRL) measurements. To eliminate the residual 1030 nm beam, a short-pass 1000 nm spectral filter was placed before the photodiode (Thorlabs, DET10A(/M), Si Biased Detector).

To validate the system, SRS measurements were conducted on a well characterized sample of polystyrene beads, known for their quite strong and distinct Raman peak at 1000 cm^{-1} [109, 110]. The resulting SRS spectrum is shown as a dotted blue line in Figure 5.17, measured by tuning the pump and Stokes beams. We also included the corresponding Spontaneous Raman Scattering (SpRS) spectrum (red line) measured using a commercial Renishaw microscope with a 532 nm excitation laser for comparison. The latter measurement was conducted in collaboration with the group photonic nanostructure facility, Institute of Experimental Physics, Faculty of Physics, University of Warsaw.

The observed discrepancies can be attributed to residual ASE contributions in the spectra of both the Stokes and pump beams, particularly near the edges of their tunable spectral range. Nonetheless, both the SRS and SpRS spectra are in good agreement, showing consistency in the overall spectral shape and clearly exhibiting the characteristic Raman peak of polystyrene at 1000 cm^{-1}.

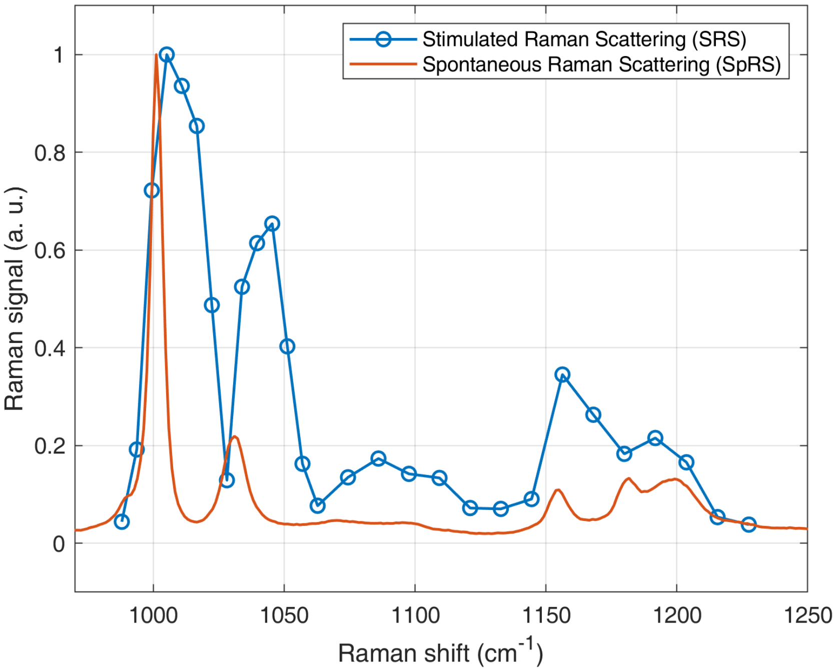

Figure 5.17: SRS spectrum of polystyrene beads (blue line-dot) compared with the SpRS spectrum (red line).

We also performed SRS imaging of the same sample of polystyrene beads. Panel (a) of Figure 5.18 shows the SRS image measured at 1000 cm^{-1}. This image of 100×65 pixels was registered with a pixel dwell time of 5 ms and spatial resolution of 1.2 μm. We used the pump and Stokes beam with average power of 45 mW and 30 mW, respectively. The corresponding optical image is displayed in panel (b) of Figure 5.18.

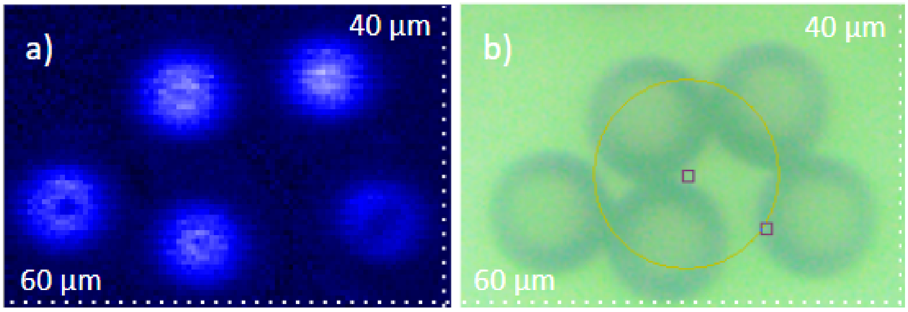

Figure 5.18: a) SRS image of polystyrene beads recorded at 1000 cm^{-1} with an acquisition time of 33 s and 1.2 μm spatial resolution. b) Corresponding optical image.

In the next step, we analyzed the leukemic cells (K562 line) provided by the group of prof. dr. Wojciech Młynarski from the Medical University of Łodz.

Firstly, the SpRS spectrum was measured at the University of Warsaw to identify the locations of Raman peaks. The obtained results are illustrated in Figure 5.19, showing the data previously retrieved from the commercial Renishaw microscope. The most prominent peak is observed at 3000 cm^{-1} as highlighted in pink, and it lies within the C-H stretch Raman region, typically characterized by a strong Raman signature. The fingerprint region is highlighted in orange, spanning from 600 cm^{-1} to 1800 cm^{-1}, while the red shading color marks the part covered by the SRS light source, ranging from 950 cm^{-1} up to 1600 cm^{-1}. The fingerprint region is important from the chemical analysis viewpoint as it provides information about various molecular bonds found in biological samples, such as proteins, lipids, and nucleic acids.

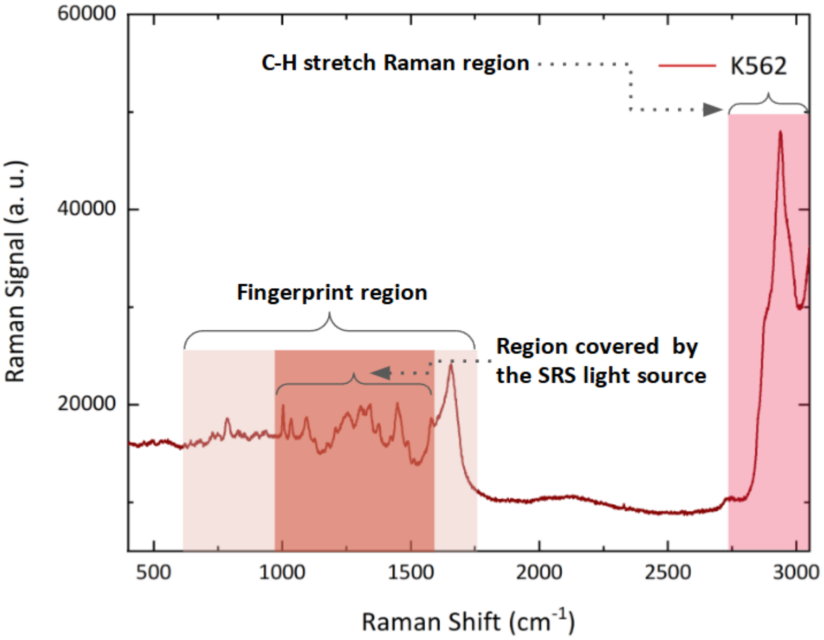

Figure 5.19: Spectrum of the SpRS of the leukemic cells sub-type K562 line.

Finally, we performed SRS imaging of these leukemic cells. Results obtained at 1300 cm^{-1} are illustrated in panel (a) of Figure 5.20. Panel (b) of Figure 5.20 illustrates the corresponding optical image. The SRS image of 50×50 pixels was achieved with a pixel dwell time of 50 ms and spatial resolution of 1.2 μm, using the pump and Stokes beam of 100 mW and 30 mW average power.

The imaging acquired at 1000 cm^{-1} is illustrated in panel (c) of Figure 5.20. It was registered with an acquisition time of 24 s, a dwell time of 30 ms, and a spatial resolution of 1.2 μm, with 26x30 pixels. The average power used for the pump and Stokes beams were 60 mW and 20 mW, respectively. Panel (d) of Figure 5.20 represents the corresponding optical images.

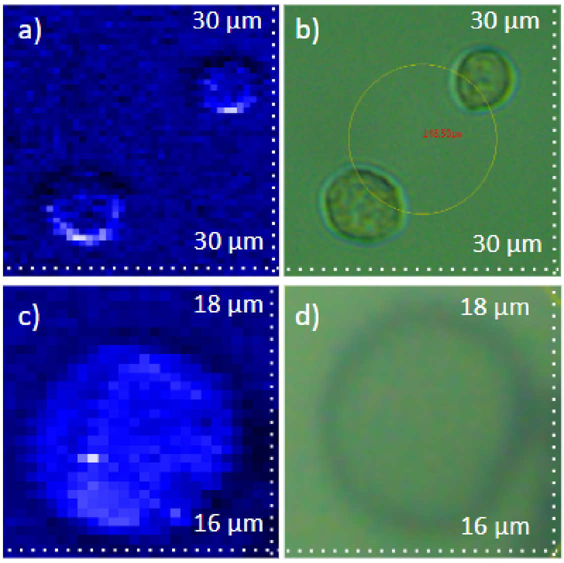

Figure 5.20: Imaging of leukemic cells subtype K562 line: SRS images performed at 1300 cm^{-1} (a) and 1000 cm^{-1} (c), and their corresponding optical images (b,d), respectively.

5.5 Conclusions

This chapter I presented the development of a dual-wavelength tunable light source designed for SRS imaging within the fingerprint spectral region. The source was based on a Yb-doped fiber oscillator mode-locked via a NOLM, delivering chirped pulses with a duration of 9.5 ps, a repetition rate of 17.18 MHz, and a fixed central wavelength of 1030 nm. This initial beam was split into two arms to construct the pump and Stokes beams.

The pump beam was tunable from 913 nm to 930 nm, achieved through tunable spectral filtering of SCG followed by multistage amplification in Nd-doped fiber. The broad SC was generated by an all-normal PCF, pumped with femtosecond pulses obtained by compressing the chirped pulses in a free-space grating compressor. The Stokes beam, tunable within the range of the oscillator's spectrum from 1023 nm to 1036 nm, underwent tunable spectral filtering and subsequent amplification in Yb-doped fiber.

The pump and Stokes beams had a bandwidth of 2 nm, a maximum output power of up to 100 mW, and a pulse duration of approximately 14.4 ps. This light source enabled SRS imaging within the fingerprint Raman region, covering a range from 977 cm^{-1} to 1300 cm^{-1}.

In the next step, the tunability range of the Stokes arm was extended by implementing a novel all-fiber approach to perform spectral broadening via SPM efficiently. Instead of using the free-space grating compressor to shorten the positively chirped pulses, a narrow-band fiberized spectral filter was used, which allowed to shorten 9.5 ps chirped pulses down to a subpicosecond regime. Such pulses were sufficiently short to induce SPM in LMA-PM-5 fiber spanning a broad 85 nm range in a normal dispersion regime. Importantly, this all-fiber configuration also helped to eliminate the need for recurrent re-alignment. After this improvement, the Stokes arm was tunable within the extended spectral range from 1020 nm up to 1070 nm, thus enabling SRS measurements in the fingerprint region extended from 950 cm^{-1} to 1600 cm^{-1} with 40 mW of average output power.

The tunable dual-wavelength light source was integrated into an SRS-based microscope system for imaging applications. SRS images were acquired for two types of samples: initially, well-characterized polystyrene beads were measured at 1000 cm^{-1} to validate the system, followed by SRS imaging of leukemic cells at both 1000 cm^{-1} and 1300 cm^{-1}. To the best of our knowledge, this represents the first demonstration of SRS imaging of carcinogenic cells within the fingerprint Raman region.

Chapter 6

Widely tunable all-Fiber Optical Parametric Oscillator seeded by ultrashort pulses at a fixed wavelength

6.1 Introduction

This chapter aims to significantly extend the tunability range of the light source and, thus, to build an all-fiber light source, allowing for Raman measurements in both fingerprint and C-H stretch regions. I will then use the Degenerate-Four-Wave Mixing (D-FWM) in Photonic Crystal Fiber (PCF), the nonlinear effect able to provide such a broad spectral tunability. When placed in cavity configuration, the efficiency of D-FWM generation and its spectral selectivity can be significantly improved.

Indeed, Fiber Optical Parametric Oscillators (FOPOs) have been demonstrated as a way to increase the power of generated FWM sidebands, by making them circulate in the cavity while being self-synchronized with the pump. During each circulation in the cavity, the FWM waves experience continuous amplification and energy exchange due to the nonlinear parametric gain of the PCF.

The Fiber-Optical Parametric Amplifiers (FOPAs) [111] additionally enable significant power enhancement within a broad tunable spectral range. However, in contrast to FOPOs, the FOPA systems typically provide lower spectral selectivity due to the broad amplification bandwidth, a feature that is crucial for Raman characterization of molecular structures and chemical compounds.

FWM-based FOPOs reported to date typically use Yb-doped fiber oscillators as the pump source. Lamb's work [11] reports the FOPO incorporating free-space parts and using the pump beam with tunability limited to approximately 10 nm, thus restricting the Raman measurements only to the C-H stretch region.

Brinkmann et al. [14] recently demonstrated an all-fiber FOPO pumped by a beam derived from a Yb-doped fiber oscillator mode-locked using a semiconductor saturable absorber mirror (SESAM). The system achieves wide tunability through a custom-made rapid spectral filter placed in the oscillator cavity. The pump tuning range, spanning from 1020 nm to 1060 nm, allows the FWM to cover the entire parametric gain of the used PCF, enabling access to both the fingerprint and C-H stretch Raman regions. However, it is important to note that the use of SESAM can affect the reliability of this light source due to its degradation over time.

A Fiber Optical Parametric Chirped-Pulse Oscillator (FOPCPO) has also been explored in the literature [112]. This approach involves significant stretching of the pump pulses to enhance their energy after amplification before injecting them into the FOPO to generate high-energy FWM. In FOPCPO systems, a free-space delay line is typically used within the parametric cavity to enable spectral tuning of the FWM sidebands, although with a limited range. However, including free-space components complicates the system's operation and negatively impacts its environmental stability.

An alternative approach for achieving a pump tunable over a sufficiently broad range to enable wide FOPO tuning has been demonstrated in Ref. [113–115]. The authors used an ultrafast Yb-doped oscillator with a fixed central wavelength. By incorporating a grating compressor within the cavity, the system generated femtosecond pulses, which were subsequently amplified and spectrally broadened in a fiber outside the oscillator. Tunable output was achieved through spectral filtration using a rotating galvanometric scanner in a 4-f configuration, followed by further amplification. However, the system was relatively complex, incorporating several free-space components, which compromised the long-term stability of the light source.

This chapter aims to describe a widely tunable FOPO that uses a tunable all-fiber pump based on an ultrafast oscillator at a fixed central wavelength. I will then implement a novel method of nonlinear spectral broadening of chirped pulses, the same as discussed in Section 5.3 of Chapter 5.

The following section will present the theoretical analysis of the FWM effect in LMA-PM-5 fiber, as used in this work. Next, in section 6.3, the development of the light source, including, in particular, the details of the construction and spectral and temporal characterization of the pump and parametric cavity, will be described. A conclusion of the achievements will be presented in Section 6.4.

6.2 Theoretical analysis

As will be shown in the next section, LMA-PM-5 Photonic Crystal Fiber (PCF) (from NKT Photonics) was used to generate the FWM nonlinear effect. Thus, a phase-matching analysis was performed to predict the spectral positions of the D-FWM sidebands generated in this fiber while varying the pump wavelengths.

The PCF was modeled using the COMSOL Multiphysics software based on the finite element method. The fiber structure, as illustrated in Figure 2.7a, was designed based on the AFM measurement of the fiber surface presented in Figure 2.9a of Chapter 2. The refractive index of silica was determined using the Sellmeier equation:

$$n^2(\lambda) = 1 + \frac{B_1\lambda^2}{\lambda^2 - C_1} + \frac{B_2\lambda^2}{\lambda^2 - C_2} + \frac{B_3\lambda^2}{\lambda^2 - C_3}, \tag{6.1}$$

where B_i and C_i are the Sellmeier coefficients, which for fused silica are equal to $B_1 = 0.696166300$, $B_2 = 0.407942600$, $B_3 = 0.897479400$, $C_1 = 4.67914826 \times 10^{-3}$, $C_2 = 1.35120631 \times 10^{-2}$, $C_3 = 97.9340025$. The effective refractive index as a function of the wavelength of the fundamental mode propagating in the PCF retrieved from the simulation is illustrated in panel (a) of Figure 6.1.

With these results, it was calculated the β_2, which is Group Velocity Dispersion (GVD):

$$\beta_2 = \frac{\lambda^3}{2\pi c^2}\frac{dn^2}{d\lambda^2}, \tag{6.2}$$

and then dispersion parameter (D):

$$D = -\frac{2\pi c}{\lambda^2}\beta_2 = -\frac{\lambda}{c}\frac{d^2n}{d\lambda^2}. \tag{6.3}$$

Figure 6.1b illustrates the calculated variation of β_2 and D as a function of wavelength (λ). As we can see, the calculated Zero Dispersion Wavelength (ZDW) of the LMA-PM-5 fiber is around 1060 nm.

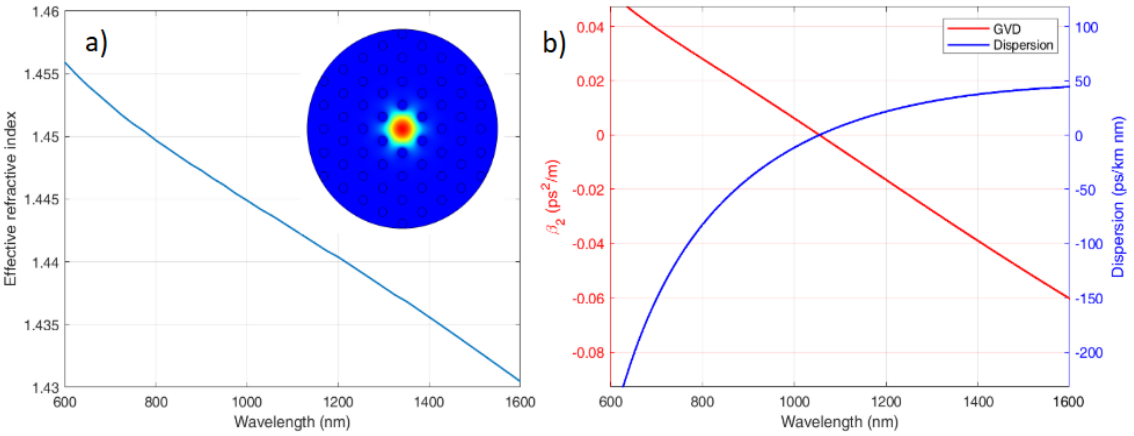

Figure 6.1: a) Effective refractive index as a function of wavelength. Inset: COMSOL of the fundamental mode of propagation of the PCF. b) GVD (β_2) (red) and D (blue) as a function of wavelength.

In the second step, a Matlab program was used to perform phase-matching analysis following Equations 3.24 and 3.25, which were discussed in detail in Section

3.4 of Chapter 3. Figure 6.2 presents the spectral position of the D-FWM sidebands of the signal (Anti-Stokes) and idler (Stokes) as a function of the pump wavelength. When tuning the pump wavelength from 1020 nm to 1090 nm, we can expect to obtain the D-FWM signal and idler varying from 728 nm to 1047 nm and 1700 nm to 1089 nm, respectively.

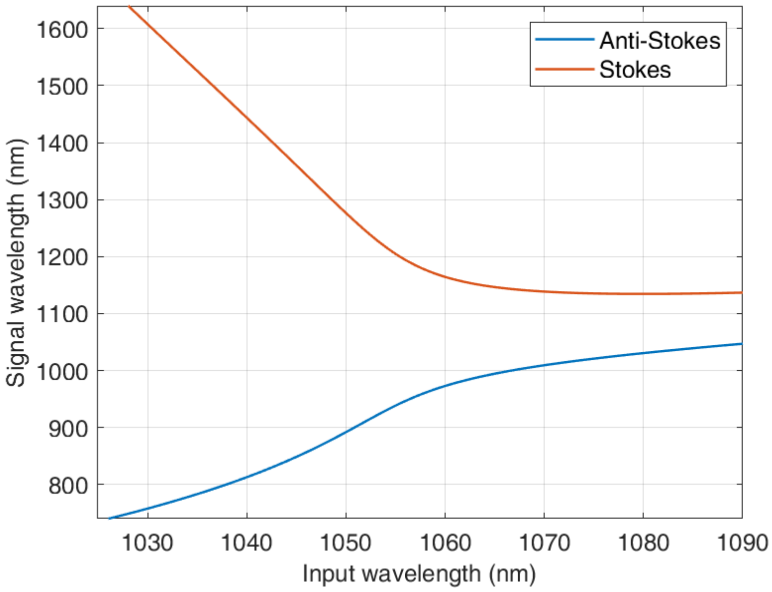

Figure 6.2: Calculated phase-matching diagram of anti-Stokes (blue) and Stokes (red).

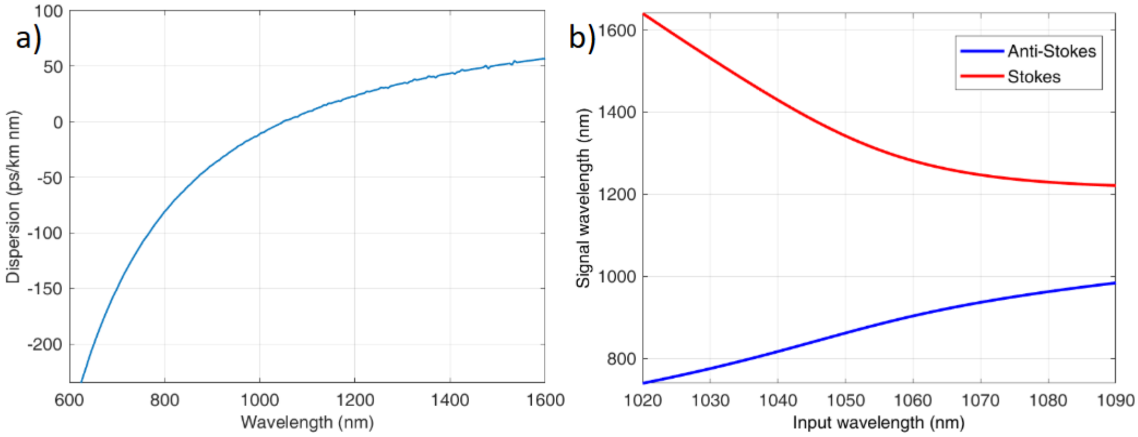

Figure 6.3: a) Dispersion curve provided by NKT Photonics and, b) calculated phase-matching diagram of anti-Stokes (blue) and Stokes (red).

To assess the obtained results, the phase-matching diagram was also calculated using the dispersion curve provided by the manufacturer (NKT Photonics) (Figure

6.3a) and is illustrated in Figure 6.3b. Discrepancies compared to the previous data (Figure 6.2) can be attributed to the parameters used in the COMSOL software. For example, minor changes in the fiber structure can lead to significantly different results. Additionally, the refractive index was determined from the Sellmeier equation, as the manufacturer did not provide precise accuracy parameters.

6.3 Experimental setup

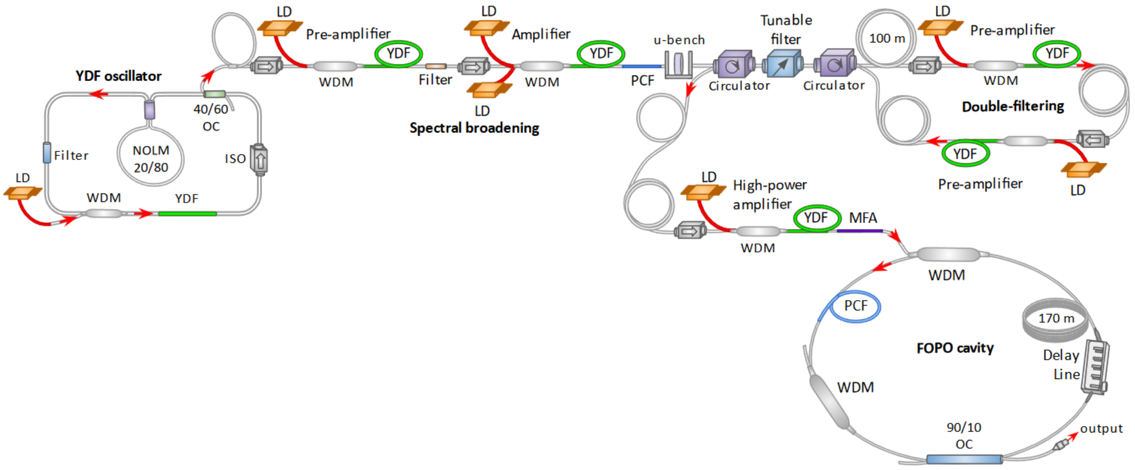

Figure 6.4: Experimental setup of the tunable D-FWM light source. YDF, Ytterbium-doped fiber; WDM, wavelength division multiplexer; LD, laser diode; ISO, optical isolator; NOLM, nonlinear optical loop mirror; OC, output coupler; PCF, photonic crystal fiber; MFA, mode-field adapter.

Figure 6.4 illustrates the schematic of the widely tunable D-FWM-based light source. It consists of two main components, described in the following sections: the all-fiber tunable pump and Fiber Optical Parametric Oscillator (FOPO). The entire source was constructed using Polarization-Maintaining (PM) fibers for stable operation.

6.3.1 All-fiber tunable pump beam based on the ultrafast oscillator operating at a fixed central wavelength

The pump arm utilized a similar architecture to the tunable Stokes arm of the SRS light source, previously described in Section 5.3. In short, it started with an ultrafast Yb-doped fiber oscillator emitting 9.5 ps chirped pulses at a fixed central wavelength of 1030 nm. These pulses were spectrally broadened via SPM in a chunk of an LMA-PM-5 fiber, preceded by pre-compression employing a 2 nm bandwidth fiberized spectral filter. The broadband light was then filtered through a 1 nm bandwidth tunable filter and amplified in a multistage amplifier with a double-filtration step.

In the current setup, a more powerful pump beam was required to generate high-power D-FWM sidebands efficiently. Therefore, the two final amplifiers, which delivered less than 1 W of average power, were replaced with a high-power Yb amplifier delivering up to 2 W. This amplifier was built using a 14 μm core diameter Yb-doped double-clad fiber (Coherent, PLMA-YDF-14/125-UF) and pumped by an 18 W continuous-wave (CW) diode laser at 976 nm. The larger core diameter, approximately three times that of the previous amplifiers, minimized unwanted nonlinear effects and preserved the narrow spectral width of the output pulses across the entire tuning range.

The results are presented in Figure 6.5. Panel (a) shows the pump spectra, tunable from 1025 nm to 1065 nm, with a spectral width of a few nanometers. Panel (b) illustrates the output power as a function of diode current for various pump wavelengths over the tuning range. For shorter wavelengths from 1025 nm to 1045 nm, it provides an output average power from 1.45 W up to 2.1 W, while for longer wavelengths from 1050 nm to 1065 nm, it is from 1.09 W to 0.58 W.

As expected, amplification at wavelengths near the edges of the Yb-doped fiber's gain curve was less efficient. Nevertheless, it still provided sufficient power for effectively seeding the FOPO.

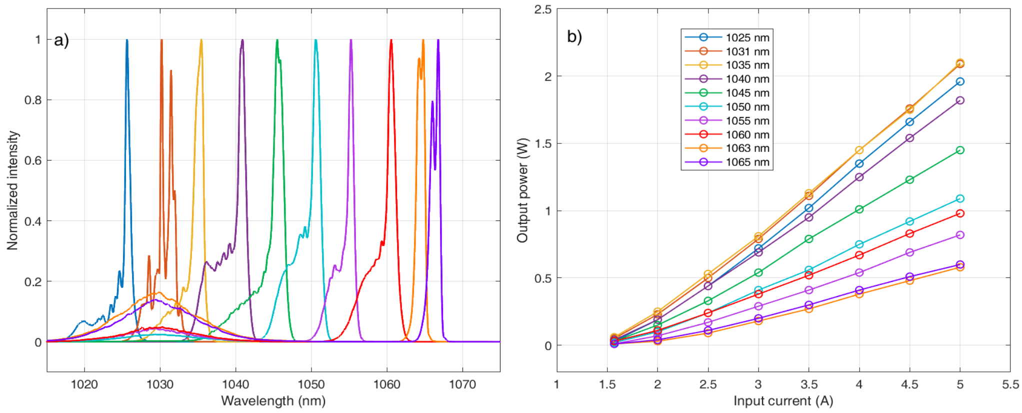

Figure 6.5: a) Spectra after the final amplification stage, output powers from 1.45 W up to 2.1 W (short wavelengths) and 1.09 W to 0.58 W (longer wavelengths). b) Output power as a function of diode current.

Figure 6.6 illustrates the pulse profile measured at the central wavelength of 1025 nm (a), 1030 nm (b), 1045 nm (c), and 1060 nm (d), respectively. As we can see, the pulse duration is around 4 ps, with minor fluctuations can be attributed to variations in output power.

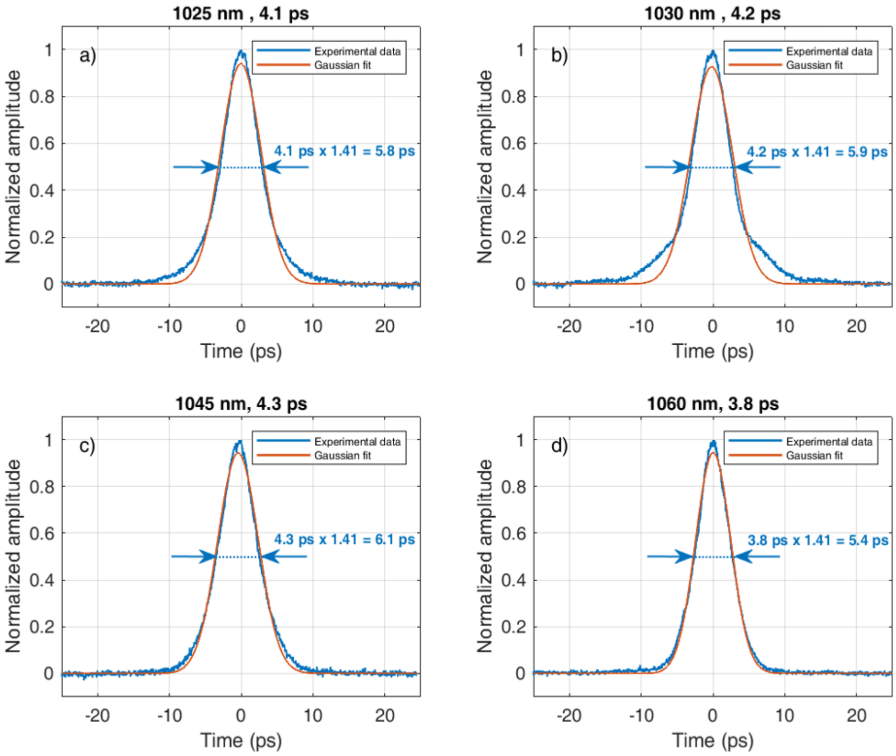

Figure 6.6: Pulse profile measured at 1 W of average power at the central wavelengths of: a) 1025 nm (4.1 ps), b) 1030 nm (4.2 ps), c) 1045 nm (4.3 ps), and d) 1060 nm (3.8 ps).

To provide more details about the construction of the pump arm, panels (a) and (b) of Figure 6.7 show the spectral evolution of the pump at central wavelengths of 1031 nm and 1060 nm as a function of output power, respectively. A clear difference in spectral dynamics is observed when amplified at the wavelength of maximum gain compared to the case of wavelength placed at the edge of the gain spectrum. Specifically, as previously mentioned, the amplification process is more efficient at the maximum gain wavelength and does not exhibit the unwanted additional amplified spontaneous emission (ASE) seen at 1060 nm.

At 1060 nm, the spectrum is less broadened, which can be attributed to the lower effective power in this spectrum region. Moreover, the less efficient broadening process is caused by the generated ASE, which contributes to the total output power and reduces the relative pump pulse intensity available for spectral broadening process.

The total output power and ASE background obtained at a fixed diode current for various wavelengths are shown in Figure 6.8a, represented by blue and red dots, respectively. Figure 6.8b presents corresponding data obtained instead using a simpler amplification scheme involving direct amplification without double-filtering, as illustrated in Figure 6.9. The significant reduction in ASE noise, particularly when amplifying the beam at wavelengths increasingly detuned from the maximum gain wavelength (1030 nm), highlights the advantages of the double-filtering configuration.

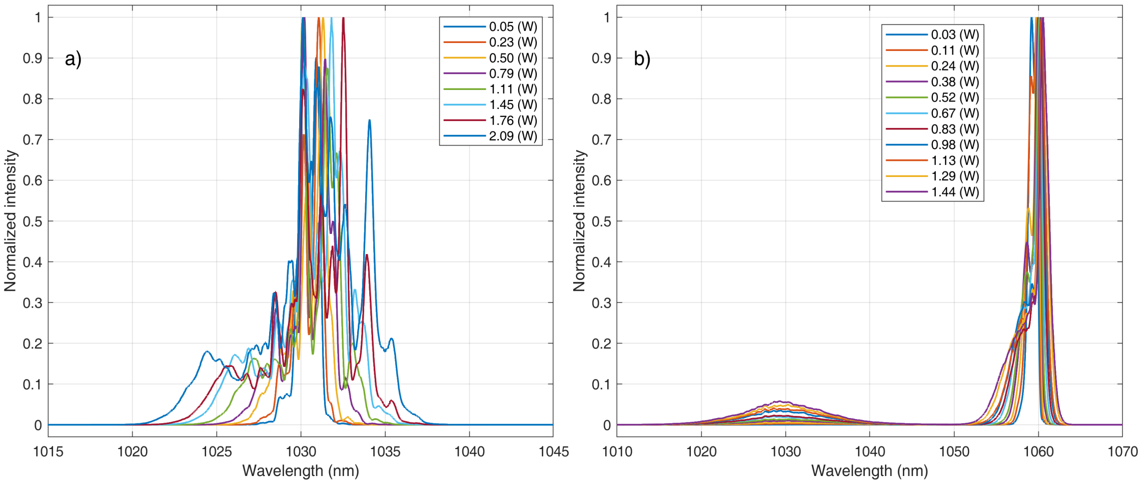

Figure 6.7: Spectra at a central wavelength of a) 1031 nm and b) 1060 nm as a function of the output power.

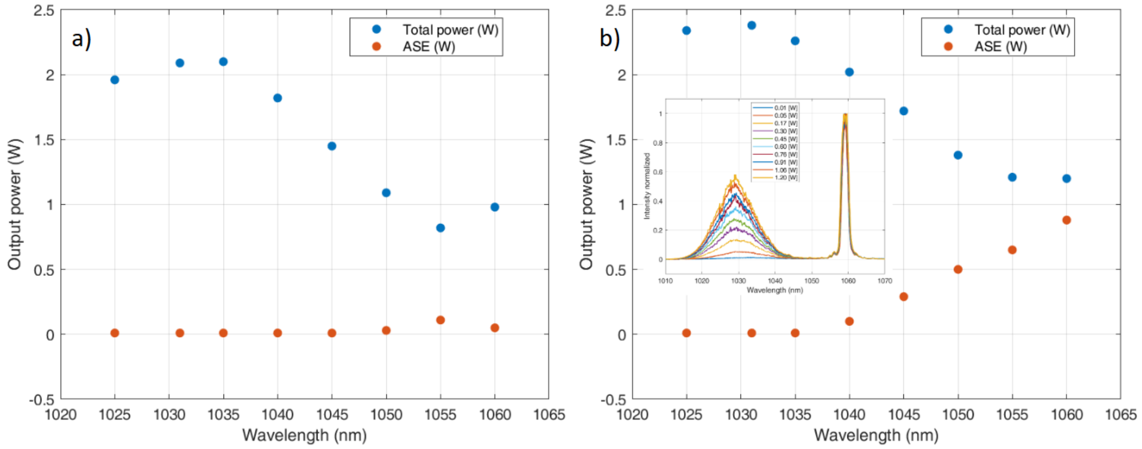

Figure 6.8: Output power. Total power (blue dot) and ASE power (red dot) at the input current of 5 A. a) Double-filtering multistage and b) simple amplification stage. Inset: spectra at the central wavelength of 1060 nm as a function of the output power.

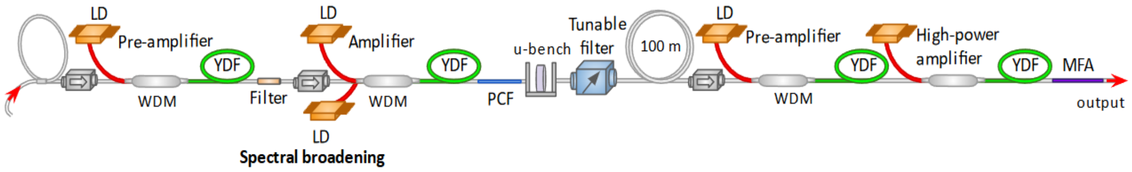

Figure 6.9: Experimental setup of the direct amplification.

6.3.2 The Fiber Optical Parametric Oscillator

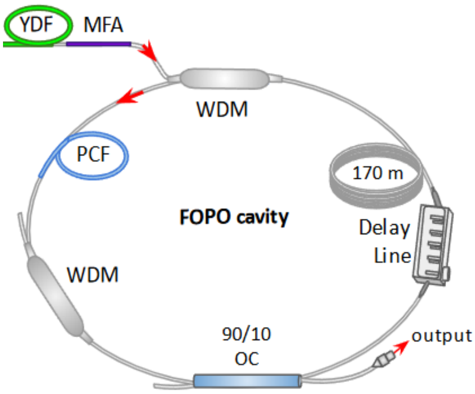

Figure 6.10: Schematic of the FOPO ring cavity.

The FOPO setup is schematically illustrated in Figure 6.10. Using the previously described tunable beam, it was pumped through a wavelength-division multiplexer 800/1064 nm (WDM). Since the WDM and the entire FOPO were constructed with optical fibers having a core diameter of approximately 5 μm, while the pump beam was delivered via a fiber with a 14 μm core diameter, a mode-field adapter (MFA) was used. The MFA was fabricated following the method described in Ref. [116], employing the thermally expanded core (TEC) technique to match the mode-field diameters of the two fibers. Directing splicing PM980 and PLMA14 results in transmission of 62.7 ± 0.5%. The MFA allowed the transmission efficiency to be achieved to 92 ± 0.5% after splicing.

The FOPO utilized D-FWM nonlinear effects, generated in a 42 cm long LMA-PM-5 fiber (from NKT Photonics). A second WDM (800/1064 nm) was placed after the PCF to filter out the residual pump beam. An output coupler with a 10:90 splitting ratio was employed to extract 90% of the D-FWM pulses from the cavity. To enable spectrally selective seeding, a 170 m segment of PM780 fiber (from Coherent) was spliced to stretch the D-FWM pulses temporally. This dispersive filter allowed the generation of D-FWM pulses with a narrow spectral bandwidth.

A fiber-based delay line capable of providing up to 500 ps of time delay was used for precise synchronization. The complete synchronization procedure between the pump and the D-FWM seed is described in detail in Appendix B.

Figure 6.11 illustrates the results obtained after careful synchronization between the pump and newly generated D-FWM pulses. The D-FWM signal spectra tunable from 730 nm to 940 nm as induced by the pump beam at the wavelengths tunable from 1025 nm to 1063 nm are presented in panel (a) of Figure 6.11. Panels (b) and (c) of Figure 6.11 show instead the corresponding values of the spectral width and output power. As can be seen, pulses with a spectral bandwidth of 2 nm and up to 13 mW of output power on average were achieved.

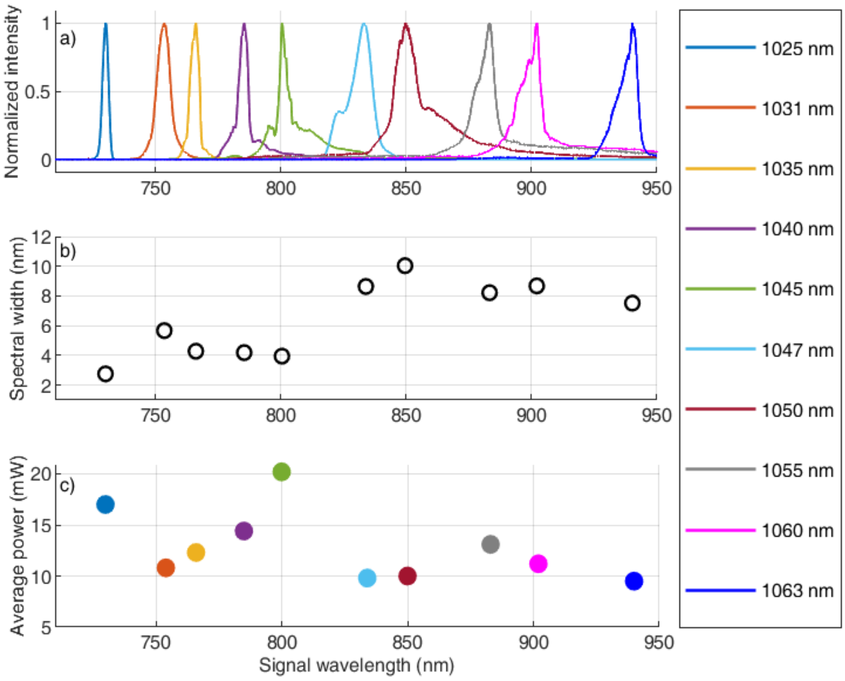

Figure 6.11: a) Synchronized D-FWM spectra generated for various pump wavelengths. b) Corresponding spectral width (black circles) and c) output average power of the D-FWM signals.

For comparison, the tunable D-FWM signal spectra in the non-synchronized case alongside their corresponding spectral widths, are shown in panels (a) and (b) of Figures 6.12, respectively. The results indicate that both cases achieve similar tunability and spectral bandwidth. However, the power is significantly higher in the synchronized case. In the non-synchronized case, the power was below 1 mW, which is the detection limit of our power meter. It is worth noting, however, that compared to purely spontaneous D-FWM (not shown here), the non-synchronized case in the cavity configuration still delivered D-FWM with a power level 16 dB higher, which despite the lack of synchronization between the cavities, some D-FWM pulses remained overlapped with the pump pulses.

Fine spectral tuning could also be performed by adjusting the FOPO cavity length at a fixed pump wavelength [12]. Figure 6.13 presents an example of the obtained results. It can be seen that by varying the cavity length from 1 cm to 16 cm, it can achieve the tuning of about 30 nm, from 880 to 910 nm, when D-FWM is induced by the pump at 1055 nm. Similar fine-tuning was observed for all the D-FWM signals.

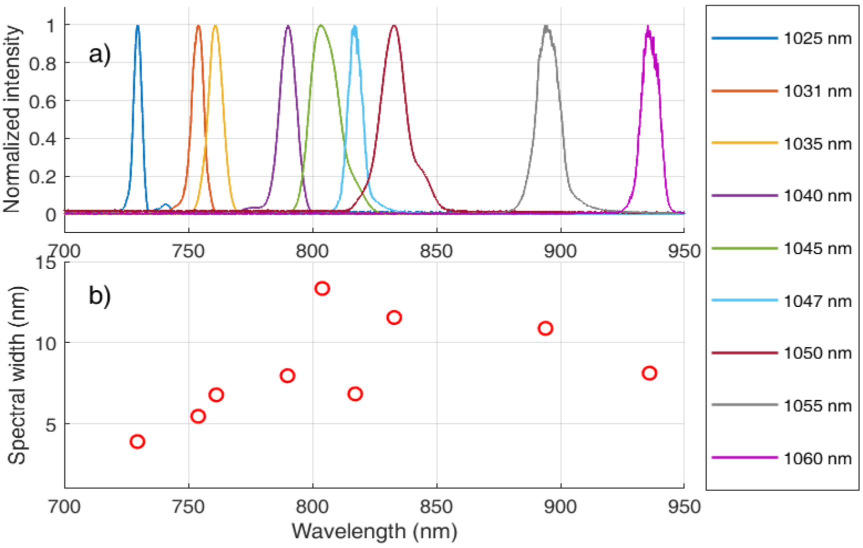

Figure 6.12: Non-synchronized D-FWM spectra generated for various pump wavelengths and b) corresponding spectral width (red circles).

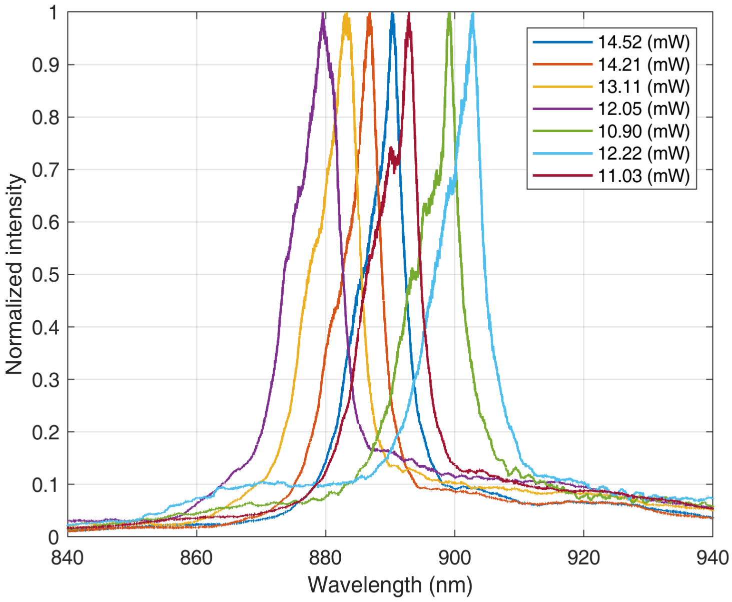

Figure 6.13: D-FWM tuning at the λ_p of 1055 nm.

The experimental results were compared with theoretical calculations. Figure 6.14 displays the theoretical phase-matching curves, calculated using the refractive index obtained from COMSOL simulations (blue) and the dispersion curve provided by NKT (green). The experimental spectral positions of the D-FWM signal are marked with red dots. To achieve better alignment with the measurements, the NKT dispersion curve was shifted by 10 nm, adjusting the Zero Dispersion Wavelength (ZDW) from 1050 nm to 1060 nm. The phase-matching diagram recalculated with the updated data is shown in red, demonstrating excellent agreement with the experimental results.

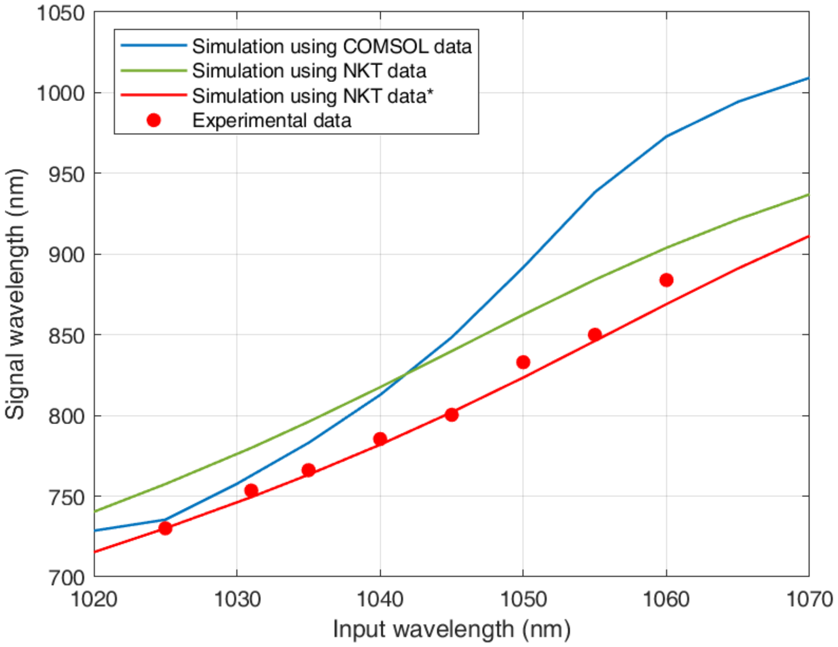

Figure 6.14: Simulated phase-matching curves (blue, green, and red lines) compared with experimental results (red dots).

Finally, the influence of the length of the LMA-PM-5 fiber on the generated D-FWM signal and its parameters was investigated. Figure 6.15 presents the D-FWM signal at 760 nm as a function of FOPO output power generated with the pump at 1030 nm in 52 cm long (a) and 42 cm long (b) LMA-PM-5, respectively. We can observe that by increasing the length of the PCF, the same power results in additional spectral broadening: a second peak emerges at 788 nm and grows larger for higher power. Careful PCF length optimization is required to avoid unwanted SCG and obtain only D-FWM sidebands.

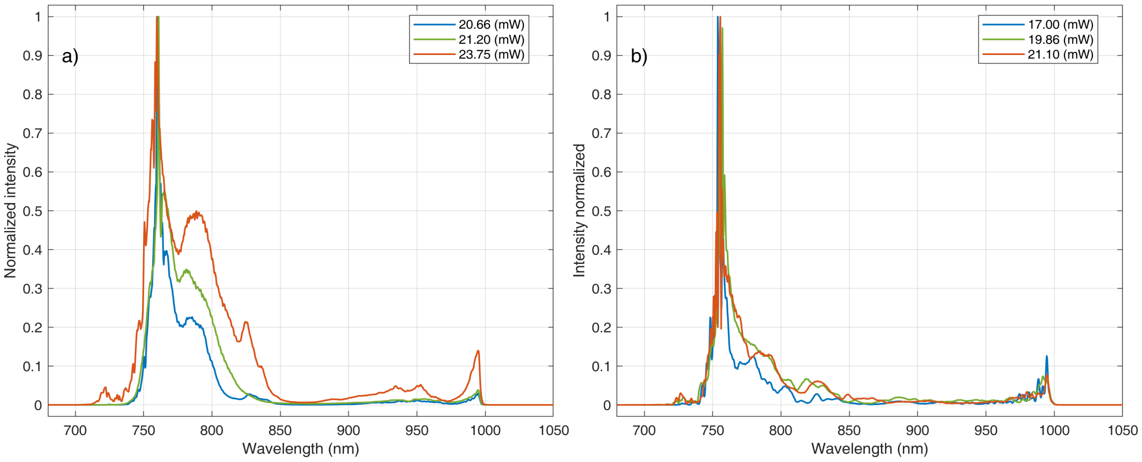

Figure 6.15: Evolution of D-FWM signal as a function of output power generated in 52 cm long (a) and 42 cm (b) long LMA-PM-5 pumped by 1030 nm beam.

6.4 Conclusions

In this chapter, I presented a widely tunable all-fiber light source composed of the tunable pump and the Fiber Optical Parametric Oscillator (FOPO) based on the resonant Degenerate-Four-Wave Mixing (D-FWM). The tunable pump was constructed in an all-fiber configuration starting from the Yb-doped fiber oscillator emitting 9.5 ps chirped pulses at a fixed central wavelength of 1030 nm. The pump beam delivered a tunability range spanning from 1025 nm to 1065 nm with 2 nm spectral bandwidth and output average power of 1.45 W up to 2.1 W (short wavelengths) and 1.09 W to 0.58 W (longer wavelengths). Its wavelength tunability was achieved with the same technique as described in Chapter 5. In short, by exploiting the SPM-induced spectral broadening enabled by a narrowband spectral filtration of chirped pulses, that was next spectrally filtered with a tunable filter and then amplified in a multistage amplifier with a double-filtration scheme.

Constructed FOPO delivers D-FWM signal tunable in the range from 730 nm to 940 nm with 2 nm spectral bandwidth and up to 13 mW of average power. Such a system holds potential for applications in nonlinear imaging, particularly Stimulated Raman Scattering-based imaging and spectroscopy. Indeed, when adding the second beam at 1030 nm, it can cover the wavenumbers from 929 cm^{-1} to 3990 cm^{-1}, allowing measurements across the fingerprint and C-H stretch regions.

Finally, the influence of the length of LMA-PM-5, in which D-FWM is generated, on the overall performance of the FOPO system was also discussed. It has been shown that too long of PCF generates SC, and its optimization is required to isolate the D-FWM nonlinear effect sufficiently.

Chapter 7

Widely tunable Four-Wave Mixing enabled by Self-Phase Modulation of chirped pulses

7.1 Introduction

As discussed in Chapter 6, the standard method for achieving broad tuning of FWM sidebands involves varying the wavelength of the laser serving as the pump beam. However, high-power ultrafast fiber lasers allowing for wavelength tunability across a range sufficient for FWM generation over the entire parametric gain are not commonly available. Recent advancements have demonstrated tunable FWM-based light sources using fixed-wavelength oscillators. FWM tuning achieved by adjusting the length of the parametric resonant cavity with a delay line, as shown in Ref. [12].

As mentioned in the introduction to Chapter 6, other solutions are however limited to a narrow range for obtaining broad tunability involves SPM spectral broadening generated by femtosecond pulses, followed by narrowband spectral filtering and amplification [113–115]. However, these setups are typically complex, requiring multiple free-space components that complicate system operation.

Here, I will demonstrate a tunable light source pumped by a laser with a fixed central wavelength. Unlike previous methods, a novel approach will be implemented to widely tune D-FWM sidebands. The method is based on SPM broadening of chirped pulses in a specially designed chain of fibers consisting of standard fiber and PCF. The details of this method will be described further in the chapter.

Section 7.2 will describe the experimental setup, the results obtained, and their interpretation. Numerical simulations supported by theoretical analysis providing deeper insight into the performed experiment will be presented in sections 7.3 and 7.4. Section 7.5 will report the application of the developed tunable light source for CARS imaging. Finally, section 7.6 will conclude the Chapter 7.

7.2 Experimental setup and results

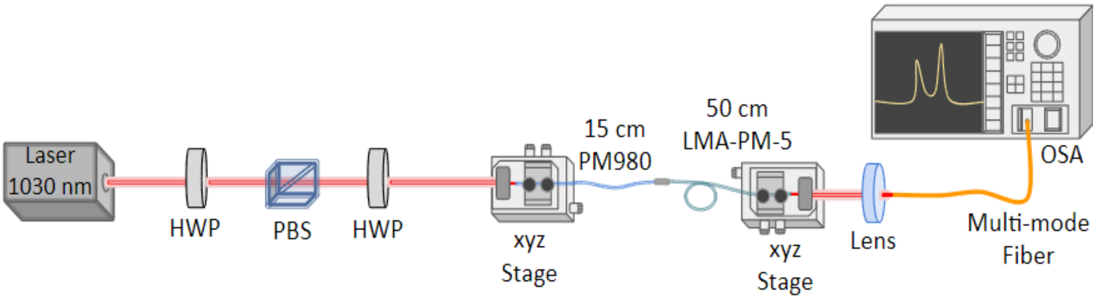

Figure 7.1: Experimental setup of the D-FWM enabled by SPM of chirped pulses. HPW, half-wave plate; PBS, polarization beam splitter; OSA, optical spectrum analyzer.

As illustrated in Figure 7.1, a commercial ultrafast fiber laser (from SPARK) operating at a fixed central wavelength of 1030 nm with a repetition rate of 2 MHz was used. The laser source provided optical pulses with durations tunable between 350 fs and 100 ps. The tunability was achieved by means of a set of diffraction gratings. A polarization beam splitter (PBS) sandwiched between two half-wave plates (HPWs) was employed to control both a beam power and a linear polarization state. The laser beam was injected into a 15 cm-long PM980 optical fiber (from Coherent) spliced to 50 cm-long LMA-PM-5 PCF (from NKT Photonics). Using an aspheric lens with a focal length of 6.2 mm allowed a coupling efficiency of 75%. At the output of PCF, a lens with a 25 mm focal length was employed instead to couple the light into a multimode fiber patch cord connected to an Optical Spectrum Analyzer (OSA, Yokogawa) for spectral measurements.

Figure 7.2 illustrates the heatmap of the output spectra measured at a peak power of 10 kW at different chirped pulse durations. As discussed in the previous Chapter 6, the standard method to shift D-FWM sidebands relies on varying the wavelength of the pump beam. The results demonstrate that the same large tunability of the D-FWM peaks can also be achieved by changing the chirp induced on the pump pulses while keeping their central wavelength fixed. Indeed, as observed in Figure 7.2, the D-FWM signal and idler can be tuned from 945 nm down to 750 nm and from 1220 nm up to 1675 nm, respectively, when varying the chirped pulse duration of the pump from 4 ps to 45 ps. The white dots in Figure 7.2 indicate the maximum intensity of the D-FWM sidebands.

To explain the observed effects, the pump spectral reshaping was measured for various chirped pulse durations. The SPM-induced spectral broadening for a pump peak power fixed at 10 kW was analyzed at the output of the PM980 fiber and at the output of the PM980 spliced with the LMA-PM-5. These results are shown in panels

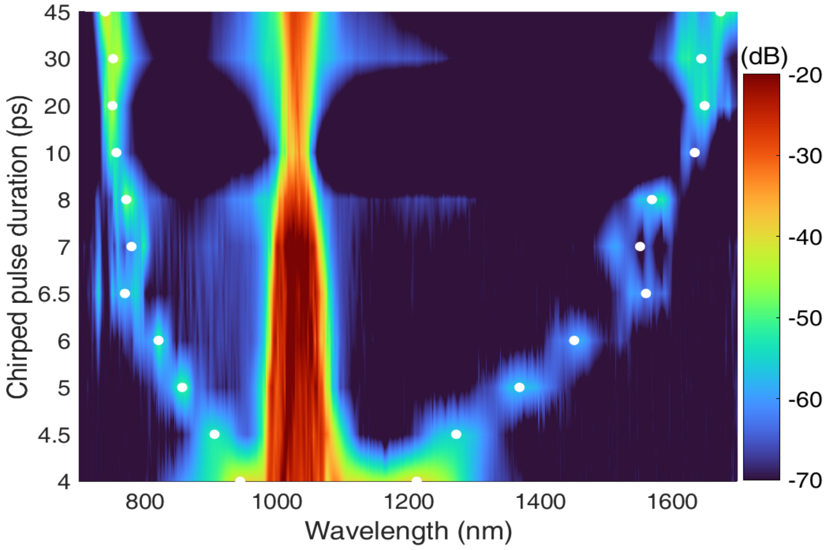

Figure 7.2: Output spectra for different chirped pulse durations at the fixed peak power of 10 kW (average powers were adjusted accordingly). White dots indicate the D-FWM sidebands.

(a) and (b) of Figure 7.3, respectively. They reveal that the spectral broadening begins in the first fiber (PM980) and continues in the second fiber (PCF).

As reported in Ref. [45], the efficiency of SPM depends on the amount of chirp applied to the pump pulses. Specifically, the spectrum undergoes weaker or stronger broadening depending on whether the chirp is larger or smaller, respectively. As the chirp changes, the multiple spectral peaks induced by SPM shift in their spectral positions, potentially acting as tunable pumps for D-FWM generation. However, the D-FWM sidebands observed in Figure 7.2 are narrower than expected if they were generated by the entire SPM spectrum. Numerical simulations presented in Section 7.3 indicate that the efficiency of D-FWM increases significantly when the pump wavelength approaches the ZDW of the PCF.

Based on this, the focus is on the outermost redshifted SPM peak (λ_{SPM}), marked by a black dot in Figure 7.3. The shift of λ_{SPM} as a function of chirped pulse duration, measured after the first and second fibers, is plotted in Figure 7.4 with blue squares and purple dots, respectively. When tuning the chirped pulse duration from 4 ps to 30 ps, λ_{SPM} moves from 1035 nm to 1041 nm after the first fiber. However, this shift is insufficient to explain the large variations in D-FWM sidebands observed experimentally (see Figure 7.2).

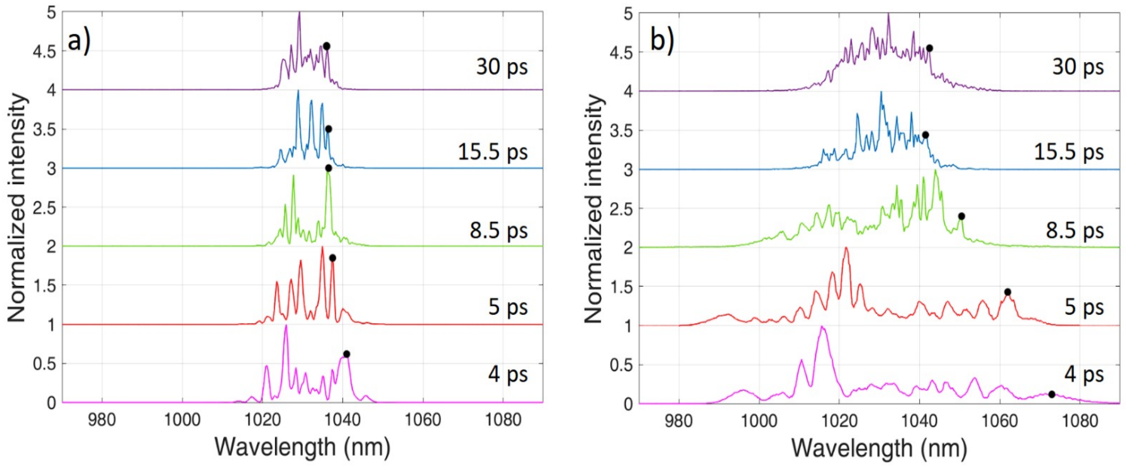

Figure 7.3: SPM spectra at the output of: a) 15 cm segment long PM980 and b) PM980 spliced with 50 cm segment long of LMA-PM-5. Black mark dots: the outermost redshifted peak.

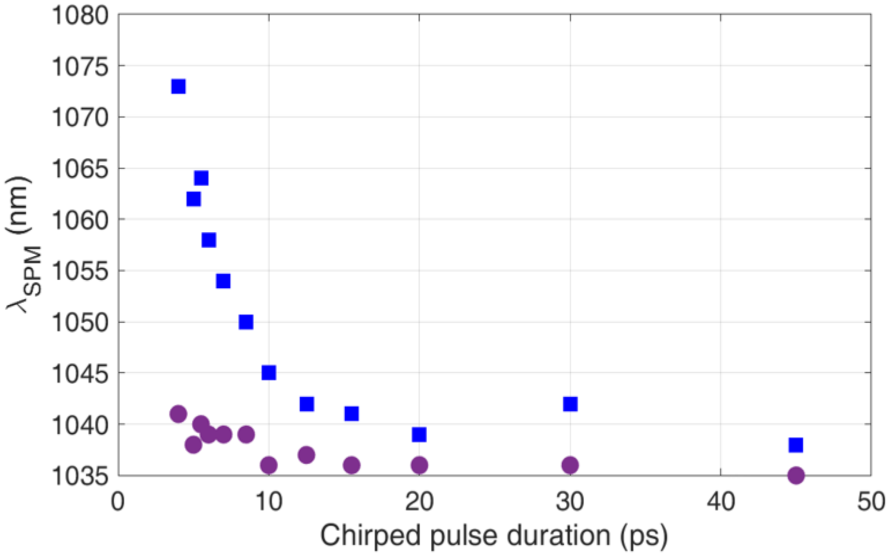

Figure 7.4: The λ_{SPM} as a function of the chirped pulse duration measured for the peak power of 10 kW at the output of PM980 (purple dots) and PM980 spliced with LMA-PM-5 (blue squares).

Importantly, as previously mentioned, the SPM continues in the LMA-PM-5 fiber, where λ_{SPM} extends further, reaching 1042 nm and 1070 nm for pulse durations of 30 ps and 4 ps, respectively. When the experimental results are compared with the three phase-matching diagrams discussed earlier in Chapter 6, as shown in Figure 7.5, they exhibit excellent agreement with the curves calculated using the adjusted NKT dispersion (represented by the red and blue solid lines). This, confirms that the tunable λ_{SPM} can act as a tunable pump in generating the D-FWM sidebands.

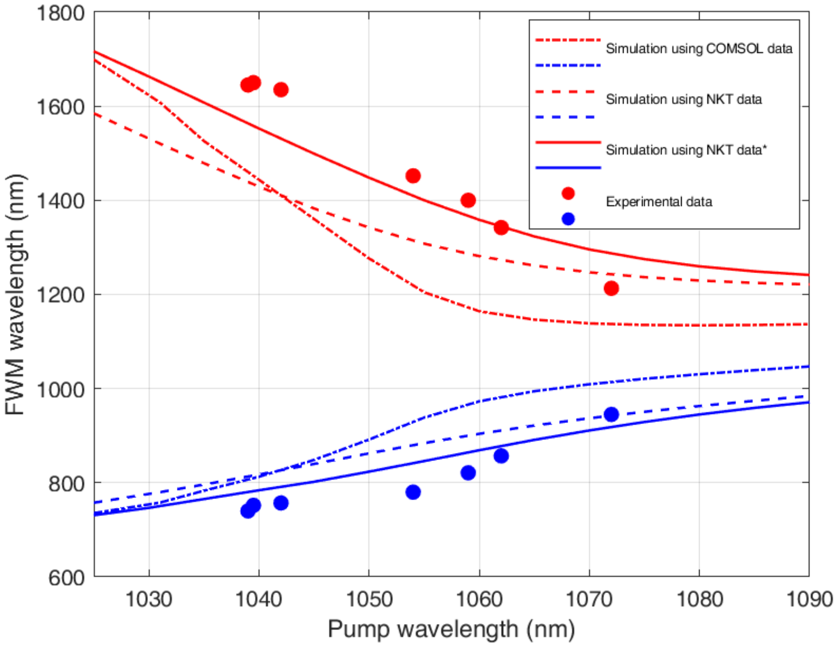

Figure 7.5: Phase-matching curves as a function of the pump wavelength. The dots represent the experimental result, while the solid, dashed, and dash-dotted lines correspond to theoretical calculations.

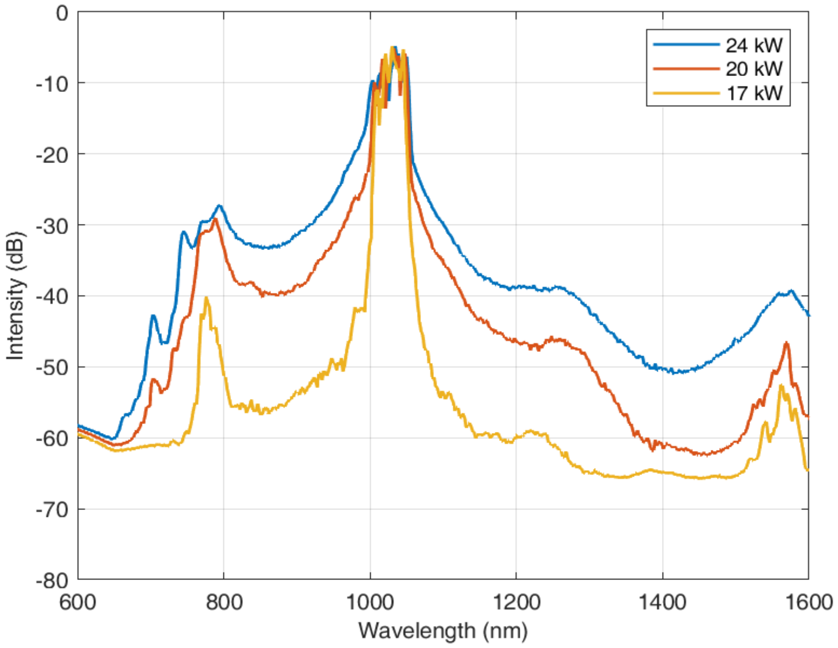

Figure 7.6: D-FWM spectral evolution measured with pump pulses of chirped temporal duration fixed to 7 ps as a function of peak power.

The influence of pump power at fixed chirp on the tunability of the D-FWM sidebands was also analyzed. Spectra measured for the pump power ranging from 17 kW to 24 kW and the pulse duration fixed to 7 ps are illustrated in Figure 7.6. One can notice that the position of the D-FWM remained unchanged when increasing the pump power. The spectrum rapidly evolved towards Supercontinuum instead. This effect was further confirmed by the numerical simulations presented in Section 7.3.

Finally, the spectral tuning of D-FWM sidebands was explored by varying the input linear state of polarization (SOP) of the pump beam. During the experiment, the chirped pulse duration and pump power were kept constant, while rotating the pump linear polarization using an HWP. Results obtained for 5.5 ps pulses with an average power of 250 mW are shown in Figure 7.7. These results reveal the sensitivity of the D-FWM sideband positions to the polarization angle.

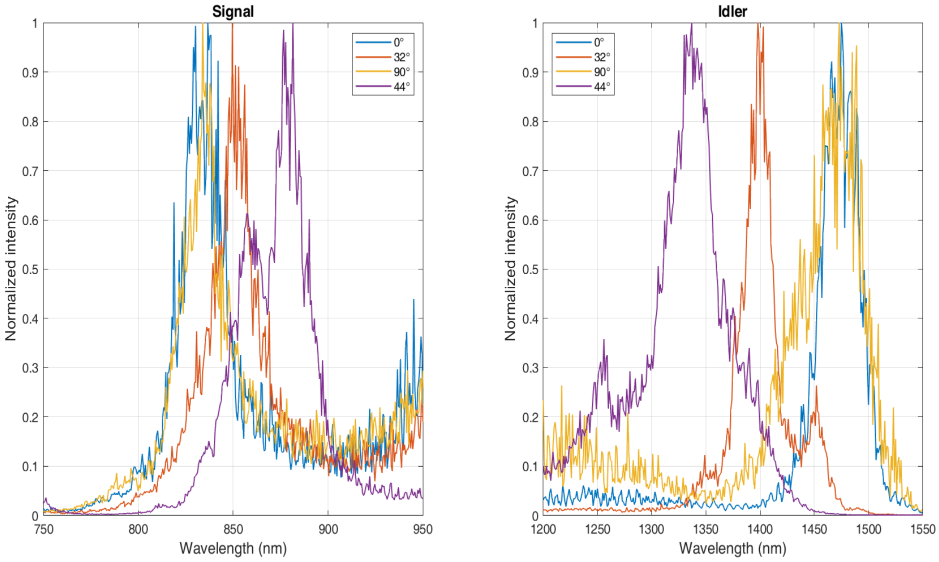

Figure 7.7: D-FWM spectra by varying the polarization of pump at the power of 250 mW, with a chirped pulse of 5.5 ps. a) Signal and b) idler.

PM fibers have two orthogonal axes, called slow and fast axes, which preserve the SOP of light propagating along either axes. In Figure 7.7, these axes are aligned with the angles 0° and 90°. When the light propagates along one of these axes, the D-FWM sidebands achieve the maximum spectral shift from the pump wavelength. As illustrated in Figure 7.7, the blue and yellow spectra for both signal and idler D-FWM, shown in panels (a) and (b), overlap and exhibit the shortest and longest wavelengths, respectively. The results indicates that the dispersion curves for both polarization states are essentially identical.

However, when the input linear polarization of the pump is rotated, the pump is divided into two polarization components as it propagates along the PM fibers. The birefringence of the fibers affects the D-FWM generation, leading to slight changes in the spectral positions of the sidebands, which allows for fine-tuning of the D-FWM signal and idler over 45 nm and 134 nm, respectively, for the 5.5 ps pulses.

7.3 Numerical simulations

To get a deeper understanding of the experimental observations, numerical simulations were conducted in collaboration with dr. hab. Alessandro Tonello from the Institute of XLIM of the University of Limoges in France, who developed a numerical code.

7.3.1 Numerical method

The numerical simulations have been performed using a code incorporating a generic propagation function for optical fibers, allowing for customization of dispersion profiles, effective core areas, and Kerr nonlinearity to match the characteristics of various fibers used in the experiments. Consistent with the experimental setup, the simulations considered the concatenation of a passive single-mode fiber segment (SMF) and a photonic crystal fiber segment (PCF). The output from the SMF served as the input for the PCF. It should be noted that the oscillator was not modeled in the simulations. Instead, to generate an input pulse resembling the positively chirped pulse from the experimental oscillator, we started with a transform-limited Gaussian pulse of 200 fs at a central wavelength of 1030 nm. Positive dispersion was applied to reshape this pulse accordingly.

The propagation code solves the scalar (i.e. polarization is not considered) Generalized Nonlinear Schrödinger Equation (GNLSE). This simplified model assumes that light polarization is not explicitly considered. The equation for the complex envelope A(z,t) implemented in a Matlab script is the following:

$$\left[\frac{\partial}{\partial z} - i\hat{D} + \frac{\alpha}{2}\right] A = i\gamma\left(1 + i\tau_S\frac{\partial}{\partial t}\right)\Bigg((1-f_R)A|A|^2 + f_R A(z,t)\int_0^\infty h_R(\xi)|A(z,t-\xi)|^2\,d\xi\Bigg), \tag{7.1}$$

where the linear operator $\hat{D}$ applied to the complex envelope $A(z,t)$ represents the fiber dispersion. The operator can be written as a sum developed in order M in the time domain.

$$i\hat{D}A = \sum_{m=2}^{M} i^{m-1}\frac{\beta_m}{m!}\frac{\partial^m A}{\partial t^m}. \tag{7.2}$$

The same operator $\hat{D}$ can be easily written in the frequency domain in the following way:

$$\tilde{D} = \beta(\omega) - \beta(\omega_0) - (\omega-\omega_0)\beta_1(\omega_0), \tag{7.3}$$

where $\beta(\omega)$ is the propagation constant at angular carrier frequency ω, ω_0 is the reference carrier frequency for a wavelength at 1030 nm and $\beta_m = (\partial\beta/\partial\omega)_{\omega=\omega_0}$. The operator $\tilde{D}$ models the linear dispersive propagation (see Equation 7.3): it is common that to reduce the overall cumulated phase in the numerical simulations, the phase velocity at ω_0 is subtracted from the propagation constant $\beta(\omega)$.

Moreover, rather than a fixed temporal frame referred to the lab, it is customary to reduce the computational load to choose a moving temporal frame following the pulse along the propagation. To optimize the computational efficiency, the time frame is chosen to travel at the pulse group velocity. This choice is reflected in the factor $\beta_1(\omega_0)$, which is the group delay per unit of length at the reference frequency ω_0. The time delay is represented in the frequency by the linear function in $(\omega - \omega_0)$. The parameter α accounts for linear losses. On the right-hand side of Equation 7.1 the nonlinear operators are represented. The first term corresponds to the instantaneous nonlinear effect, or electronic nonlinearity, while the second term represents the delayed molecular Raman response. The partition of the nonlinear susceptibility into instantaneous (Kerr effect) and delayed (Raman response) components is governed by the fraction f_R, which depends on the material properties of the fiber (silica glass). Specifically, the nearly instantaneous Kerr effect of electronic origin $(1 - f_R)A|A|^2$ contributes to nonlinear effects such as the SPM or the FWM.

The GNLSE, which incorporates both linear and nonlinear operators, is numerically solved using the split-step method. In this approach, the propagation is computed over small steps dz, allowing the linear operators (e.g., dispersion) and nonlinear operators to be applied separately at each step.

7.3.2 Simulation results

Figure 7.8 reports the numerical simulation of the D-FWM spectral evolution upon a chirped pulse duration varied from 2 ps to 5 ps at a pump peak power of 31 kW. These results agree with those previously presented in Figure 7.2 experimental results. Indeed, when the pulses get shorter, the D-FWM sidebands approach the pump wavelength.

Panel (a) in Figure 7.9 shows how the input spectrum evolves along the propagation distance z in the concatenation of PM980 and LMA-PM-5 fibers starting from the 3.3 ps chirped pulses with 31 kW peak power. Panel (b) in Figure 7.9 displays instead two examples of the corresponding spectra around the pump wavelength, computed at z = 0.15 m (purple curve), that is the output of PM980, and at z = 0.45 m (blue curve), that is after 0.30 m of propagation in the subsequent LMA-PM-5 fiber. It is evident that the pump spectrum starts to broaden within the first fiber and continues to expand in the PCF. At the onset of D-FWM, the λ_{SPM} reaches a

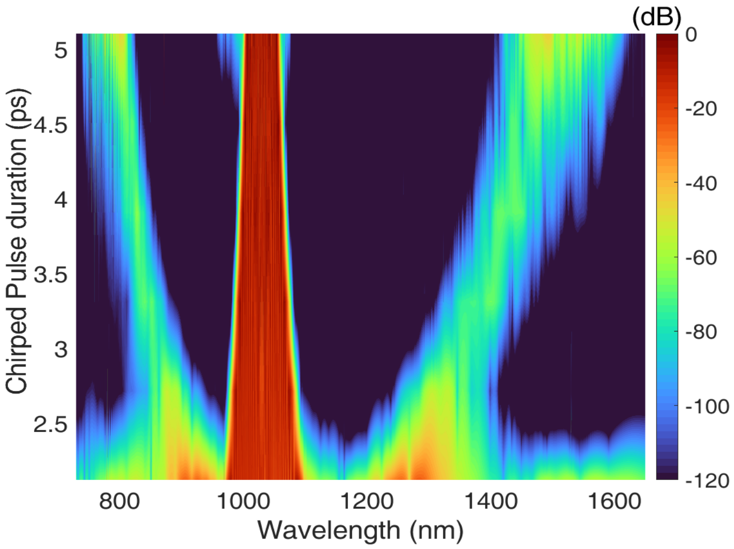

Figure 7.8: Numerical spectra by increasing the chirped pulse duration at a fixed peak power of 31 kW.

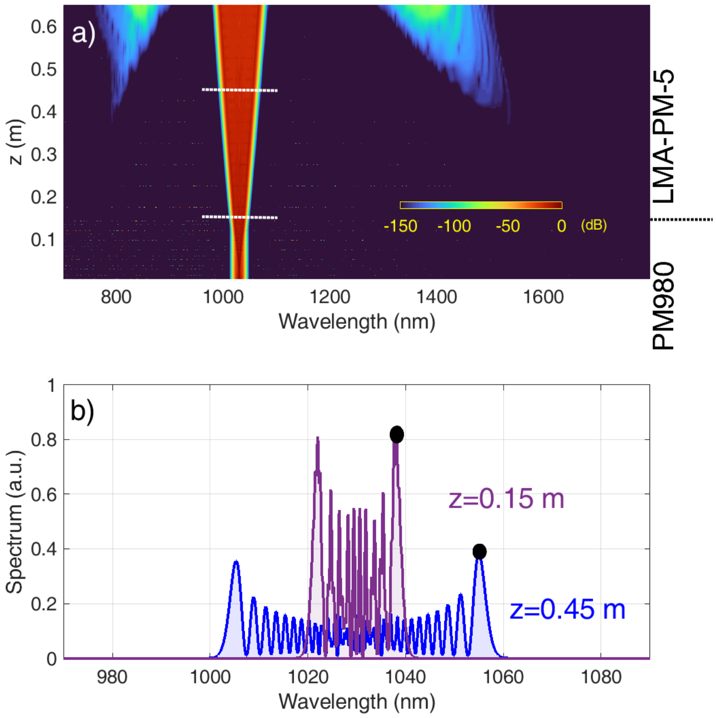

Figure 7.9: a) Spectral evolution along the propagation in a concatenation of PM980 and LMA-PM-5 for a chirped pulse of 3.3 ps and a peak power of 31 kW. b) Pump spectra at z = 0.15 m (purple), i.e. at the output of PM980, and at z = 0.45 m (blue) at the onset of D-FWM sidebands.

sufficiently large value to generate D-FWM sidebands at the maximum detuning, consistent with phase-matching predictions and in agreement with experimental results.

To better understand why, as previously assumed, the D-FWM is generated only by the outermost redshifted SPM peak, numerical simulations of the spectral evolution as a function of the chirped-free pulse of 5 ps and peak power of 2 kW, tunable from 1025 nm to 1060 nm were performed. The obtained results are illustrated in Figure 7.10. For better visualization, the central position of generated D-FWM sidebands is indicated with purple vertical lines. As the pump wavelength increases and gets closer to the ZDW of PCF, the D-FWM efficiency significantly increases. Indeed, as shown in the inset of Figure 7.10, the idler power exhibits an increase of more than 30 dB when generated with a pump at 1060 nm compared to 1025 nm.

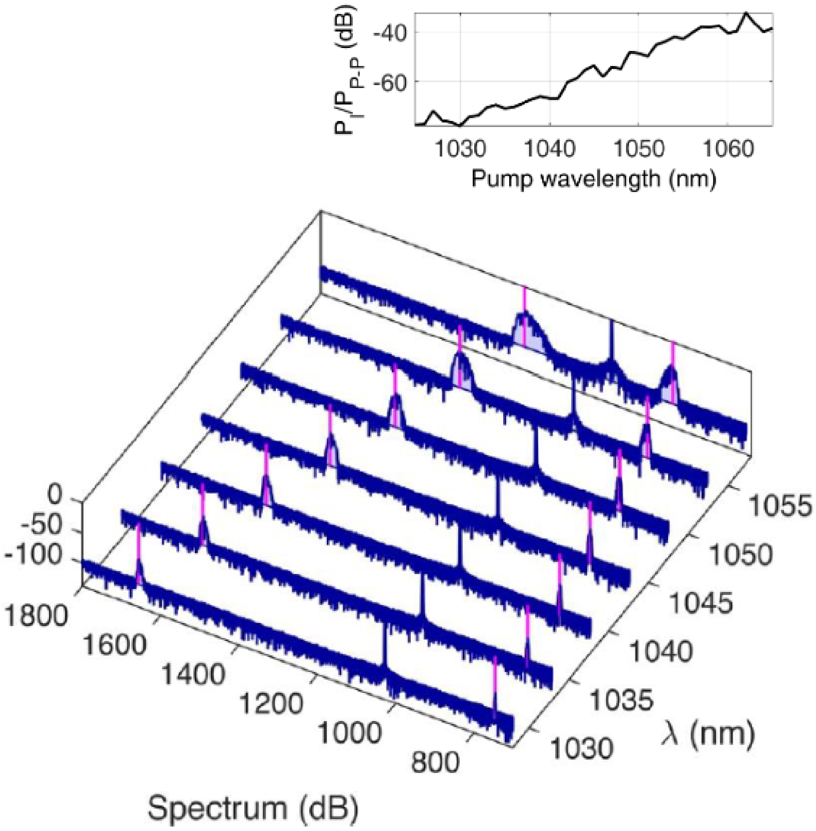

Figure 7.10: Numerical spectra obtained in 50 cm LMA-PM-5 for different pulse wavelength for 5 ps chirped-free pulses at 2 kW peak power (P_{P-P}) and, inset: calculated idler power P_I.

Finally, a numerical simulation also confirms that the D-FWM sidebands do not shift when increasing the pump power alone without changing the chirped pulse duration. Additionally, a numerical simulation was also performed to validate the observed SCG presented in Figure 7.6. The numerical simulations demonstrated a rapid transition to SCG as the pump power increases, as illustrated in Figure 7.11.

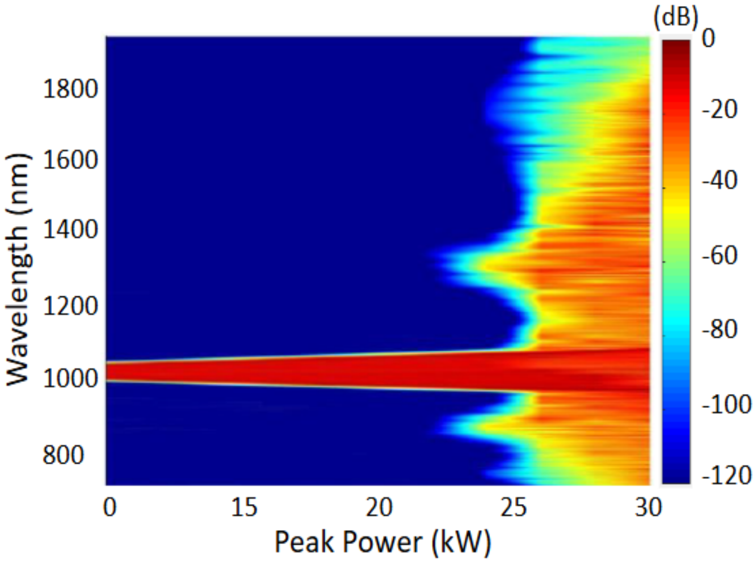

Figure 7.11: Numerical spectral evolution as a function of pump peak power with chirped pulse duration fixed to 2.7 ps.

7.4 Theoretical analysis

The electric field of the chirped pulse at the laser output can be described by the equation:

$$A(t, z = 0) = A_1 e^{-\frac{t^2(1+iC)}{2T_1^2}}, \tag{7.4}$$

where:

- $A(t, z = 0)$ is the electric field of the pulse at the fiber input (before propagation);
- t is time;
- A_1 is the amplitude of the stretched pulse;
- T_1 is the half pulse duration of the stretched pulse measured at exp(-1) in intensity; T_1 is related to the half temporal duration T_0 of the chirped-free pulse $T_1^2 = T_0^2(1 + C^2)$. Note that $T_{FWHM} = 2\sqrt{ln(2)}T_{HWEM}$, where T_{FWHM} is full pulse width at half maximum in intensity and T_{HWEM} is half pulse width at exp(-1) in intensity;

- C is the parameter chirp. The chirp C can be approximated as $C = \frac{T_1}{T_0}$.

Considering the pulse propagating into a nonlinear fiber of length L, where the nonlinear length is shorter than the dispersion length, the output spectrum can be described by Equation 7.5, if it is considering only the SPM effect:

$$\hat{A}(\omega, z = L) = \int_{-\infty}^{+\infty} A_1 e^{-\frac{t^2(1+iC)}{2T_1^2} + i\gamma |A(t)|^2 L} e^{i\omega t} dt, \tag{7.5}$$

the term $i\gamma|A(t)|^2 L$ represents the nonlinear phase shift caused by the SPM effect, where γ is the fiber nonlinear coefficient. Equation 7.5 can be simplified using the method of stationary phase, as demonstrated by Anderson et al. [45]:

$$\frac{\partial}{\partial t}\left[-\frac{Ct^2}{2T_1^2} + \gamma L |A(t)|^2 + \omega t \right] = 0, \tag{7.6}$$

this gives:

$$-\frac{Ct}{T_1^2} + \gamma L \frac{\partial |A(t)|^2}{\partial t} + \omega = 0. \tag{7.7}$$

From Equation 7.4:

$$|A(t)|^2 = |A_1|^2 e^{-\frac{t^2}{T_1^2}} \tag{7.8}$$

and thus:

$$\frac{\partial |A(t)|^2}{\partial t} = -\frac{2t}{T_1^2} |A_1|^2 e^{-\frac{t^2}{T_1^2}}. \tag{7.9}$$

Substituting Equation 7.9 into Equation 7.7, we obtain:

$$\omega = \frac{Ct}{T_1^2} + \frac{2\gamma L t}{T_1^2} |A_1|^2 e^{\frac{-t^2}{T_1^2}}. \tag{7.10}$$

Equation 7.10 shows how by stretching pulses and increasing their time duration (T_1) with the diffraction gratings can reduce the maximum spectral broadening along the nonlinear fiber L at fixed peak power.

7.5 Application to CARS imaging

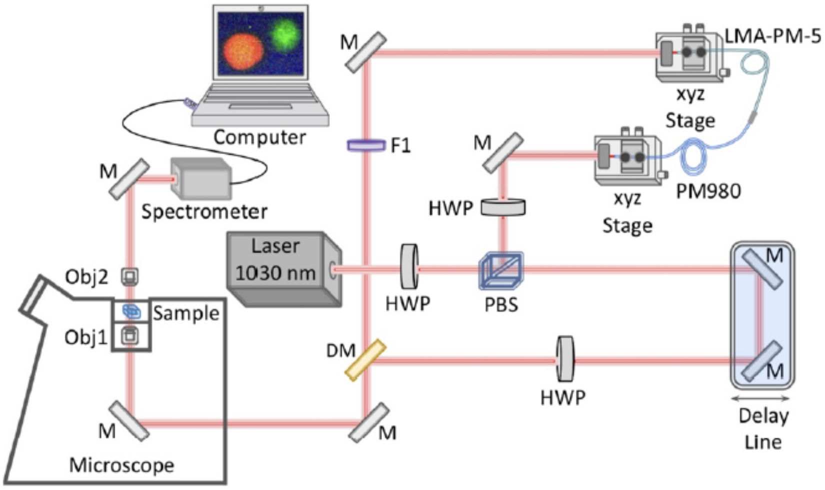

Figure 7.12: Experimental setup integrated into a CARS microscope.

The developed tunable light source was integrated into a CARS microscope to evaluate its performance for nonlinear imaging, as shown schematically in Figure 7.12. A portion of the 1030 nm input beam, redirected via a polarization beam splitter, served as the pump beam. The tunable idler beam was used as the Stokes beam, instead. To eliminate visible and NIR radiation up to 1100 nm, a long-pass filter (F1, FELH1000, Thorlabs) was employed. A dichroic mirror (DM, Thorlabs) was used to overlap the pump and Stokes beams spatially with real-time alignment allowed by a CCD camera. A free-space delay line (DL) stage was adjusted for temporal overlap by observing interference between the two 1030 nm beams. Figure 7.13 shows the spectrum without temporal overlap (in blue) and the interference fringes achieved after alignment (in red). Fine adjustment of the temporal overlap was further made during Raman measurements. The pump and Stokes beam power and polarization state were optimized using a density filter and a half-wave plate, respectively.

Finally, the beams were directed into a Nikon scanning stage microscope and focused onto the sample using a high numerical aperture objective lens (Obj1, LUMFLN60XW, Olympus). The CARS signal was collected using another high numerical aperture objective lens (Obj2, Nikon S Plan Fluor ELWD 60X) and analyzed with a Raman spectrometer (Horiba LabRAM).

We measured a sample consisting of a polystyrene bead and a droplet of paraffin, with the optical image shown in Figure 7.14. These compounds were chosen due to their well-characterized Raman spectra [109, 110], which exhibit strong peaks at 3050 cm^{-1} for polystyrene and 2849 cm^{-1} for paraffin. To differentiate the two compounds, we performed imaging by adjusting the chirped pulse duration from 5.5 ps to 6 ps, thereby tuning the idler central wavelength from 1500 nm to 1458 nm, as presented in Figure 7.15a. Examples of the corresponding CARS spectra are illustrated in Figure 7.15b. These spectra are consistent with those reported in the literature and reveal the main vibrational signatures of both investigated compounds.

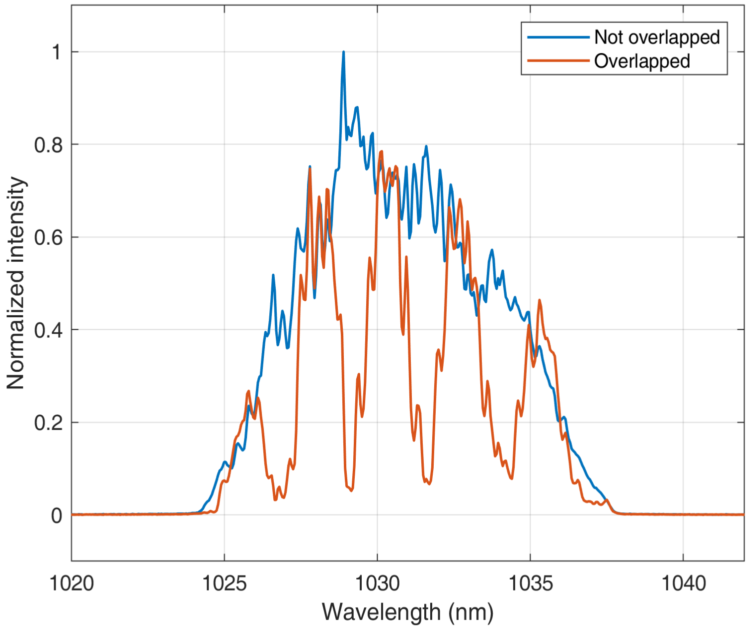

Figure 7.13: Spectra of two pulses temporally overlapped by adjusting the delay line.

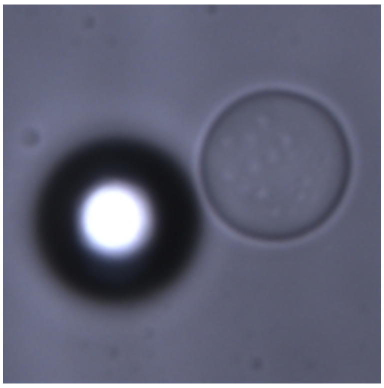

Figure 7.14: Optical image of a measured sample composed of the polystyrene bead (left) and a droplet of paraffin (right).

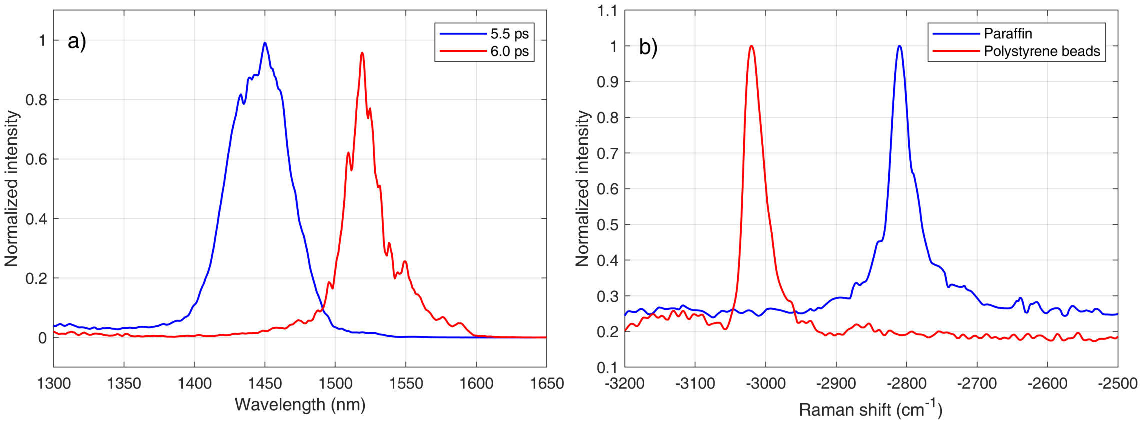

Figure 7.15: a) D-FWM idler spectrum obtained from 5.5 ps (blue) and 6.0 ps (red) pump. b) CARS spectra for paraffin (blue curve) and polystyrene bead (red curve).

Panels (a) and (b) in Figure 7.16 display the CARS images reconstructed from the Raman spectra near the vibrational frequencies associated with the paraffin droplet (2849 cm^{-1}) and the polystyrene bead (3050 cm^{-1}), respectively. In panel (a) of Figure 7.16, aside from the paraffin droplet, the low-intensity image of the polystyrene bead is also visible due to its weak Raman peak around 2845 cm^{-1}. Both images were acquired using a scanning step of 0.5 μm, an estimated spatial resolution of 0.4 μm, and a pixel integration time of 0.5 s.

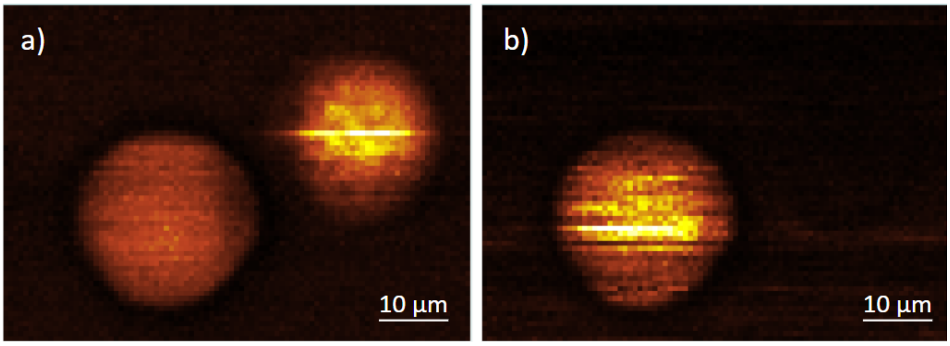

Figure 7.16: CARS images constructed from the Raman spectra around the Raman peak at a) 2849 cm^{-1} (droplet of paraffin) and b) 3050 cm^{-1} (polystyrene bead).

7.6 Conclusions

In this chapter, I demonstrated a new method of D-FWM spectral tunability. By varying a chirp pulse duration at a fixed pump wavelength, it is achieved a large shift of parametric sidebands within the range comparable to the one allowed by a standard technique of changing the pump wavelength. The tuning range extending from 750 nm to 945 nm for the D-FWM signal and from 1220 nm to 1675 nm for the

D-FWM idler was measured. This novel approach was achieved by concatenating two types of fibers, specifically PM980 and LMA-PM-5 fiber. The observed effect was enabled by the SPM of chirped pulses, where the outermost redshifted peak of the SPM served as a tunable pump for D-FWM generation. Specifically, the first fiber initiated the SPM process, while the second fiber further enhanced the SPM and allowed for the D-FWM generation.

It also observed the possibility of fine-tuning the D-FWM sidebands by exploiting the birefringence of the PM fibers. A tuning over 45 nm and 145 nm for the signal and idler was demonstrated.

This tunable light source was subsequently integrated into a CARS microscope and validated using a sample consisting of a polystyrene bead and a droplet of paraffin. By adjusting the D-FWM idler sideband, enables to selective image of each of the two components, demonstrating the potential of the developed light source for nonlinear imaging.

Chapter 8

Conclusions and Perspectives

This thesis was devoted to the development of fiber-based, widely-tunable laser sources for coherent Raman microscopy applications. Three different light sources were designed and built, leveraging nonlinear effects in optical fibers, including Self-Phase Modulation (SPM), Supercontinuum Generation (SCG), and Four-Wave Mixing (FWM). All systems utilized polarization-maintaining (PM) fibers and fiber components to ensure environmental stability. Each laser source was also based on the Ytterbium-doped fiber oscillator that delivered 9.5 ps chirped pulses at a repetition rate of 17.18 MHz. The oscillator was mode-locked via a Nonlinear Optical Loop Mirror (NOLM), ensuring reliable long-term operation. The work primarily exploited the normal dispersion regime of nonlinear beam propagation, enhancing the coherence of the spectral broadening used for achieving spectral tuning of the developed light sources.

I developed a dual-wavelength light source for SRS nonlinear imaging, capable of covering the fingerprint spectral region from 950 cm^{-1} to 1600 cm^{-1}. This light source delivered two beams with up to 40 mW average power, tunable from 1020 nm to 1070 nm for the Stokes beam and 913 nm to 930 nm for the pump beam, with a spectral bandwidth of less than 2 nm. The pump arm, tunable in the 920 nm spectral range, was based on SCG in an all-normal dispersion Photonic Crystal Fiber (PCF), achieved using the conventional approach of femtosecond pulse pumping. A free-space grating compressor was employed to compress chirped pulses from a 1030 nm ultrafast oscillator. To obtain broad tunability of the Stokes beam around 1030 nm, a novel all-fiber method was implemented for efficient spectral broadening via Self-Phase Modulation of chirped pulses. The chirped pulses were pre-compressed to a few picoseconds using a narrowband filter, enabling a spectral range of 85 nm. The broadband spectra generated in both the Stokes and pump arms were spectrally filtered using a tunable 1 nm-wide filter and subsequently amplified in Yb-doped and Nd-doped multistage amplifiers, respectively.

To extend the tunability range across both the fingerprint and C-H stretch

Raman regions, I developed a second fiber-based light source using the Degenerate-FWM (D-FWM) effect. This source delivered pulses with up to 13 mW average power, tunable from 730 nm to 940 nm. Combined with a second beam at 1030 nm, this enabled Raman measurements across a spectral range from 929 cm^{-1} to 3990 cm^{-1}. The laser was based on an ultrafast fiber oscillator operating at a fixed central wavelength. Wavelength tunability for generating the D-FWM sidebands was achieved externally to the oscillator cavity, using an innovative all-fiber approach, unlike many state-of-the-art methods. Specifically, the same all-fiber technique employed in the first source was utilized, leveraging SPM of chirped pulses, followed by spectral filtering and amplification in a multistage high-power fiber amplifier. D-FWM generation occurred within an all-Fiber Optical Parametric Oscillator (FOPO), significantly enhancing both the power and spectral resolution of the D-FWM sidebands compared to spontaneous D-FWM generation.

The third source I also developed based on the D-FWM effect, but here, a novel method for tuning the parametric sidebands using SPM. This approach provided a wide tuning range comparable to that achieved by the conventional method of tuning the pump wavelength. Instead of varying the pump wavelength, the chirp of the pump pulses injected into a concatenation of a PM fiber and an LMA-PM-5 fiber was adjusted. The first fiber initiated the SPM process, while the second fiber extended the SPM and generated the D-FWM. It was demonstrated that the outermost redshifted peak of the SPM spectrum could act as a tunable pump for D-FWM generation. Combined with a second beam at a fixed central wavelength of 1030 nm, this light source enabled measurements across the fingerprint and C-H stretch Raman regions. Specifically, it allowed access to a range from 873 cm^{-1} to 3624 cm^{-1} using the signal D-FWM sideband and from 1512 cm^{-1} to 3738 cm^{-1} with the idler D-FWM sideband.

Finally, to validate the light sources, they were integrated into Raman microscopes and conducted Raman imaging experiments. Using the first source, we achieved what we believe to be the first SRS imaging of leukemic cells in the fingerprint region, specifically at 1000 cm^{-1} and 1300 cm^{-1}. With the third source, we performed CARS imaging. CARS imaging was performed with a sample containing a droplet of paraffin and polystyrene beads, well capturing the Raman peaks at 2849 cm^{-1} and 3050 cm^{-1}, characteristic of these two compounds, respectively.

However, the developed three light sources can be further improved. Starting with the first laser designed for measurements in the fingerprint Raman region, a key challenge lies in the relatively weak SRS signal in this range compared to the strong signals typically observed in the C-H stretch region. One potential solution can be to address this limitation by reducing the pulse duration of both the Stokes and pump beams to just a few picoseconds. This approach would enhance the peak power for

SRS generation. However, it might come at the cost of increased spectral bandwidth at the output of the source, necessitating a well-considered design to balance these trade-offs. The study of chemical and molecular composition can also be expanded to include a wider range of samples beyond biological cells.

The FOPO system could also be further improved, primarily by increasing its output power, which could be accomplished by replacing the cavity's optical components with high-power alternatives. Furthermore, a PCF with a slightly shifted Zero Dispersion Wavelength could extend the tuning range, enabling coverage of the entire fingerprint and C-H stretch regions.

For the source exploiting the SPM-enabled D-FWM, its performance could be significantly enhanced by implementing a resonant cavity. This modification would help achieve a narrower spectral bandwidth while improving conversion efficiency.

Bibliography

[1] Yasuyuki Ozeki, Wataru Umemura, Yoichi Otsuka, Shuya Satoh, Hiroyuki Hashimoto, Kazuhiko Sumimura, Norihiko Nishizawa, Kiichi Fukui, and Kazuyoshi Itoh. High-speed molecular spectral imaging of tissue with stimulated raman scattering. *Nature photonics*, 6(12):845–851, 2012.

[2] I. Rocha-Mendoza, W. Langbein, and P. Borri. Coherent anti-stokes raman microspectroscopy using spectral focusing with glass dispersion. *Applied Physics Letters*, 93(20):201103, 2008.

[3] David J Jones, Eric O Potma, Ji-xin Cheng, Berndt Burfeindt, Yang Pang, Jun Ye, and X Sunney Xie. Synchronization of two passively mode-locked, picosecond lasers within 20 fs for coherent anti-stokes raman scattering microscopy. *Review of Scientific Instruments*, 73(8):2843–2848, 2002.

[4] C. Cleff, J. Epping, P. Gross, and C. Fallnich. Femtosecond opo based on lbo pumped by a frequency-doubled yb-fiber laser-amplifier system for cars spectroscopy microscopy. *Applied Physics B: Lasers and Optics*, 103:795–800, 2011.

[5] L. Kong, M. Ji, G. R. Holtom, D. Fu, C. W. Freudiger, and X. S. Xie. Multicolor stimulated raman scattering microscopy with a rapidly tunable optical parametric oscillator. *Optics Letters*, 38(2):145–147, 2013.

[6] Nicholas G Horton, Ke Wang, Demirhan Kobat, Catharine G Clark, Frank W Wise, Chris B Schaffer, and Chris Xu. In vivo three-photon microscopy of subcortical structures within an intact mouse brain. *Nature photonics*, 7(3):205–209, 2013.

[7] Grzegorz Soboń, Tadeusz Martynkien, Dorota Tomaszewska, Karol Tarnowski, Paweł Mergo, and Jarosław Sotor. All-in-fiber amplification and compression of coherent frequency-shifted solitons tunable in the 1800–2000 nm range. *Photonics Research*, 6(5):368–372, 2018.

[8] L Rishøj, Boyin Tai, Poul Kristensen, and Siddharth Ramachandran. Soliton self-mode conversion: revisiting raman scattering of ultrashort pulses. *Optica*, 6(3):304–308, 2019.

[9] Etienne Genier, Sacha Grelet, Rasmus D Engelsholm, Patrick Bowen, Peter M Moselund, Ole Bang, John M Dudley, and Thibaut Sylvestre. Ultra-flat, low-noise, and linearly polarized fiber supercontinuum source covering 670–1390 nm. *Optics Letters*, 46(8):1820–1823, 2021.

[10] Nicola Coluccelli, Vikas Kumar, Marco Cassinerio, Gianluca Galzerano, Marco Marangoni, and Giulio Cerullo. Er/tm: fiber laser system for coherent raman microscopy. *Optics letters*, 39(11):3090–3093, 2014.

[11] Erin S Lamb, Simon Lefrancois, Minbiao Ji, William J Wadsworth, X Sunney Xie, and Frank W Wise. Fiber optical parametric oscillator for coherent anti-stokes raman scattering microscopy. *Optics letters*, 38(20):4154–4157, 2013.

[12] Thomas Gottschall, Tobias Meyer, Martin Baumgartl, Benjamin Dietzek, Jürgen Popp, Jens Limpert, and Andreas Tünnermann. Fiber-based optical parametric oscillator for high resolution coherent anti-stokes raman scattering (cars) microscopy. *Optics express*, 22(18):21921–21928, 2014.

[13] Mario Chemnitz, Martin Baumgartl, Tobias Meyer, Cesar Jauregui, Benjamin Dietzek, Jürgen Popp, Jens Limpert, and Andreas Tünnermann. Widely tuneable fiber optical parametric amplifier for coherent anti-stokes raman scattering microscopy. *Optics express*, 20(24):26583–26595, 2012.

[14] Maximilian Brinkmann, Alexander Fast, Tim Hellwig, Isaac Pence, Conor L Evans, and Carsten Fallnich. Portable all-fiber dual-output widely tunable light source for coherent raman imaging. *Biomedical optics express*, 10(9):4437–4449, 2019.

[15] Walter Fu and Frank W Wise. Normal-dispersion fiber optical parametric chirped-pulse amplification. *Optics letters*, 43(21):5331–5334, 2018.

[16] N. S. Kapany. *Fiber optics. Principles and applications.* New York: Academic Press, 1967.

[17] K Charles Kao and George A Hockham. Dielectric-fibre surface waveguides for optical frequencies. In *Proceedings of the Institution of Electrical Engineers*, pages 1151–1158. IET, 1966.

[18] Felix P Kapron, Donald B Keck, and Robert D Maurer. Radiation losses in glass optical waveguides. *Applied Physics Letters*, 17(10):423–425, 1970.

[19] William G French, John B MacChesney, PB O'connor, and GW Tasker. Bstj brief: Optical waveguides with very low losses. *The Bell system technical journal*, 53(5):951–954, 1974.

[20] Terenuma Miya, Yukio Terunuma, Tatsuya Hosaka, and Tadakazu Miyashita. Ultimate low-loss single-mode fibre at 1.55 μ m. *Electronics Letters*, 4(15):106–108, 1979.

[21] Rajiv Ramaswami, Kumar Sivarajan, and Galen Sasaki. *Optical networks: a practical perspective.* Morgan Kaufmann, 2009.

[22] Gerd Keiser. *Optical fiber communications.* New York: McGraw-Hill, 2000.

[23] Govind P. Agrawal. *Fiber-optic communication systems.* Wiley and Sons, 2012.

[24] J. Tyndall. *Notes of a course of nine lectures on LIGHT.* Longmans, Green, and Company, 1870.

[25] J. Tyndall. *Six Lectures on Light: Delivered in America in 1872-1873.* Longmans, Green, 1873.

[26] Govind P. Agrawal. *Nonlinear Fiber Optics.* Elsevier, 2013.

[27] Tingye Li. *Optical fiber communications: fiber fabrication.* Elsevier, 1985.

[28] T Hosaka, K Okamoto, T Miya, Y Sasaki, and T Edahiro. Low-loss single polarisation fibres with asymmetrical strain birefringence. *Electronics Letters*, 15(17):530–531, 1981.

[29] Wolfgang Hänsel, Heinar Hoogland, Michele Giunta, Sebastian Schmid, Tilo Steinmetz, Ralf Doubek, Peter Mayer, Sven Dobner, Carsten Cleff, Marc Fischer, et al. All polarization-maintaining fiber laser architecture for robust femtosecond pulse generation. *Exploring the World with the Laser: Dedicated to Theodor Hänsch on his 75th birthday*, pages 331–340, 2018.

[30] Claude Aguergaray, Ryan Hawker, Antoine FJ Runge, Miro Erkintalo, and Neil GR Broderick. 120 fs, 4.2 nj pulses from an all-normal-dispersion, polarization-maintaining, fiber laser. *Applied Physics Letters*, 103(12), 2013.

[31] Jan Szczepanek, Tomasz M Kardaś, Maria Michalska, Czesław Radzewicz, and Yuriy Stepanenko. Simple all-pm-fiber laser mode-locked with a nonlinear loop mirror. *Optics letters*, 40(15):3500–3503, 2015.

[32] Tongxiao Jiang, Yifan Cui, Pei Lu, Chen Li, Aimin Wang, and Zhigang Zhang. All pm fiber laser mode locked with a compact phase biased amplifier loop mirror. *IEEE Photonics Technology Letters*, 28(16):1786–1789, 2016.

[33] Erich Götzinger, Bernhard Baumann, Michael Pircher, and Christoph K Hitzenberger. Polarization maintaining fiber based ultra-high resolution spectral domain polarization sensitive optical coherence tomography. *Optics express*, 17(25):22704–22717, 2009.

[34] Tim A Birks, Jonathan C Knight, and P St J Russell. Endlessly single-mode photonic crystal fiber. *Optics letters*, 22(13):961–963, 1997.

[35] Jonathan C Knight. Photonic crystal fibres. *nature*, 424(6950):847–851, 2003.

[36] Philip Russell. Photonic crystal fibers. *science*, 299(5605):358–362, 2003.

[37] P. St. J. Russell and R. Dettmer. A neat idea [photonic crystal fibre]. *IEE Review*, 47(5):19–23, 2001.

[38] P Weinberger. John kerr and his effects found in 1877 and 1878. *Philosophical Magazine Letters*, 88(12):897–907, 2008.

[39] John Kerr. Xl. a new relation between electricity and light: Dielectrified media birefringent. *The London, Edinburgh, and Dublin Philosophical Magazine and Journal of Science*, 50(332):337–348, 1875.

[40] John Kerr. Liv. a new relation between electricity and light: Dielectrified media birefringent (second paper). *The London, Edinburgh, and Dublin Philosophical Magazine and Journal of Science*, 50(333):446–458, 1875.

[41] Fujio Shimizuj. frequency broadening in liquids by a short light pulse. *Physical Review Letters*, 19(19):1097– 1100, 1967.

[42] EP Ippen, CV Shank, and TK Gustafson. Self-phase modulation of picosecond pulses in optical fibers. *Applied Physics Letters*, 24(4):190–192, 1974.

[43] R. H. Stolen and Chinlon Lin. Self-phase-modulation in silica optical fibers. *Physical Review A*, 17(4):1448–1453, 1977.

[44] WJ Tomlinson, Roger H Stolen, and Anthony M Johnson. Optical wave breaking of pulses in nonlinear optical fibers. *Optics letters*, 10(9):457–459, 1985.

[45] Dan Anderson, M Desaix, M Lisak, and Manuel L Quiroga-Teixeiro. Wave breaking in nonlinear-optical fibers. *JOSA B*, 9(8):1358–1361, 1992.

[46] J Scott Russell. Report on waves. In *Report of the fourteenth meeting of the British Association for the Advancement of Science*, volume 25, 1844.

[47] Norman J Zabusky and Martin D Kruskal. Interaction of" solitons" in a collisionless plasma and the recurrence of initial states. *Physical review letters*, 15(6):240, 1965.

[48] Akira Hasegawa and Frederick Tappert. Transmission of stationary nonlinear optical pulses in dispersive dielectric fibers. i. anomalous dispersion. *Applied Physics Letters*, 23(3):142–144, 1973.

[49] Mark J Ablowitz and Peter A Clarkson. *Solitons, nonlinear evolution equations and inverse scattering*, volume 149. Cambridge university press, 1991.

[50] Aleksei Shabat and Vladimir Zakharov. Exact theory of two-dimensional self-focusing and one-dimensional self-modulation of waves in nonlinear media. *Sov. Phys. JETP*, 34(1):62, 1972.

[51] Akira Hasegawa and Yuji Kodama. *Solitons in optical communications.* Oxford University Press, 1995.

[52] Robert W. Boyd. *Nonlinear Optics.* Third edition. Ap, 2007.

[53] Yuen-Ron Shen. *Principles of nonlinear optics.* Wiley, New York, 1984.

[54] R H_ Stolen, EP Ippen, and AR Tynes. Raman oscillation in glass optical waveguide. *Applied Physics Letters*, 20(2):62–64, 1972.

[55] RH Stolen and EP Ippen. Raman gain in glass optical waveguides. *Applied Physics Letters*, 22(6):276–278, 1973.

[56] Reuben Shuker and Robert W Gammon. Raman-scattering selection-rule breaking and the density of states in amorphous materials. *Physical Review Letters*, 25(4):222, 1970.

[57] R. R. Alfano and S. L. Shapiro. emission in the region 4000 to 7000 a via four-photon coupling in glass. *Physical Review Letters*, 24(11):584–587, 1970.

[58] Chinlon Lin and R. H. Stolen. New nanosecond continuum for excited-state spectroscopy. *Applied Physics Letters*, 28(4):216–218, 1976.

[59] P. L. Baldeck and R. R. Alfano. Intensity effects on the stimulated four photon spectra. *Lightwave Technology*, 5(12):1712–1715, 1987.

[60] P Beaud, W Hodel, B Zysset, and H Weber. Ultrashort pulse propagation, pulse breakup, and fundamental soliton formation in a single-mode optical fiber. *IEEE journal of quantum electronics*, 23(11):1938–1946, 1987.

[61] Mohammed N Islam, G Sucha, Israel Bar-Joseph, M Wegener, James P Gordon, and Daniel S Chemla. Femtosecond distributed soliton spectrum in fibers. *JOSA B*, 6(6):1149–1158, 1989.

[62] I Ilev, H Kumagai, K Toyoda, and I Koprinkov. Highly efficient wideband continuum generation in a single-mode optical fiber by powerful broadband laser pumping. *Applied optics*, 35(15):2548–2553, 1996.

[63] WH Reeves, Dmitry V Skryabin, Fabio Biancalana, Jonathan C Knight, P St J Russell, FG Omenetto, Anatoly Efimov, and Antoinette Jane Taylor. Transformation and control of ultra-short pulses in dispersion-engineered photonic crystal fibres. *Nature*, 424(6948):511–515, 2003.

[64] Stephane Coen, Alvin Hing Lun Chau, Rainer Leonhardt, John D Harvey, Jonathan C Knight, William J Wadsworth, and Philip St J Russell. Supercontinuum generation by stimulated raman scattering and parametric four-wave mixing in photonic crystal fibers. *JOSA B*, 19(4):753–764, 2002.

[65] Ö Boyraz, J Kim, MN Islam, F Coppinger, and B Jalali. 10 gb/s multiple wavelength, coherent short pulse source based on spectral carving of supercontinuum generated in fibers. *Journal of Lightwave Technology*, 18(12):2167, 2000.

[66] AB Rulkov, MY Vyatkin, SV Popov, JR Taylor, and VP Gapontsev. High brightness picosecond all-fiber generation in 525–1800nm range with picosecond yb pumping. *Optics Express*, 13(2):377–381, 2005.

[67] Stefan Demmler, Jan Rothhardt, Alexander M Heidt, Alexander Hartung, Erich G Rohwer, Hartmut Bartelt, Jens Limpert, and Andreas Tünnermann. Generation of high quality, 1.3 cycle pulses by active phase control of an octave spanning supercontinuum. *Optics express*, 19(21):20151–20158, 2011.

[68] Jinendra K Ranka, Robert S Windeler, and Andrew J Stentz. Visible continuum generation in air–silica microstructure optical fibers with anomalous dispersion at 800 nm. *Optics letters*, 25(1):25–27, 2000.

[69] William J Wadsworth, Jonathan C Knight, A Ortigosa-Blanch, J Arriaga, E Silvestre, and P St J Russell. Soliton effects in photonic crystal fibres at 850nm. *Electronics Letters*, 36(1):1, 2000.

[70] John M. Dudley; Goery Genty; and Stephane Coen. Supercontinuum generation in photonic crystal fiber. *Review Modern Physics*, 78:1135–1184, 2006.

[71] C. V. Raman and K. S. Krishnan. A new type of secondary radiation. *Nature*, 121(2):501–502, 1928.

[72] Theodore H. Maiman. Stimulated optical radiation in ruby. *Nature*, 187:493–494, 1960.

[73] Alfons Weber, Sergio PS Porto, Leonard E Cheesman, and Joseph J Barrett. High-resolution raman spectroscopy of gases with cw-laser excitation. *JOSA*, 57(1):19–28, 1967.

[74] Michel Delhaye and Paul Dhamelincourt. Raman microprobe and microscope with laser excitation. *Journal of Raman spectroscopy*, 3(1):33–43, 1975.

[75] Dario Polli, Vikas Kumar, Carlo M Valensise, Marco Marangoni, and Giulio Cerullo. Broadband coherent raman scattering microscopy. *Laser & Photonics Reviews*, 12(9):1800020, 2018.

[76] Monika Gniadecka, Peter Alshede Philipsen, Sonja Wessel, Robert Gniadecki, Hans Christian Wulf, Sigurdur Sigurdsson, Ole Faurskov Nielsen, Daniel Højgaard Christensen, Jana Hercogova, Kristian Rossen, et al. Melanoma diagnosis by raman spectroscopy and neural networks: structure alterations in proteins and lipids in intact cancer tissue. *Journal of investigative dermatology*, 122(2):443–449, 2004.

[77] Renate Petry, Michael Schmitt, and Jürgen Popp. Raman spectroscopy—a prospective tool in the life sciences. *chemphyschem*, 4(1):14–30, 2003.

[78] J. X. Cheng and X. S. Xie. *Coherent Raman scattering microscopy.* CRC press, 2016.

[79] Christoph Krafft, Iwan W Schie, Tobias Meyer, Michael Schmitt, and J Popp. Developments in spontaneous and coherent raman scattering microscopic imaging for biomedical applications. *Chemical Society Reviews*, 45(7):1819–1849, 2016.

[80] Debmalya Roy, Sanjay Kanojia, Kingsuk Mukhopadhyay, and N Eswara Prasad. Analysis of carbon-based nanomaterials using raman spectroscopy: principles and case studies. *Bulletin of Materials Science*, 44(1):31, 2021.

[81] E.J. Woodbury and W. K. Ng. Ruby laser operation in the near ir. *Proc. IRE*, 50(11):2347–2348, 1962.

[82] Gisela Eckhardt, Robert W Hellwarth, Fred J McClung, Steven E Schwarz, Daniel Weiner, and EJ Woodbury. Stimulated raman scattering from organic liquids. *Physical Review Letters*, 9(11):455, 1962.

[83] Philipp Kukura, David W McCamant, and Richard A Mathies. Femtosecond stimulated raman spectroscopy. *Annu. Rev. Phys. Chem.*, 58(1):461–488, 2007.

[84] Andreas Zumbusch, Gary R Holtom, and X Sunney Xie. Three-dimensional vibrational imaging by coherent anti-stokes raman scattering. *Physical review letters*, 82(20):4142, 1999.

[85] Christian W Freudiger, Wei Min, Brian G Saar, Sijia Lu, Gary R Holtom, Chengwei He, Jason C Tsai, Jing X Kang, and X Sunney Xie. Label-free biomedical imaging with high sensitivity by stimulated raman scattering microscopy. *Science*, 322(5909):1857–1861, 2008.

[86] R. W. Maker, P. D.; Terhune. Study of optical effects due to an induced polarization third order in the electric field strength. *Physical Review*, 137:A801–A818, 1965.

[87] RF Begley, AB Harvey, and Robert L Byer. Coherent anti-stokes raman spectroscopy. *Applied Physics Letters*, 25(7):387–390, 1974.

[88] Michael D Duncan, J Reintjes, and TJ Manuccia. Scanning coherent anti-stokes raman microscope. *Optics letters*, 7(8):350–352, 1982.

[89] Conor L Evans and X Sunney Xie. Coherent anti-stokes raman scattering microscopy: chemical imaging for biology and medicine. *Annu. Rev. Anal. Chem.*, 1(1):883–909, 2008.

[90] A. Zumbusch, G. R. Holtom, and X. S. Xie. Three-dimensional vibrational imaging by coherent anti-stokes raman scattering. *Physical Review Letters*, 82(20):4142–4145, 1999.

[91] Hideaki Kano and Hiro-o Hamaguchi. Ultrabroadband (> 2500cm- 1) multiplex coherent anti-stokes raman scattering microspectroscopy using a supercontinuum generated from a photonic crystal fiber. *Applied Physics Letters*, 86(12), 2005.

[92] Tak W Kee and Marcus T Cicerone. Simple approach to one-laser, broadband coherent anti-stokes raman scattering microscopy. *Optics letters*, 29(23):2701–2703, 2004.

[93] Sapun H Parekh, Young Jong Lee, Khaled A Aamer, and Marcus T Cicerone. Label-free cellular imaging by broadband coherent anti-stokes raman scattering microscopy. *Biophysical journal*, 99(8):2695–2704, 2010.

[94] Bernhard von Vacano, Lars Meyer, and Marcus Motzkus. Rapid polymer blend imaging with quantitative broadband multiplex cars microscopy. *Journal of Raman Spectroscopy: An International Journal for Original Work in all Aspects of Raman Spectroscopy, Including Higher Order Processes, and also Brillouin and Rayleigh Scattering*, 38(7):916–926, 2007.

[95] Evelyn Ploetz, Stefan Laimgruber, Stefan Berner, Wolfgang Zinth, and Peter Gilch. Femtosecond stimulated raman microscopy. *Applied Physics B*, 87:389–393, 2007.

[96] Dan Fu, Fa-Ke Lu, Xu Zhang, Christian Freudiger, Douglas R Pernik, Gary Holtom, and Xiaoliang Sunney Xie. Quantitative chemical imaging with multiplex stimulated raman scattering microscopy. *Journal of the American Chemical Society*, 134(8):3623–3626, 2012.

[97] Ji-xin Cheng, Andreas Volkmer, Lewis D Book, and X Sunney Xie. Multiplex coherent anti-stokes raman scattering microspectroscopy and study of lipid vesicles. *The Journal of Physical Chemistry B*, 106(34):8493–8498, 2002.

[98] Masanari Okuno, Hideaki Kano, Philippe Leproux, Vincent Couderc, and Hiro-o Hamaguchi. Ultrabroadband multiplex cars microspectroscopy and imaging using a subnanosecond supercontinuum light source in the deep near infrared. *Optics letters*, 33(9):923–925, 2008.

[99] Thomas Hellerer, Annika MK Enejder, and Andreas Zumbusch. Spectral focusing: High spectral resolution spectroscopy with broad-bandwidth laser pulses. *Applied Physics Letters*, 85(1):25–27, 2004.

[100] Adrian F Pegoraro, Andrew Ridsdale, Douglas J Moffatt, Yiwei Jia, John Paul Pezacki, and Albert Stolow. Optimally chirped multimodal cars microscopy based on a single ti: sapphire oscillator. *Optics express*, 17(4):2984–2996, 2009.

[101] Aaron D Slepkov, Andrew Ridsdale, Adrian F Pegoraro, Douglas J Moffatt, and Albert Stolow. Multimodal cars microscopy of structured carbohydrate biopolymers. *Biomedical optics express*, 1(5):1347–1357, 2010.

[102] Leila B Mostaço-Guidolin, Michael G Sowa, Andrew Ridsdale, Adrian F Pegoraro, Michael SD Smith, Mark D Hewko, Elicia K Kohlenberg, Bernie Schattka, Masashi Shiomi, Albert Stolow, et al. Differentiating atherosclerotic plaque

burden in arterial tissues using femtosecond cars-based multimodal nonlinear optical imaging. *Biomedical optics express*, 1(1):59–73, 2010.

[103] Bryce Manifold, Elena Thomas, Andrew T Francis, Andrew H Hill, and Dan Fu. Denoising of stimulated raman scattering microscopy images via deep learning. *Biomedical optics express*, 10(8):3860–3874, 2019.

[104] Lili Zhang, Yongzheng Wu, Bin Zheng, Lizhong Su, Yuan Chen, Shuang Ma, Qinqin Hu, Xiang Zou, Lie Yao, Yinlong Yang, et al. Rapid histology of laryngeal squamous cell carcinoma with deep-learning based stimulated raman scattering microscopy. *Theranostics*, 9(9):2541, 2019.

[105] Christian W Freudiger, Wenlong Yang, Gary R Holtom, Nasser Peyghambarian, X Sunney Xie, and Khanh Q Kieu. Stimulated raman scattering microscopy with a robust fibre laser source. *Nature photonics*, 8(2):153–159, 2014.

[106] Daniel A. Orringer and Sandra Camelo-Piragua. Rapid intraoperative histology of unprocessed surgical specimens via fibre-laser-based stimulated raman scattering microscopy. *Nature biomedical engineering*, 1(0027):1–13, 2017.

[107] Cihang Kong, Christian Pilger, Henning Hachmeister, Xiaoming Wei, Tom H Cheung, Cora SW Lai, Nikki P Lee, Kevin K Tsia, Kenneth KY Wong, and Thomas Huser. High-contrast, fast chemical imaging by coherent raman scattering using a self-synchronized two-colour fibre laser. *Light: Science & Applications*, 9(1):25, 2020.

[108] Etienne Genier, Amar N Ghosh, Swetha Bobba, Patrick Bowen, Peter M Moselund, Ole Bang, John M Dudley, and Thibaut Sylvestre. Cross-phase modulation instability in pm andi fiber-based supercontinuum generation. *Optics Letters*, 45(13):3545–3548, 2020.

[109] Aart A van Apeldoorn, Y Aksenov, M Stigter, I Hofland, Joost Dick de Bruijn, HK Koerten, Cornelis Otto, Jan Greve, and CA Van Blitterswijk. Parallel high-resolution confocal raman sem analysis of inorganic and organic bone matrix constituents. *Journal of the Royal Society Interface*, 2(2):39–45, 2005.

[110] Aseefhali Bankapur, Elsa Zachariah, Santhosh Chidangil, Manna Valiathan, and Deepak Mathur. Raman tweezers spectroscopy of live, single red and white blood cells. *PLoS one*, 5(4):e10427, 2010.

[111] Simon Lefrancois, Dan Fu, Gary R. Holtom, Lingjie Kong, William J. Wadsworth, Patrick Schneider, Robert Herda, Armin Zach, X. Sunney Xie,

and Frank W. Wise. Fiber four-wave mixing source for coherent anti stokes raman scattering microscopy. *Optics Letters*, 37(10):1652–1654, 2012.

[112] Rezki Becheker, Mohamed Touil, Saïd Idlahcen, Mincheng Tang, Adil Haboucha, Benoit Barviau, Frédéric Grisch, Patrice Camy, Thomas Godin, and Ammar Hideur. High-energy normal-dispersion fiber optical parametric chirped-pulse oscillator. *Optics Letters*, 45(23):6398–6401, 2020.

[113] Yasuyuki Ozeki, Takuya Asai, Jingwen Shou, and Hironobu Yoshimi. Multicolor stimulated raman scattering microscopy with fast wavelength-tunable yb fiber laser. *IEEE Journal of selected topics in quantum electronics*, 25(1):1–11, 2018.

[114] Shun Takahashi, Jingwen Shou, Gaoyu Dai, and Yasuyuki Ozeki. Widely tunable and repetition-rate-fixed fiber optical parametric oscillator. In *2023 Conference on Lasers and Electro-Optics (CLEO)*, pages 1–2. IEEE, 2023.

[115] Shun Takahashi, Kenichi Oguchi, Kento Kamei, Takaha Mizuguchi, Spencer J Spratt, and Yasuyuki Ozeki. Widely tunable fiber optical parametric oscillator synchronized with a ti: sapphire laser for stimulated raman scattering microscopy. *Biomedical Optics Express*, 15(5):3191–3199, 2024.

[116] Agnieszka Jamrozik, Mateusz Pielach, Bartosz Fabjanowicz, Katarzyna Krupa, and Yuriy Stepanenko. Quick fabrication method of a thermally expanded core in polarization-maintaining fibers using co_2 laser and fiber rotation. *Optical Fiber Technology*, 89:104055, 2025.

Appendix A

Overlapping the beams

After developing the two tunable arms (pump and Stokes), which provides a Raman shift from 900 cm^{-1} to 1300 cm^{-1}. The next step is to achieve spatial and temporal overlap of the beams. For spatial overlap, a dichroic mirror (DM, Thorlabs, DMLP1000) was used, which reflects the wavelengths from the pump arm and transmits those from the Stokes arm when is placed at 45°.

For temporal overlap, a free space delay line (DL) stage, that consisting of two mirrors was implemented, providing a range of 10 cm (corresponding to 667 ps). The beams were spatially overlapped so that the pulses were simultaneously measured by the ultra-fast photodetector (Alphalas, InGaAs). Then, an oscilloscope (WavePro 760Zi-A, Teledyne Lecroy) was used to observe the pulse train, illustrated in Figure A.1a. The peaks with higher amplitude present the pulses modulated at 1 MHz, while in the background correspond to the peaks at 17.18 MHz. Figure A.1b is a zoom version of the aforementioned pulse train. The plot illustrates the pulse at the central wavelength of 1030 nm in red, the pulse at 920 nm in black, and the highest peak in blue, which indicates the overlap of both beams achieved by adjusting the DL stage.

To verify the overlap precisely, it was taken advantage of the nonlinear effect of Second Harmonic Generation (SHG), by employing a Beta Barium Borate (BBO, Ekasma) nonlinear crystal in the system. By focusing the pump and Stokes beams into the BBO crystal, the interaction of these beams at different frequencies in the crystal produces a single Sum Frequency Generation (SFG). Next, for better visualization, a diffraction grating was used to separate the wavelengths and observe the overlap by adjusting the DL stage. Figure A.2a illustrates the schematic of the experimental setup.

Figure A.2b, the green color on the left of the screen represents the SHG of the pump beam at 515 nm, and the dark blue on the right represents the SHG of the Stokes beam at 460 nm. The overlap is confirmed by varying the DL stage and observing the distinct turquoise color at the center of the screen, generated by

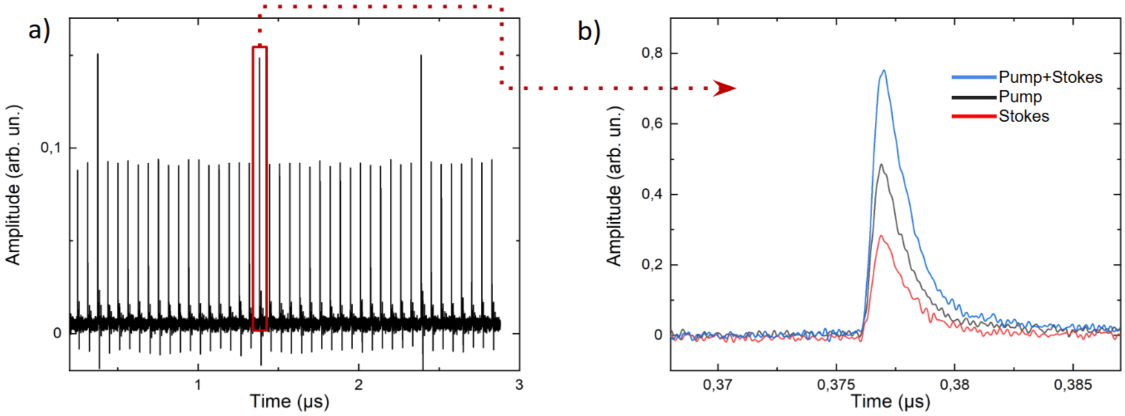

Figure A.1: Overlap in time using an oscilloscope. a) Train pulse with the highest peak at 1 MHz and the background at 17.18 MHz. b) Zoom of the overlap.

the SHG of the pump and Stokes beams at 488 nm, indicating temporal alignment. Once the central wavelength is changed, adjustment of the DL is necessary due to the different group velocity dispersion values of each wavelength. The system was calibrated by verifying the overlap with the BBO crystal for all the pump and Stokes wavelengths. This allowed for the exact position of the DL stage for perfect temporal overlap.

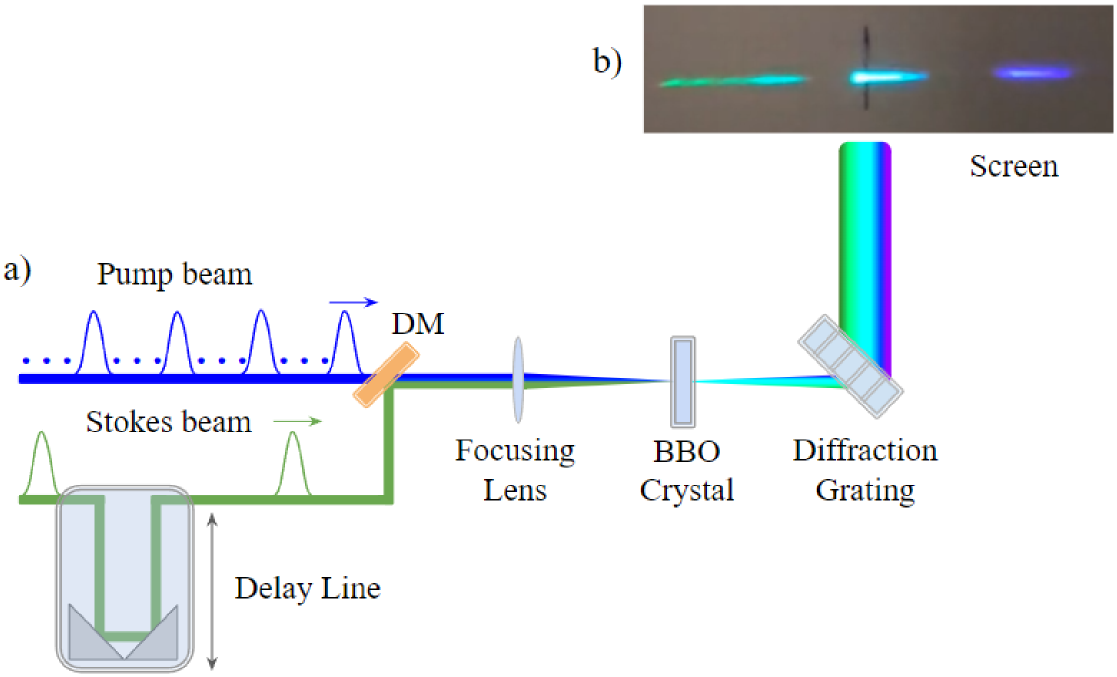

Figure A.2: a) Scheme for precise temporal overlapping using the BBO crystal. b) SHG and SFG visible on the screen by adjusting the DL stage.

Appendix B

Synchronization between the Yb-doped fiber oscillator and FOPO cavities

For the synchronization between the Yb-doped fiber oscillator (pump) and FWM FOPO cavity, the following steps were applied:

1. Both WDMs and the PCF were replaced by PM780 fiber and spliced between the OC 10/90 and the 170 m of PM780;

2. The output of the YDF pre-amplifier was connected to the output coupler (OC 10/90, DK Photonics), allowing the pulses at 1030 nm circulate in the cavity;

3. Next, both pulses were measured through a highly sensitive photodiode connected to the oscilloscope (WavePro 760Zi-A, Teledyne Lecroy), differentiating the cavity pulses by adjusting the fiber delay line. Figure B.1 illustrates the two pump pulses, with the highest one from the Yb-doped fiber oscillator and the lowest one originating from the cavity;

4. To synchronize the two pulses, I calculated the distance between them by the given equation:

   $$l = \frac{c}{n}\Delta t, \tag{B.1}$$

   where c is the velocity of light, n is the refractive index of the optical fiber, and l is the fiber length to be added or removed for synchronization.

5. The next step includes observing the lowest peak in the oscilloscope by adjusting the fiber delay line. If decreasing the delay line the lowest peaks moves the right way, requires to remove fiber, and opposite requires adding fiber;

6. Finally, the system is spliced into the WDMs and the PCF. Fine-adjustments include to verify the D-FWM signals by adjusting the fiber delay line.

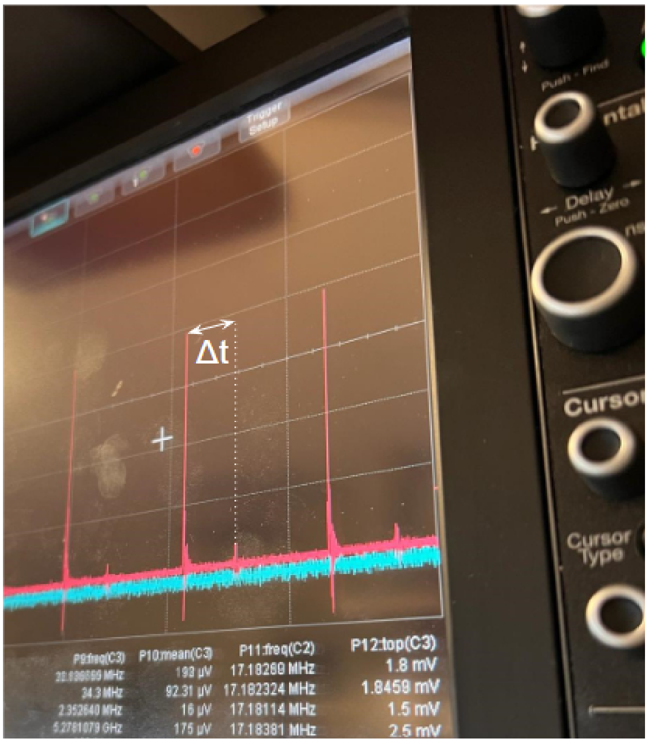

P9:freq(C3)	P10:mean(C3)	P11:freq(C2)	P12:top(C3)
[illegible] MHz	193 µV	17.18269 MHz	1.8 mV
34.3 MHz	92.31 µV	17.182324 MHz	1.8459 mV
2.352640 MHz	16 µV	17.18114 MHz	1.5 mV
5.2781079 GHz	175 µV	17.18381 MHz	2.5 mV

Figure B.1: Synchronization between the cavities using the oscilloscope.

The described synchronization operates at a ratio of around 1:17, which means that 17 pulses resonate simultaneously within the cavity. To achieve parametric gain, the length of the FOPO must be an integer of the oscillator. Various resonant pulse configurations exist for FOPO, such as 1:1, 1:2, 1:100, etc. However, increasing the FOPO cavity length might change the cavity dispersion. The dispersion influences the pulse chirp as it propagates through the cavity, which impacts the generated spectrum and FWM efficiency.